

JGR Planets

RESEARCH ARTICLE

10.1029/2020JE006536

Key Points:

- Results and stratigraphic context for APXS targets from the first 2,301 sols of the *Curiosity* Mars rover mission are presented
- Gale crater sediment has a diverse provenance that is primarily basaltic
- Alteration and diagenetic features demonstrate widespread aqueous activity

Supporting Information:

- Supporting Information S1
- Supporting Information S2
- Supporting Information S3

Correspondence to:





J. A. Berger,
jeffrey.a.berger@nasa.gov

Citation:

Berger, J. A., Gellert, R., Boyd, N. I., King, P. L., McCraig, M. A., O'Connell-Cooper, C. D., et al. (2020). Elemental composition and chemical evolution of geologic materials in Gale crater, Mars: APXS results from Bradbury Landing to the Vera Rubin ridge. *Journal of Geophysical Research: Planets*, 125, e2020JE006536. <https://doi.org/10.1029/2020JE006536>

Received 26 MAY 2020
 Accepted 13 OCT 2020

Elemental Composition and Chemical Evolution of Geologic Materials in Gale Crater, Mars: APXS Results From Bradbury Landing to the Vera Rubin Ridge

Jeff A. Berger^{1,2} , Ralf Gellert¹ , Nicholas I. Boyd¹, Penelope L. King³ , Michael A. McCraig¹, Catherine D. O'Connell-Cooper⁴ , Mariek E. Schmidt⁵ , John G. Spray⁴ , Lucy M. Thompson⁴ , Scott J. V. VanBommel⁶ , and Albert S. Yen⁷ 

¹University of Guelph, Guelph, ON, Canada, ²Now at NASA Johnson Space Center, Houston, TX, USA, ³The Australian National University, Canberra, ACT, Australia, ⁴University of New Brunswick, Fredericton, NB, Canada, ⁵Brock University, St. Catharines, ON, Canada, ⁶Washington University in St. Louis, St. Louis, MO, USA, ⁷JPL-Caltech, Pasadena, CA, USA

Abstract The Alpha Particle X-ray Spectrometer (APXS) on the rover *Curiosity* has analyzed the composition of geologic materials along a >20-km traverse in Gale crater on Mars. The APXS dataset after 6.5 Earth years (2,301 sols) includes 712 analyses of soil, sand, float, bedrock, and drilled/scooped fines. We present the APXS results over this duration and provide stratigraphic context for each target. We identify the best APXS measurement of each of the 22 drilled and scooped samples that were delivered to the instruments Chemistry and Mineralogy (CheMin; X-ray diffractometer) and Sample Analysis at Mars (SAM; mass spectrometer and gas chromatograph) during this period. The APXS results demonstrate that the basaltic and alkali-rich units in the Bradbury group (sols 0–750) show minimal alteration indicating an arid climate. In contrast, the Murray formation of the Mount Sharp group (sols ~750–2,301) has compositions indicating pervasive alteration. Diagenetic features are common and show fluid interaction with the sediment after (and possibly during) lithification. A sandstone unit, the Stimson formation, overlies part of the Murray formation. This has a composition similar to the basaltic sand and soil, suggesting a shared source. Cross-cutting, fracture-associated haloes are evidence of late-stage fluid alteration after lithification of the sediment. The APXS dataset, evaluated in concert with the full science payload of *Curiosity*, indicates that Gale crater was habitable, and that liquid water was stable for extended periods.

Plain Language Summary The Mars rover *Curiosity* uses the Alpha Particle X-ray Spectrometer (APXS) located on *Curiosity's* robotic arm to determine the composition of surface materials at the Mars Science Laboratory landing site in Gale crater. The APXS has measured more than 700 2-cm-wide spots over a >20 km traverse during 2,301 martian days, or 6.5 Earth years. This study presents those data acquired to date, and an overview of the results from this period of *Curiosity's* mission. The APXS results demonstrate that the geologic materials in Gale crater have diverse elemental compositions and include several broad groups. Most of the bedrock is made of small grains of rock transported by surface processes that may include fluvial, aeolian, impact, volcanic, and mass wasting into a lake system where they were deposited and cemented. Many of the bedrock layers show evidence for aqueous processes that can be traced using soluble elements in the rocks, veins, and concretions. We show that the elemental characteristics are consistent with bedrock alteration by acidic as well as neutral and/or alkaline waters. These results are key to the goal of *Curiosity's* mission to determine if Gale crater had an environment where microbial life could have emerged.

1. Introduction

The Alpha Particle X-ray Spectrometer (APXS) on the Mars rover *Curiosity* analyzed more than 700 targets during its first 2,301 martian solar days after landing (sols; 1 sol = 24.7 h). The primary objectives of APXS investigations are to determine the elemental composition of geologic materials in Gale crater to infer the geologic and climate history, establish whether or not liquid water was stable for extended periods, constrain the geochemical conditions of ancient liquids, and deduce the provenance of sedimentary materials

in the crater. APXS data are also key to interpreting results from the drilled and scooped samples that have been delivered to the Chemistry and Mineralogy (CheMin) X-ray diffractometer (Blake et al., 2012) and the Sample Analysis at Mars (SAM) mass spectrometer and gas chromatograph (Mahaffy et al., 2012).

In this study, we present an overview of APXS results from landing (sol 0; 6 August 2012) to the end of the Vera Rubin ridge (VRR) campaign on sol 2,301 (25 January 2019). These results encompass all APXS measurements acquired before *Curiosity* traversed into the region named Glen Torridon (e.g., Fox et al., 2019). The results demonstrate that elemental trends in Gale crater record evidence of a changing climate, widespread interaction of liquid water with the rocks, and a basaltic and alkali-rich provenance. Here, we outline the broad compositional groups and common chemical features that have emerged. The purpose of this study is to provide a context for more focused investigations so they can be better integrated for a deeper understanding of the geochemical history of Gale crater.

2. Geological Setting

Gale crater is an ~150 km wide complex impact crater with a central mound centered near the dichotomy boundary of the northern lowlands and southern highlands of Mars (5.4°S, 137.8°E). The Gale crater-forming impact occurred ~3.8–3.6 billion years ago (Ga; Le Deit et al., 2013; Thomson et al., 2011), and the crater floor was subsequently infilled with sediment likely derived from mass wasting and fluvial erosion of the crater rim and central mound before 3.3–3.1 Ga (Grant et al., 2014; Grotzinger et al., 2015). The distal end of fan deposits sourced from the crater rim and nearby upland plains via Peace Vallis reaches *Curiosity's* traverse near Bradbury Landing (Palucis et al., 2014). Exhumation of the crater floor deposits has exposed lithified sedimentary strata that were likely deposited in a fluvial and lacustrine system (Grotzinger et al., 2014, 2015). Sandstone strata consistent with a dry aeolian system unconformably overlie the fluvio-lacustrine units (Banham et al., 2018). Surface exposure age dating indicates that one unit, the Sheepbed mudstone, has been at the surface for 78 ± 30 Ma (Farley et al., 2014). Localized alluvial deposits indicate aqueous activity on Aeolis Palus <2 Ga ago (Grant & Wilson, 2019).

Curiosity's traverse is effectively a cross-section of the layered sedimentary strata in Gale crater (Figure 1). The traverse began at Bradbury Landing, and the first detailed investigation was of outcropping sedimentary strata at Yellowknife Bay (YKB). From there, *Curiosity* traversed southwest across Aeolis Palus to an entry point onto lower Aeolis Mons (informally named Mt. Sharp), where the rover heading was changed on sol ~750 to drive south-southeast toward the central mound of Mt. Sharp. The rover has been ascending a succession of horizontal to sub-horizontal sedimentary units. The mean dip is roughly horizontal, thus elevation is an acceptable proxy for stratigraphic position (Grotzinger et al., 2015). Using elevation as a proxy, a composite stratigraphic column was assembled by from Bradbury Landing to the VRR (Figure 1; Edgar et al., 2020; Fedo et al., 2018; Grotzinger et al., 2015; Stack et al., 2019; the Mars Science Laboratory [MSL] Science Team).

3. Methods

3.1. APXS Method and Geochemical Dataset

The APXS method combines particle-induced X-ray emission (PIXE) and X-ray fluorescence (XRF) techniques (Campbell et al., 2012; Gellert et al., 2006, 2009) to determine elemental concentrations in geologic samples. Curium-244 radioisotope sources emit radiation that induces characteristic X-rays from a specimen, a subset of which are in turn counted with a detector and converted into an energy dispersive spectrum. The relative areas of characteristic X-ray peaks correlate with the relative abundance of elements in the specimen, enabling the calculation of major, minor, and selected trace element concentrations for atomic number $Z \geq 11$ (Figure 2).

APXS data were reduced using a peak fitting routine with empirical concentration calculations derived from a laboratory calibration dataset, largely based on the one originally developed during the Mars Exploration Rover (MER) APXS calibration (Gellert et al., 2006), with adjustments specific to the MSL variant. The statistical peak area uncertainty (2σ) reported by the fit routine for each element represents precision and decreases with improved counting statistics and resolution (VanBommel et al., 2019a, 2019b). The 2σ

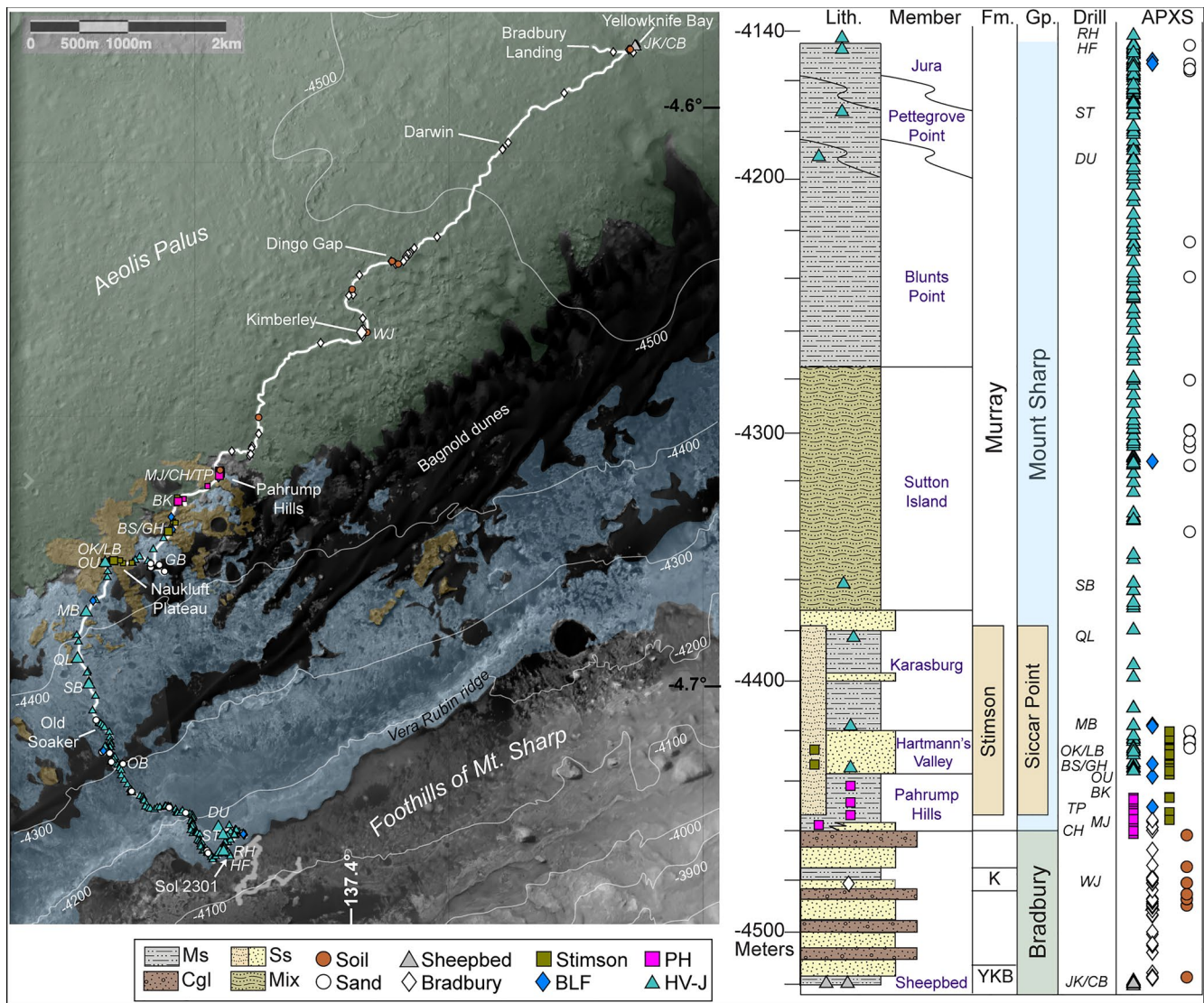


Figure 1. Map of *Curiosity*'s traverse in Gale crater and distribution of APXS targets in the Gale crater stratigraphy adapted from Grotzinger et al. (2015), Fedo et al. (2018), Stack et al. (2019), Edgar et al. (2020), and the Mars Science Laboratory Science Team Sed/Strat working group. The geologic map shows the Bradbury (green), Mt. Sharp (blue), and Siccar Point (tan) groups. Elevation is shown as contour lines on the map and the y-axis of the column. The Kimberley and Yellowknife Bay formations are indicated with K and YKB, respectively. Drill locations are shown as larger symbols on the traverse and with symbols on the unit lithology (lith.) using abbreviations shown under the 'drill' column (see Tables 3 and 4). The key indicates mudstone (Ms), mixed mudstone, siltstone, and sandstone (Mix), sandstone (Ss), and conglomerate (Cgl). APXS targets are grouped primarily by stratigraphic unit, and secondarily by composition (see text). Murray formation targets are divided into the Pahrump Hills member (PH) and the Hartmann's Valley to Jura members (HV-J). Bradbury-like float on top of Murray units is grouped separately (Bradbury-like float; BLF). The APXS symbology is consistent with all figures herein, and all omissions in the following plots are noted in the figure captions (e.g., measurements with Ca-sulfate veins).

statistical error is reported for each measurement in Data Set S1. Errors reported here have supplemental corrections applied based on a set of rules derived empirically with the testbed APXS for each element to account for physical effects that can compound to degrade precision for certain elements more than others such as poor resolution or high standoff (Gellert et al., 2006). Major, minor, and trace elements are reported in the form of 16 oxides and elements normalized to 100 weight percent (wt%). Sulfur, chlorine, and iron are reported in wt% as SO₃, Cl, and FeO, noting that oxidation state is not measured by the APXS. Instrument accuracy and typical precision error are shown in Table 1 (Gellert & Clark, 2015). The APXS accuracy, which was estimated with testbed APXS measurements of the ~100 powdered geological reference materials (GRMs) used for the APXS calibration, reflects heterogeneous matrix effects (Gellert et al., 2006). That is,

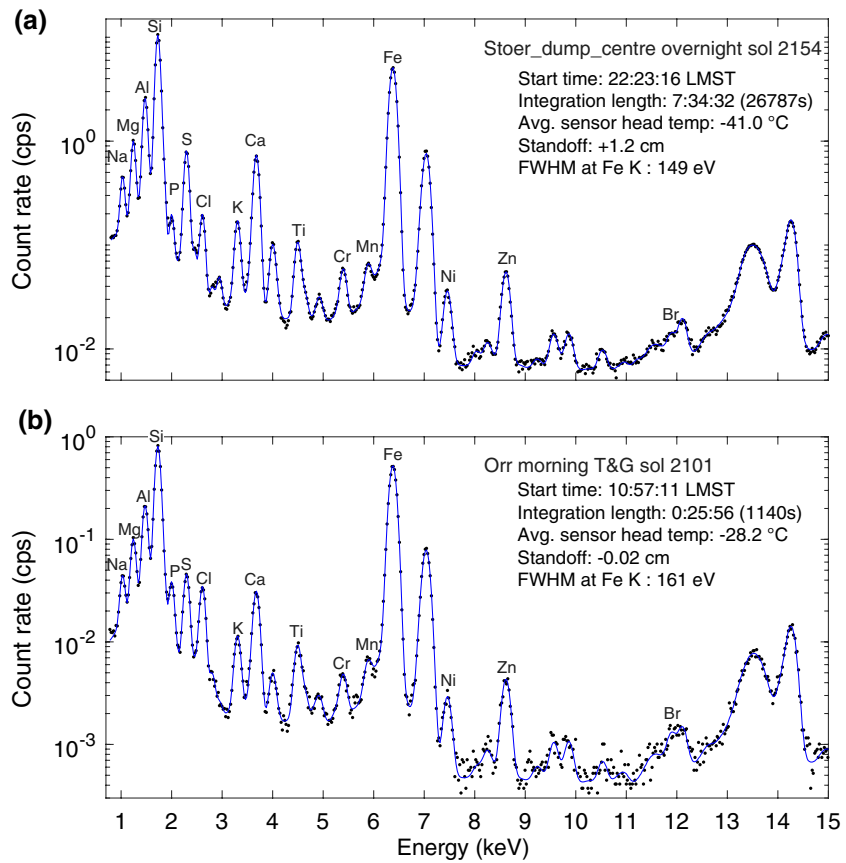


Figure 2. Typical APXS spectra showing the data (dots) and fit (line). (a) This spectrum was acquired on sol 2,154 on the dumped DBA fines of the drill target Stoer and is representative of a high-quality overnight (8 h) measurement. (b) This touch-and-go (T&G) spectrum was acquired on sol 2,101 on the target Orr and demonstrates that high-quality spectra are possible with short integrations (25 m) in mornings before the temperature is too high. For comparison, one of the ~9 low-quality spectra is shown in Figure S1. $K\alpha$ peaks of the 16 elements reported in Data Set S1 are indicated. The full APXS spectrum is not shown (15–25 keV is omitted).

the GRMs were not infinitely fine powders with respect to the APXS sampling depth, thus the assumption of sample homogeneity necessary for calculation of X-ray attenuation in the sample matrix leads to lower accuracy, which is captured in Table 1. Conditions may arise with martian targets where heterogeneous matrix effects may cause systematic offset of some elements (e.g., Mg and Al in olivine-phyric samples; Berger et al., 2020); however, evaluation of this effect should be done on a case-by-case basis rather than application of blanket corrections (Gellert et al., 2006).

The quality of APXS data is impacted by several factors that are constrained by rover operations: (1) the temperature of the APXS sensor head, (2) the length of the integration, and (3) the standoff distance from the target. Higher temperatures ($> -20^\circ\text{C}$) result in lower spectral resolution, so the rover operations team plans APXS measurements when the ambient temperatures are low enough for good data quality. For this reason, integrations are commanded during the morning (~09:00–12:00) or evenings and overnight (~17:00–06:00). The spectral quality is approximated by the full-width-at-half-maximum (FWHM) of the Fe $K\alpha$ peak (Data Set S1). The signal/noise ratio increases with longer integration times, which are given in Data Set S1 as the “lifetime” of the measurement. The signal/noise ratio decreases with larger instrument standoff distance, and so the APXS is deployed to within < 2 cm of the target, if possible, although topography of the target surface may vary. The standoff distance, estimated from the APXS signal using the method of Gellert et al. (2006), is given in Data Set S1. A detailed discussion of the effects of temperature, integration time, and standoff distance on APXS data quality is presented by VanBommel et al. (2019b). Of 712 measurements, 9 have very low-quality spectra (FWHM at Fe $K\alpha$ peak > 250 eV) and we recommend conservative interpretation of those results (e.g., Figure S1).

Table 1
APXS Precision Error and Accuracy

| | Concentration: Stoer ^a drill fines (wt%) | Statistical fitting error (wt%) | Relative accuracy ^b (%) | Limit of detection ^b (wt%) |
|--------------------------------|---|---------------------------------------|--|---|
| SiO ₂ | 44.1 | 0.54 | 3 | 1 |
| TiO ₂ | 1.03 | 0.03 | 20 | 0.2 |
| Al ₂ O ₃ | 8.75 | 0.19 | 7 | 1 |
| FeO | 21.5 | 0.26 | 7 | 0.03 |
| MnO | 0.17 | 0.01 | 8 | 0.05 |
| MgO | 4.72 | 0.17 | 14 | 1 |
| CaO | 6.44 | 0.07 | 7 | 0.2 |
| Na ₂ O | 2.45 | 0.14 | 11 | 1 |
| K ₂ O | 0.91 | 0.04 | 15 | 0.2 |
| P ₂ O ₅ | 0.84 | 0.05 | 15 | 0.3 |
| Cr ₂ O ₃ | 0.34 | 0.01 | 19 | 0.05 |
| Ni (ppm) | 915 | 50 | 16 | 50 |
| Zn (ppm) | 850 | 30 | 16 | 30 |
| SO ₃ | 7.59 | 0.10 | 15 | 0.2 |
| Cl | 0.89 | 0.02 | 30 | 0.2 |
| Br (ppm) | 45 | 5 | 20 | 20 |

^aRepresentative error for an overnight measurement is taken from the sol 2,154 analysis of Stoer_dump_centre (spectrum shown in Figure 2a).
^bAccuracy and limit of detection determined by APXS calibration (Gellert & Clark, 2015).

Curiosity's APXS instrument acquired 712 measurements on geologic materials along the rover's traverse up to sol 2,301, and the results are presented in Data Set S1. Statistical summaries of selected groups discussed herein are presented in Data Set S2. Explanations for the columns in Data Sets S1 and S2 are given in the Supporting Information document. The measured ~2-cm-wide spots were given names taken from terrestrial geographic regions (e.g., Namibia, Africa). The named spots are referred to as "targets," and they represent that specific location in Gale crater with the coordinates given in Data Set S1. A single target may have multiple measurements, as indicated by appended names (e.g., Highfield_DRT, Highfield_offset, Highfield_dump_offset; see Sections 3.2 and 4.1 for more details). Drilled and scooped materials also have target names, and that material is referred to here as "sample" because it was processed by the sampling system and, in some cases, it was dumped on the ground and measured at a different site along the traverse. Oxide and trace element concentrations for APXS measurements are presented in Data Set S1. Each target is part of a stratigraphic unit as defined by the MSL Science Team Sedimentology and Stratigraphy working group (Figure 1; e.g., Edgar et al., 2020; Grotzinger et al., 2015). The stratigraphic unit names are convenient for grouping APXS targets by location along the traverse as well as in the composite stratigraphic column; however, the units are defined primarily by sedimentological and stratigraphic observations rather than chemical or mineralogical composition. Thus, some units contain more than one compositionally distinct rock type, and groups of different units have similar compositions. Soil and sand are classified as separate units and disconnected from the stratigraphic column.

Curiosity's payload also contains a laser induced breakdown spectrometer (LIBS) on the rover's mast that quantifies most major elements and some minor and trace elements (ChemCam; Wiens et al., 2012, 2013).

ChemCam targets typically consist of 3–5 LIBS spots in a line spaced ~1–10 mm apart (e.g., Lasue et al., 2016; Mangold et al., 2015; Nachon et al., 2017). The spot size of the LIBS shots increases from ~350 to ~550 μm in diameter with increasing distance of the instrument to the target (~1.6–7 m; Wiens et al., 2012). When ChemCam analyzes a target, it progressively ablates material with LIBS shots, and each spot typically has 30 shots. The depth is usually ~90 μm but can reach up to 1 mm in a consolidated rock target (Wiens et al., 2012). A spectrum (240–905 nm) of the plasma generated by the laser is acquired for each shot, enabling measurements of surface dust (Lasue et al., 2018) as well as depth profiling (Lanza et al., 2016). In comparison, the APXS FOV is ~15–20 mm in diameter and the sampling depth varies as a function of the atomic number of the element being analyzed and the matrix composition. In a basalt matrix, for example, the sampling depth ranges from ~3 μm for Na to ~90 μm for Fe (Brückner et al., 2008; Rieder et al., 2003; Schmidt et al., 2018). The sample volume of the APXS is thus much larger than that of ChemCam. A consequence of this is that an APXS analysis of a fine-grained basalt, such as the APXS calibration target, approximates a bulk measurement (Campbell et al., 2014). In contrast, due to the smaller spot size, ChemCam requires 5–15 spots to converge on a bulk composition for a fine-grained rock (R. B. Anderson et al., 2011). The sampling differences between APXS and ChemCam lead to complexities in comparing the two datasets, and although valuable information can be derived by comparison, we do not do so herein.

3.2. Field Methods

Curiosity's APXS is an arm-mounted, robotically deployed field instrument that can analyze a variety of geologic materials under a range of environmental conditions (Figure S2). APXS targets include outcrop, veins, concretions, and unconsolidated materials. We differentiate unconsolidated materials as float, sand, soil, and dust. Note that the definition of soil by the Soil Science Society of America includes unconsolidated materials on planetary surfaces (Van Es, 2017). Float is defined here as loose fragments of rock on the

Table 2
Description of Sample Preparation Methods

| Preparation method | Abbreviation (Data Set S1) | Description | Number of targets ^a |
|-----------------------|----------------------------|--|--------------------------------|
| Unbrushed rock | RU | As-is, unbrushed rock surface | 408 |
| Brushed rock | RB | Rock surface after brushing by Dust Removal Tool (DRT) | 167 |
| Minidrill | MD | Shallow test drill; ~2–5 mm in depth; APXS deployed over chipped/abraded rock | 12 |
| Drill tailings | DT | Drill tailings ejected from the hole without being acquired by SA/SPaH, extracted from a range of depths in the drill hole up to ~5 cm and primarily from the top 2–3 cm | 27 |
| DBA drill fines | DBA | Sample dumped from the drill bit assembly (DBA) using the feed extended drilling and feed extended sample transfer (FED/FEST) techniques (sols >1,536) | 7 |
| Sieved <150 μm | Postsieve | Sample processed by SA/SPaH, sieved to <150 μm, and dumped on the ground. The targets include “postsieve” in the name | 16 |
| Sieved >150 μm | Presieve | Sample processed by SA/SPaH that did not pass through the 150 μm sieve, and dumped on the ground. The targets include “presieve” in the name | 10 |
| Sieved 150–1,000 μm | Sieve 150 μm–1 mm | Sample processed by SA/SPaH, sieved to 150–1,000 μm, and dumped on the ground | 1 |
| Sieved >1,000 μm | Sieve 1 mm | Sample processed by SA/SPaH, sieved to >1,000 μm, and dumped on the ground | 1 |
| Undisturbed soil/sand | SU | Soil and sand as-is, untouched by the rover hardware | 33 |
| Disturbed soil/sand | SD | Soil and sand that has been disturbed by the rover’s scoop and/or wheels | 9 |
| Failed drill fines | Failed | Sample fines dumped by SA/SPaH but did not fill the APXS FOV and/or was not infinitely thick with respect to APXS sampling depth | 21 |

^aNumber of APXS targets of each preparation method as of sol 2,301.

surface that are larger than coarse pebbles (~>20 mm). Outcrop targets were typically given higher priority to systematically characterize the Gale rock units. However, float was analyzed regularly when outcrop was not reachable by the rover’s arm (i.e., outside of the rover workspace) and/or to characterize the variety of materials encountered. Veins and concretions were surveyed and the different types of features were analyzed and cataloged when possible. Veins and concretions in the APXS dataset are *not necessarily* representative of the frequency or distribution of the features over the traverse. For example, over most of the traverse, *Curiosity’s* tactical operations team attempted to exclude white veins from the APXS FOV because they were previously well-characterized as Ca-sulfate and complicate bedrock measurements of Ca and S.

Curiosity utilizes several different approaches for handling samples and placing the APXS in close (~mm to cm scale) proximity to surface samples with the rover’s arm and there are consequences for data interpretation. Targets are measured by the APXS either as-is (i.e., undisturbed by rover hardware), after the surface was brushed by the Dust Removal Tool (DRT), after the target was disturbed by the rover’s scoop and/or wheels, or as fines and fragments generated by the drill. Drill fines are measured by the APXS with multiple methods (Table 2) involving the robotic arm and the sampling subsystem (SA/SPaH; R. C. Anderson et al., 2012). We refer to the different sample handling and deployment approaches as the “preparation method,” all of which are described in Table 2 with examples illustrated in Figure 3. The preparation method for every target is given in Data Set S1.

In some cases, the APXS was moved by the arm to obtain multiple, generally overlapping, measurements over an area and these are known as “rastered targets.” Targets are rastered to investigate heterogeneity on the mm-cm scale, particularly when multiple phases are apparent. Common examples are white 5–10-mm-wide veins in bedrock and small concretions (VanBommel et al., 2016, 2017). Multiple raster points on one target have the same name appended with descriptors such as “_raster1, _raster2..._rasterN.” Targets with two laterally adjacent APXS integrations within ~2 cm or less are given the same name and appended with “_centre” and “_offset.”

Context imagery and the inferred APXS FOV are used to determine what the APXS actually measured. Under optimal conditions, the rover arm placement accuracy is ~10 mm, precision is ~5 mm, and the APXS FOV is

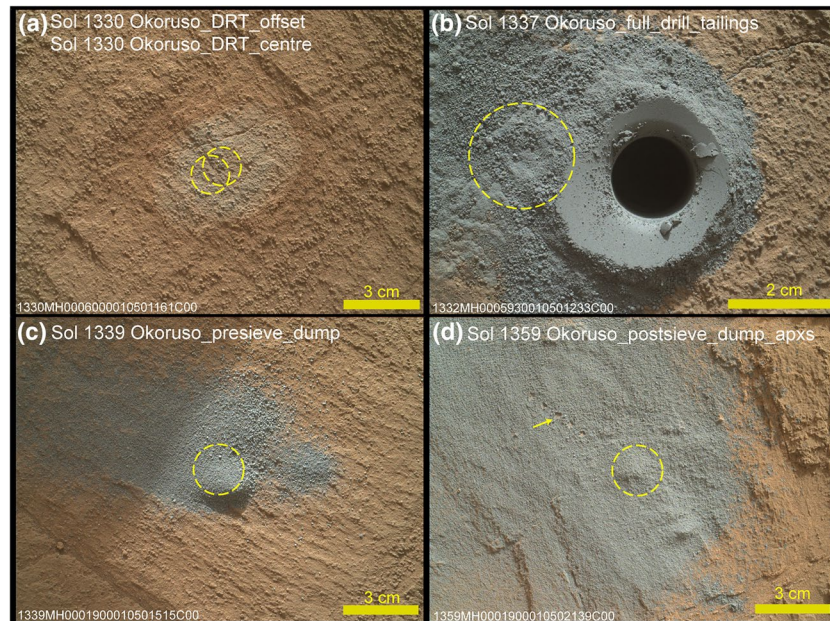


Figure 3. Mars Hand Lens Imager (MAHLI) context images of a representative APXS drill campaign (Okoruso drill site). The sol and APXS target name are shown and yellow circles denote the approximate APXS field of view (FOV). MAHLI image identification numbers are shown. (a) Before drilling, two APXS measurements were obtained after the drill site was brushed by the Dust Removal Tool (DRT): one centered in the DRT area and one offset ~ 1 cm (lower left circle) to investigate possible heterogeneity on the surface. The brushed area is the lighter-toned oval ~ 4 cm wide. (b) One APXS measurement of the drill tailings was centered on the tailings adjacent to the drill hole. (c) The pre-sieve drill fines were dumped on the ground and the APXS was placed over the thickest portion of the pile. (d) About 20 sols after driving away from the Okoruso drill site, the post-sieve drill fines were dumped on the ground for APXS analysis. This post-sieve dump pile measurement was successful because the fines fill the APXS FOV and the pile is >200 μm thick, and it is thus the best representative APXS analysis of the ChemMin sample (Tables 3 and 4). The arrow indicates one of five laser induced breakdown spectrometer pits in the fines created by ChemCam.

~ 15 – 20 mm in diameter for measurements conducted within 5 mm of the target surface. The FOV increases with larger standoff distance (VanBommel et al., 2016, 2017). We estimate the APXS FOV footprint to be circular, with a signal intensity that is higher in the center of the FOV than at the margins, with a roughly Gaussian cross-section of intensity across the diameter of the FOV. The standoff distance is estimated from the sum of all oxides (before normalization to 100 wt%), or the geometric norm, which indicates larger standoff distances when the sum is less than 100 wt% (Gellert et al., 2006), and this is converted to an average distance. To provide context imagery, APXS measurements are co-analyzed by the Mars Hand Lens Imager (MAHLI), which acquires microscopic images of the same targets (Edgett et al., 2012; Yingst et al., 2016). MAHLI images are usually acquired before the APXS deployment on the same sol. Images of fine-grained particulates (e.g., sand or drill fines) are taken after the APXS is retracted to document if/when the APXS contact plate (Figure S2) touched the particulates. MAHLI data products are the highest resolution documentation of APXS targets, and nearly all APXS deployments include at least one MAHLI image with the optical axis aligned with the center of the APXS FOV at a working distance of ~ 5 cm. In this configuration, MAHLI captures an image area of approximately 5 cm by 3 cm. Acknowledging the arm placement accuracy and precision, we typically assume that the center of the 5 cm MAHLI image is the center of the APXS FOV. This is a valid assumption, but deviations occur in co-registration of APXS and MAHLI as discussed by VanBommel et al. (2016, 2017). MAHLI data products corresponding to APXS measurements share the same base target name with APXS; MAHLI names may be appended with descriptions that do not necessarily match APXS descriptions (Edgett et al., 2015). APXS targets are also documented in images by MastCam (Bell et al., 2012), the Navigation cameras (Navcams), and the Hazard Avoidance cameras (Hazcams; Maki et al., 2012). Raw image data are available on the Planetary Data System (PDS; <https://pds-geosciences.wustl.edu/missions/msl/index.htm>; Gellert, 2012). The Analyst's Notebook for MSL is a convenient source for browsing and compiling APXS data with corresponding imagery (e.g., T. C. Stein et al., 2019; <https://an.rsl.wustl.edu/msl/mslbrowser>).

4. Results

In this section we present an overview of APXS results for the first 2,301 sols of *Curiosity's* operations in Gale crater (Data Set S1). First, we summarize the APXS results for the high value drilled and scooped samples delivered to CheMin and SAM. Second, we present results from targets that are grouped by stratigraphy: (1) soil, sand, and dust (2) Bradbury group, (3) Mt. Sharp group, and (4) Siccar Point group. Then, we present selected results indicating element mobility: fracture-associated haloes and S, Cl, Br, and P characteristics. When discussing grouped targets, we state the median oxide or element concentrations and \pm two standard deviations, as shown in Data Set S2, which presents statistical summaries of selected target groups discussed herein.

4.1. Samples Delivered to CheMin and SAM

Drilled and scooped materials are the best-characterized samples that *Curiosity* obtains because they are delivered to the CheMin and SAM instruments inside the rover chassis. Drill fines are also high-value because the drill samples a larger volume of rock more likely to represent the bulk composition, and the relatively consistent grain size reduces heterogeneity. The bulk chemical composition determined by the APXS enhances the interpretation of CheMin and SAM data. For example, APXS data can be used to determine the composition of the X-ray amorphous fraction in CheMin measurements (e.g., Morrison et al., 2018), and APXS analyses of Cl constrain the chloride/oxychlorine ratios measured by SAM (e.g., Ming et al., 2014; Sutter et al., 2018). Drill targets were strategically planned to sample bedrock formations over intervals that best characterized the sedimentary units along the traverse (e.g., Rampe et al., 2020a). The APXS was an important part of the target triage process to find the most representative sample that the rover was able to drill.

Multiple APXS analyses are acquired at drill and scoop sites, and several different sample preparation methods are employed using the rover hardware (Table 2; Figure 3). This enables an evaluation of the degree of heterogeneity inside the drill hole and any elemental enrichments at the surface (top \sim 200 μ m). Not all of the same sample preparation methods were used at every sampling site. The APXS campaigns at the 19 drill and 3 scoop sites varied depending on the science strategy and rover resources at the time of sampling. For different analyses of one site, APXS target names include the site name with appended descriptors (Data Set S1).

For every scoop and drill sampling site, we have determined which single APXS measurement is the best analogue for evaluating the sample splits ingested by CheMin and SAM (Tables 3 and 4). During a typical drill campaign, one or two analyses are conducted on the as-is and/or brushed surface, and then 2–4 analyses are obtained for the drilled fines. Fines can be sieved by SA/SPaH with 1 mm and 150 μ m grid sizes; only one sample was passed through the 1 mm and 150 μ m sieves to allow SAM to analyze a 150 μ m to 1 mm sand grain sizes (Gobabeb; Sutter et al., 2017). At most drill sites, APXS analyses of the post-sieve fines ($<$ 150 μ m grain size; abbreviated “post-sieve” in sample names) best represent the CheMin and SAM samples because the material followed the same sample collection, handling, and processing pathway as the material delivered to CheMin and SAM. However, a drill malfunction precluded the use of the sieves for samples after sol \sim 1,500, and a method was developed (feed extended drilling; FED) by which the drill fines are delivered to CheMin and SAM directly from the drill bit assembly (DBA). For these samples, APXS analyses are conducted on fines dumped onto the ground from the DBA after the samples are delivered to CheMin and SAM. Because the fines are not sieved and homogenized in the sampling subsystem, the DBA fines that the APXS analyze may not represent exactly what the onboard instruments measure; compositional heterogeneities with depth or mechanical sorting due to material properties could be preserved in the DBA.

The most effective method for analyzing samples processed by SA/SPaH with the APXS is to dump the fines on the ground and deploy the APXS over the dump pile such that the FOV is filled and the thickness is “infinite” with respect to the APXS sampling depth (\sim >200 μ m). Post-sieve and DBA fines are a portion of the same material delivered to CheMin and SAM, therefore these APXS targets are the highest priority for drill sites. However, not every APXS measurement of a dump pile was successful. In some cases, the pile was too thin and/or not centered in the APXS FOV due to movement of the sample by wind, uncertainty in the placement of the dump pile, or insufficient sample volume. Consequently, in some cases the drill tailings

Table 3
APXS Results for Drilled and Scooped Samples (Sols 0–2,301)

| Target name | Sol | Strat unit | Drill site (Abbrv.) ^a | Sample prep. ^b | Temperature ^c (C) | Standoff distance (cm) | Lifetime | FWHM Fe (eV) |
|--|-------|-------------------|----------------------------------|---------------------------|------------------------------|------------------------|----------|--------------|
| PortageRP | 89 | Soil | Rocknest (RN) | SD | −62 | 2.11 | 03:14:02 | 145 |
| APXS_Drill_Site_Raster_Integration_Site7 | 230 | Sheepbed | John Klein (JK) | Post-sieve | −43 | 1.48 | 04:02:14 | 157 |
| Cumberland_dump_pile_center | 487 | Sheepbed | Cumber-land (CB) | Post-sieve | −65 | 1.63 | 02:00:00 | 144 |
| DumpPile_Windjana | 704 | Dillinger | Windjana (WJ) | Post-sieve | −39 | 0.26 | 08:00:00 | 147 |
| Confidence_Hills_fines_post-sieve_dump | 781 | Pahrump Hills | Confidence Hills (CH) | Post-sieve | −42 | 0.41 | 04:00:00 | 145 |
| Mojave2_post-sieve_dump | 894 | Pahrump Hills | Mojave (MJ) | Post-sieve | −40 | 0.4 | 04:00:00 | 147 |
| Telegraph_Peak_post-sieve_dump | 954 | Pahrump Hills | Telegraph Peak (TP) | Post-sieve | −34 | 0.48 | 06:30:00 | 152 |
| Buckskin_post_sieve_dump_twk_corrected | 1,092 | Pahrump Hills | Buckskin (BK) | Post-sieve | −63 | 0.67 | 04:00:00 | 152 |
| Big_Sky_post-sieve_dump | 1,132 | Stimson | Big Sky (BS) | Post-sieve | −62 | 0.42 | 05:30:00 | 152 |
| Greenhorn_post-sieve_dump | 1,202 | Stimson | Greenhorn (GH) | Post-sieve | −63 | 0.46 | 07:00:00 | 153 |
| Gobabeb_DumpA_APXS | 1,226 | Bagnold Dunes | Gobabeb (GB) | Post-sieve | −65 | 0.14 | 07:30:00 | 148 |
| Lubango_presieve_apxs | 1,326 | Stimson | Lubango (LB) | Presieve | −38 | 0.5 | 04:00:00 | 146 |
| Okoruso_post-sieve_dump_apxs | 1,359 | Stimson | Okoruso (OK) | Post-sieve | −39 | 0.29 | 08:00:00 | 146 |
| Oudam_presieve_dump | 1,368 | Hartmann's Valley | Oudam (OU) | Presieve | −41 | 0.25 | 08:00:00 | 146 |
| Marimba2_full_drill_tailings | 1,426 | Karasburg | Marimba (MB) | Tailings | −43 | 0.25 | 04:22:19 | 145 |
| Quela_full_drill_tailings | 1,466 | Karasburg | Quela (QL) | Tailings | −41 | 1.48 | 05:30:00 | 145 |
| Sebina_full_drill_tailings | 1,496 | Sutton Island | Sebina (SB) | Tailings | −41 | 2.15 | 04:00:00 | 145 |
| Ogunquit_Beach_post-sieve_dump | 1,969 | Bagnold Dunes | Ogunquit Beach (OB) | Post-sieve | −41 | 0.82 | 07:00:00 | 148 |
| Duluth_DBA_dump_center | 2,080 | Blunts Point | Duluth (DU) | DBA fines | −42 | 0.67 | 08:00:00 | 147 |
| Stoer_dump_centre | 2,154 | Pettegrove Point | Stoer (ST) | DBA | −41 | 0.83 | 07:26:27 | 149 |
| Highfield_dump_centre ^d | 2,245 | Jura | Highfield (HF) | DBA | −40 | 0.87 | 01:07:02 | 148 |
| Rock_Hall_dump_corrected | 2,291 | Jura | Rock Hall (RH) | DBA | −43 | 0.68 | 07:00:00 | 149 |

| Target name | Sol | SiO ₂ | TiO ₂ | Al ₂ O ₃ | FeO | MnO | MgO | CaO | Na ₂ O | K ₂ O | P ₂ O ₅ | Cr ₂ O ₃ | Ni ppm | Zn ppm | SO ₃ | Cl | Br ppm |
|--|------|------------------|------------------|--------------------------------|------|------|------|------|-------------------|------------------|-------------------------------|--------------------------------|--------|--------|-----------------|------|--------|
| PortageRP | 89 | 43.0 | 1.19 | 9.37 | 19.2 | 0.42 | 8.69 | 7.26 | 2.70 | 0.49 | 0.95 | 0.49 | 460 | 330 | 5.47 | 0.69 | 30 |
| APXS_Drill_Site_Raster_Integration_Site7 | 230 | 41.1 | 1.05 | 8.51 | 20.7 | 0.33 | 8.97 | 7.87 | 2.93 | 0.55 | 0.92 | 0.47 | 710 | 810 | 5.91 | 0.52 | 30 |
| Cumberland_dump_pile_center | 487 | 41.1 | 0.99 | 8.63 | 22.0 | 0.29 | 9.32 | 6.66 | 3.01 | 0.62 | 0.86 | 0.46 | 930 | 920 | 4.61 | 1.19 | 70 |
| DumpPile_Windjana | 704 | 37.4 | 1.07 | 5.62 | 27.9 | 0.55 | 12.3 | 5.26 | 0.96 | 3.09 | 0.64 | 0.49 | 520 | 4780 | 3.57 | 0.57 | 120 |
| Confidence_Hills_fines_postsieve_dump | 781 | 48.1 | 1.13 | 9.73 | 19.8 | 0.37 | 5.55 | 4.58 | 2.65 | 0.98 | 1.02 | 0.39 | 930 | 2110 | 4.86 | 0.41 | 40 |
| Mojave2_postsieve_dump | 894 | 49.5 | 1.19 | 11.4 | 16.1 | 0.40 | 4.55 | 4.33 | 3.01 | 0.73 | 1.29 | 0.37 | 1030 | 2200 | 6.27 | 0.43 | 70 |
| Telegraph_Peak_postsieve_dump | 954 | 52.7 | 1.23 | 10.7 | 18.7 | 0.25 | 2.93 | 4.37 | 3.34 | 0.98 | 1.33 | 0.36 | 520 | 1230 | 2.54 | 0.30 | 40 |
| Buckskin_post_sieve_dump_twk_corrected | 1092 | 73.7 | 1.57 | 5.66 | 5.49 | 0.09 | 0.82 | 3.05 | 2.08 | 0.96 | 1.25 | 0.10 | 130 | 330 | 4.80 | 0.29 | 60 |
| Big_Sky_postsieve_dump | 1132 | 42.9 | 1.00 | 11.5 | 21.6 | 0.40 | 7.49 | 6.12 | 3.08 | 0.46 | 0.72 | 0.51 | 540 | 380 | 3.35 | 0.73 | 380 |
| Greenhorn_postsieve_dump | 1202 | 53.2 | 1.00 | 3.92 | 15.2 | 0.14 | 1.81 | 7.80 | 2.43 | 0.30 | 1.15 | 0.45 | 290 | 160 | 11.9 | 0.46 | 230 |
| Gobabeb_DumpA_APXS | 1226 | 47.9 | 0.88 | 9.78 | 17.9 | 0.37 | 7.57 | 7.30 | 2.75 | 0.49 | 0.79 | 0.39 | 440 | 200 | 3.36 | 0.50 | 20 |
| Lubango_presieve_apxs | 1326 | 59.7 | 1.11 | 3.09 | 8.22 | 0.09 | 1.55 | 8.22 | 1.92 | 0.31 | 1.33 | 0.29 | 110 | 90 | 13.7 | 0.32 | 60 |
| Okoruso_postsieve_dump_apxs | 1359 | 45.1 | 0.94 | 9.64 | 22.4 | 0.39 | 8.97 | 6.36 | 3.08 | 0.37 | 0.75 | 0.41 | 490 | 320 | 0.96 | 0.50 | 110 |
| Oudam_presieve_dump | 1368 | 51.8 | 1.05 | 9.40 | 18.7 | 0.22 | 4.90 | 4.55 | 2.59 | 0.87 | 0.52 | 0.32 | 770 | 1080 | 4.36 | 0.35 | 20 |

Table 3
Continued

| Target name | Sol | SiO ₂ | TiO ₂ | Al ₂ O ₃ | FeO | MnO | MgO | CaO | Na ₂ O | K ₂ O | P ₂ O ₅ | Cr ₂ O ₃ | Ni ppm | Zn ppm | SO ₃ | Cl | Br ppm |
|------------------------------------|------|------------------|------------------|--------------------------------|------|------|------|------|-------------------|------------------|-------------------------------|--------------------------------|-----------|-----------|-----------------|------|-----------|
| Marimba2_full_drill_tailings | 1426 | 46.0 | 1.07 | 8.49 | 22.5 | 0.09 | 4.58 | 5.27 | 2.11 | 0.83 | 1.05 | 0.33 | 1080 | 1080 | 6.78 | 0.48 | 260 |
| Quela_full_drill_tailings | 1466 | 44.8 | 1.05 | 8.48 | 18.9 | 0.22 | 4.10 | 7.48 | 2.19 | 0.77 | 1.10 | 0.29 | 1000 | 830 | 9.30 | 1.01 | 40 |
| Sebina_full_drill_tailings | 1496 | 46.2 | 1.10 | 8.68 | 18.3 | 0.16 | 4.25 | 7.13 | 2.01 | 0.83 | 0.61 | 0.30 | 1020 | 810 | 9.1 | 1.06 | 100 |
| Ogunquit_Beach_postsieve_dump | 1969 | 47.5 | 0.93 | 10.44 | 17.3 | 0.36 | 7.55 | 7.14 | 2.85 | 0.59 | 0.76 | 0.46 | 440 | 250 | 3.4 | 0.57 | 23 |
| Duluth_DBA_dump_center | 2080 | 42.9 | 1.05 | 7.81 | 22.1 | 0.21 | 2.66 | 7.52 | 2.24 | 0.94 | 1.11 | 0.32 | 920 | 1420 | 9.86 | 0.89 | 20 |
| Stoer_dump_centre | 2154 | 44.1 | 1.03 | 8.75 | 21.5 | 0.17 | 4.72 | 6.44 | 2.45 | 0.91 | 0.84 | 0.34 | 910 | 850 | 7.59 | 0.89 | 40 |
| Highfield_dump_centre ^d | 2245 | 51.6 | 0.88 | 9.64 | 17.3 | 0.15 | 4.29 | 4.84 | 2.57 | 0.89 | 0.79 | 0.28 | 930 | 660 | 5.63 | 0.92 | 60 |
| Rock_Hall_dump_corrected | 2291 | 37.4 | 1.00 | 7.33 | 20.0 | 0.08 | 3.97 | 8.64 | 2.13 | 0.62 | 0.87 | 0.31 | 1000 | 920 | 15.28 | 2.10 | 230 |

^aNote that the abbreviations listed here correspond with those discussed in presentations of results from CheMin (e.g., Bristow et al., 2018) and SAM (e.g., Sutter et al., 2018).

^bSee Table 2 for an explanation of preparation methods.

^cTemperature indicates average temperature of the APXS sensor head chassis.

^dHighfield_dump_offset on sol 2245 was of comparable quality and has small compositional differences.

or pre-sieve fines are the best sample measured by APXS for particular drill holes. Based on assessments of the centered placement of the APXS and thickness of the dump piles, we have determined the best single drill fines targets for interpreting CheMin and SAM results (Tables 3 and 4). Note that most of the post-sieve samples collected before the change to FED (after sol 2000) were dumped by SA/SPaH after being cached for a period during which the rover drove away from the sample site. The coordinates listed in Data Set S1 indicate the dump location (latitude, longitude, and elevation) as well as the sampling location (easting, northing, and elevation₂).

4.2. Soil, Sand, and Dust

Orbital, in situ, and meteoritic observations suggest that the average composition of the martian crust is basaltic (e.g., McSween et al., 2009), and this is reflected in the unconsolidated soil, sand, and dust in Gale crater. Nine soil targets and 39 sand targets were analyzed over the first 2,301 sols of *Curiosity's* traverse (Data Sets S1 and S2), and detailed results and interpretations have been presented previously (O'Connell-Cooper et al., 2017 and 2018). Airfall dust was measured on the rover's titanium observation tray on sols 177 and 571, as discussed by Berger et al. (2016). Soil is distinguished from sand primarily by two characteristics. First, soil has higher P₂O₅, SO₃, Cl, and Zn concentrations than sand. Second, aeolian processes are actively transporting the sand, whereas soil has a surface lag deposit and is more cohesive, indicating that it may be a less recently active deposit than sand, that is, soils are isolated, inactive bedforms (O'Connell-Cooper et al., 2017; Sullivan et al., 2008; Weitz et al., 2018).

The bulk chemical composition of the soil, sand, and dust is basaltic (Figure 4), with a volatile-free SiO₂ concentration of 46 ± 4 wt%, $(\text{Na}_2\text{O} + \text{K}_2\text{O}) = 3.3 \pm 1$ wt%, $\text{FeO}/\text{MnO} = 50 \pm 8$, and without systematic depletions or enrichments in other major or minor elements (Data Sets S1 and S2). The alkali content is higher than the SNC martian meteorites, (e.g., McSween et al., 2009), but approximately the same as the bulk polymict breccia martian meteorites (Agee et al., 2013). The sand targets have a wider range in major elements owing to aeolian sorting of mafic and felsic components: targets were selected intentionally to evaluate this effect (e.g., targeting ripple crests vs. troughs; O'Connell-Cooper et al., 2017 and 2018).

Soil, sand, and dust are enriched in volatile elements S, Cl, and Zn, relative to bulk silicate Mars (Figure 5). Bulk Mars is likely enriched in volatile elements relative to the Earth (e.g., Dreibus & Wanke, 1985; Lodders & Fegley, 1997). However, the basaltic, unconsolidated soil, sand, and dust (as well as the lithified basaltic Gale crater sedimentary units) are all enriched in SO₃ (1–8 wt%), Cl (0.4–2 wt%), and Zn (130–940 ppm) compared to the ranges predicted for the crust and mantle (SO₃ ~270–2,750 ppm; Cl ~25–390 ppm; Zn ~80 ppm; e.g., Filiberto et al., 2019; Lodders & Fegley, 1997; G. J. Taylor et al., 2010). Figure 5 shows

Table 4
Statistical 2σ Error^a for Analyses of Drilled and Scooped Samples (Table 3)^b

| Target name | Sol | SiO ₂ | TiO ₂ | Al ₂ O ₃ | FeO | MnO | MgO | CaO | Na ₂ O | K ₂ O | P ₂ O ₅ | Cr ₂ O ₃ | Ni ppm | Zn ppm | SO ₃ | Cl | Br ppm |
|--|-------|------------------|------------------|--------------------------------|-----|------|------|------|-------------------|------------------|-------------------------------|--------------------------------|-----------|-----------|-----------------|------|-----------|
| PortageRP | 89 | 0.5 | 0.05 | 0.19 | 0.2 | 0.02 | 0.25 | 0.08 | 0.14 | 0.02 | 0.07 | 0.03 | 30 | 20 | 0.10 | 0.03 | 10 |
| APXS_Drill_Site_Raster_ Integration_Site7 | 230 | 0.4 | 0.03 | 0.19 | 0.3 | 0.01 | 0.25 | 0.08 | 0.14 | 0.02 | 0.07 | 0.01 | 40 | 30 | 0.08 | 0.02 | 5 |
| Cumberland_dump_pile_center | 487 | 0.4 | 0.03 | 0.19 | 0.3 | 0.02 | 0.25 | 0.07 | 0.14 | 0.02 | 0.05 | 0.03 | 50 | 30 | 0.10 | 0.04 | 10 |
| DumpPile_Windjana | 704 | 0.4 | 0.03 | 0.19 | 0.3 | 0.01 | 0.25 | 0.06 | 0.07 | 0.10 | 0.05 | 0.01 | 30 | 150 | 0.05 | 0.01 | 5 |
| Confidence_Hills_fines_post- sieve_dump | 781 | 0.5 | 0.05 | 0.29 | 0.3 | 0.01 | 0.17 | 0.06 | 0.14 | 0.04 | 0.07 | 0.01 | 50 | 70 | 0.08 | 0.02 | 5 |
| Mojave2_post-sieve_dump | 894 | 0.5 | 0.05 | 0.29 | 0.2 | 0.01 | 0.17 | 0.06 | 0.14 | 0.02 | 0.07 | 0.01 | 60 | 70 | 0.08 | 0.02 | 5 |
| Telegraph_Peak_post-sieve_dump | 954 | 0.5 | 0.05 | 0.29 | 0.2 | 0.01 | 0.08 | 0.06 | 0.14 | 0.04 | 0.07 | 0.01 | 30 | 40 | 0.05 | 0.01 | 5 |
| Buckskin_post_sieve_dump_ twk_corrected | 1,092 | 0.8 | 0.05 | 0.19 | 0.1 | 0.01 | 0.83 | 0.04 | 0.07 | 0.04 | 0.07 | 0.01 | 10 | 10 | 0.08 | 0.01 | 5 |
| Big_Sky_post-sieve_dump | 1,132 | 0.5 | 0.03 | 0.29 | 0.3 | 0.01 | 0.17 | 0.07 | 0.14 | 0.02 | 0.05 | 0.01 | 30 | 20 | 0.05 | 0.02 | 15 |
| Greenhorn_post-sieve_dump | 1,202 | 0.5 | 0.03 | 0.10 | 0.2 | 0.01 | 0.08 | 0.08 | 0.14 | 0.01 | 0.07 | 0.01 | 20 | 10 | 0.13 | 0.01 | 10 |
| Gobabeb_DumpA_APXS | 1,226 | 0.5 | 0.03 | 0.29 | 0.2 | 0.01 | 0.17 | 0.08 | 0.14 | 0.02 | 0.05 | 0.01 | 20 | 10 | 0.05 | 0.01 | 5 |
| Lubango_presieve_apxs | 1,326 | 0.6 | 0.05 | 0.10 | 0.1 | 0.01 | 0.83 | 0.08 | 0.07 | 0.01 | 0.07 | 0.01 | 10 | 10 | 0.15 | 0.01 | 5 |
| Okoruso_post-sieve_dump_apxs | 1,359 | 0.5 | 0.03 | 0.29 | 0.3 | 0.01 | 0.25 | 0.07 | 0.14 | 0.01 | 0.05 | 0.01 | 20 | 10 | 0.03 | 0.01 | 5 |
| Oudam_presieve_dump | 1,368 | 0.5 | 0.03 | 0.19 | 0.2 | 0.01 | 0.17 | 0.06 | 0.14 | 0.04 | 0.05 | 0.01 | 40 | 40 | 0.05 | 0.01 | 5 |
| Marimba2_full_drill_tailings | 1,426 | 0.5 | 0.03 | 0.19 | 0.3 | 0.01 | 0.17 | 0.06 | 0.07 | 0.04 | 0.07 | 0.01 | 60 | 40 | 0.08 | 0.02 | 10 |
| Quela_full_drill_tailings | 1,466 | 0.5 | 0.03 | 0.19 | 0.2 | 0.01 | 0.08 | 0.08 | 0.14 | 0.02 | 0.07 | 0.01 | 50 | 20 | 0.13 | 0.02 | 5 |
| Sebina_full_drill_tailings | 1,496 | 0.5 | 0.03 | 0.19 | 0.2 | 0.01 | 0.17 | 0.08 | 0.14 | 0.04 | 0.05 | 0.03 | 50 | 20 | 0.15 | 0.03 | 10 |
| Ogunquit_Beach_post-sieve_ dump | 1969 | 0.5 | 0.03 | 0.29 | 0.2 | 0.01 | 0.17 | 0.08 | 0.14 | 0.02 | 0.05 | 0.01 | 25 | 10 | 0.05 | 0.02 | 5 |
| Duluth_DBA_dump_center | 2080 | 0.5 | 0.03 | 0.19 | 0.3 | 0.01 | 0.08 | 0.08 | 0.07 | 0.04 | 0.07 | 0.01 | 50 | 50 | 0.10 | 0.02 | 5 |
| Stoer_dump_centre | 2,154 | 0.5 | 0.03 | 0.19 | 0.3 | 0.01 | 0.17 | 0.07 | 0.14 | 0.04 | 0.05 | 0.01 | 50 | 30 | 0.10 | 0.02 | 5 |
| Highfield_dump_centre | 2,245 | 0.5 | 0.03 | 0.29 | 0.2 | 0.01 | 0.17 | 0.07 | 0.14 | 0.04 | 0.05 | 0.03 | 50 | 30 | 0.13 | 0.03 | 5 |
| Rock_Hall_dump_corrected | 2,291 | 0.4 | 0.03 | 0.19 | 0.3 | 0.01 | 0.08 | 0.10 | 0.07 | 0.02 | 0.05 | 0.01 | 50 | 30 | 0.17 | 0.03 | 10 |

^aPrecision; see Table 1 and Section 3.1. ^bConcentrations are in wt% unless otherwise noted.

SO₃, Cl, and Zn concentrations, as well as the consistent molar S/Cl ratio of 3.4 ± 0.2 in soils and dust. The same S/Cl ratio was found by the two MER rovers in basaltic soils (Yen et al., 2005). The molar S/Cl of sand (2.8 ± 0.2) is lower than soils and dust due to an apparent Cl enrichment and/or S depletion (O'Connell-Cooper et al., 2017). Sulfur, chlorine, and zinc are higher in soils than they are in sand (Figure 5). Sulfur and chlorine are yet higher in airfall dust than in soil and sand (Figure 5a). The MER APXS instruments found that Zn is enriched in surface dust relative to soil (Yen et al., 2005); this couldn't be confirmed with the MSL APXS because Zn was not detectable due to the thinness of the sample of airfall dust on top of the observation tray (Berger et al., 2016).

Phosphorus is positively correlated with S, Cl, and Zn in the sand and soil, but the sand has lower P₂O₅ (0.77 ± 0.09 wt%) than the soil (0.93 ± 0.05 wt%; Figure 6). The mean molar P:Cl in sand and soil is 0.75 ± 0.09 , which is inconsistent with pure chlorapatite (molar P:Cl = 2.9). Assuming the dust content is higher in the soil than in the sand, this is evidence of phosphorus enrichment in the dust. Phosphorus enrichment in airfall dust was also observed on the MER magnets (Goetz et al., 2005). The five sand outliers in Figure 6 with higher P₂O₅ (>0.90 wt%) at a given SO₃, Cl, and Zn are targets that had dust coatings on grains as well as larger average grain sizes (330–480 μm) than the sand with lower P₂O₅ (100–260 μm; Weitz et al., 2018). This is consistent with higher dust content and/or greater heterogeneity due to larger grains in the APXS FOV.

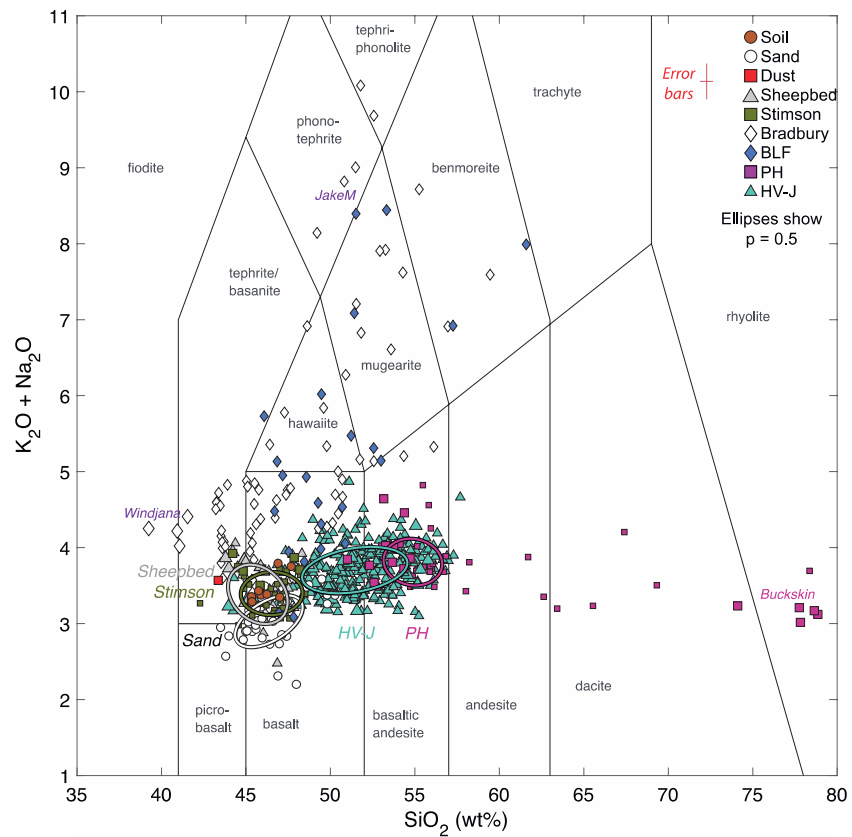


Figure 4. Volatile-free, total alkali versus silica diagram (Le Maitre et al., 2002) for Gale crater rocks, soils, sand, and dust. Veins, alteration haloes, and other diagenetic features are omitted. Concentrations are renormalized to 100 wt% without SO_3 and Cl. Drill fines are indicated by the larger symbols and Mahalanobis ellipses (probability = 0.5) are shown for sand, the Sheepbed member, and the Stimson and Murray (PH and HV-J) formations to aid interpretation of overlapping data points. The PH ellipse excludes the high SiO_2 Buckskin targets. Error bars are omitted for clarity; typical error bars are shown.

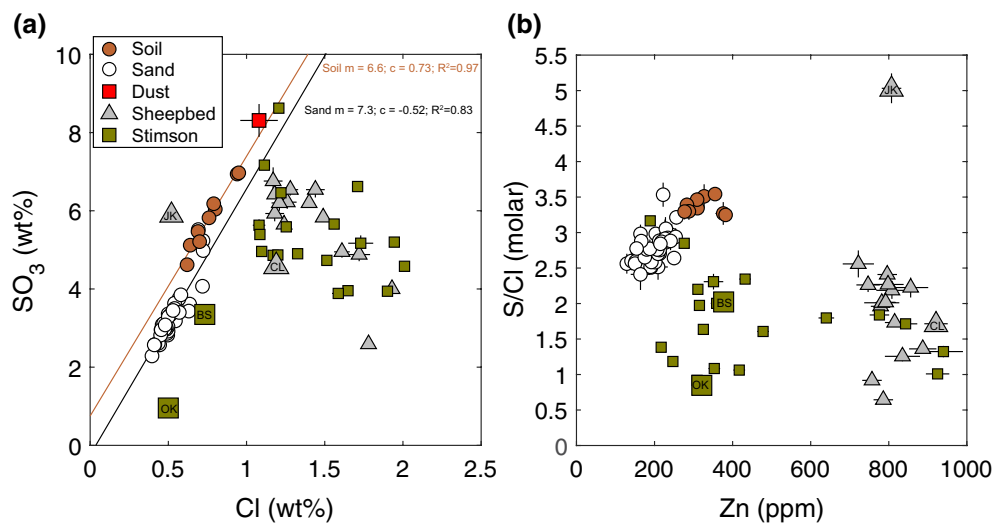


Figure 5. Volatile element concentrations in soil, sand, and dust compared to the basaltic bedrock units Sheepbed and Stimson. Regression lines for soil and sand each are shown in (a). The larger symbols denote drill fines from the four drill sites in bedrock: John Klein (JK), Cumberland (CL), Big Sky (BS), and Okoruso (OK). The dust composition is not shown in (b) because the concentration of Zn in the dust was not determined (Berger et al., 2016). Two σ error bars in this and all plots herein are shown when larger than the symbols except as noted.

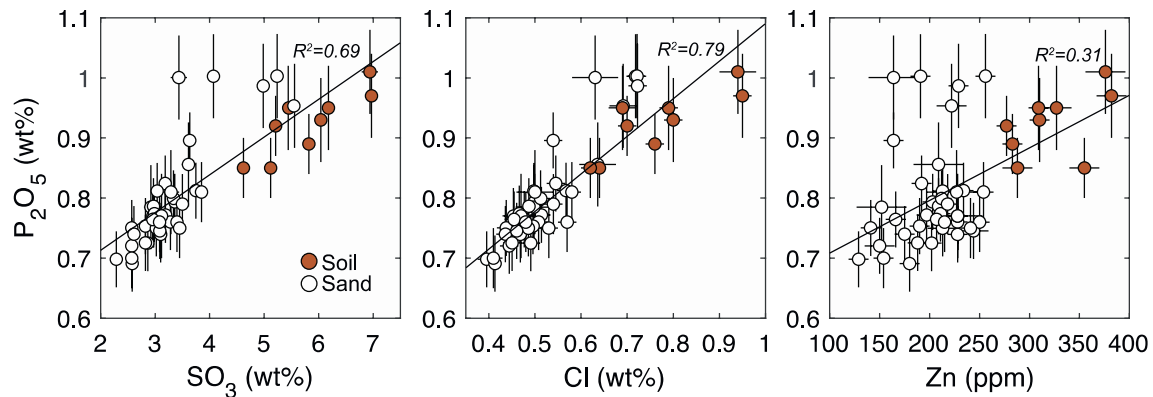


Figure 6. P_2O_5 versus SO_3 , Cl, and Zn in sand and soil. The line shows the ordinary least-squares regression and R^2 is denoted.

The MER and MSL APXS observations show that the unconsolidated fine-grained materials on Mars have varying proportions of: (1) regional sediment derived from basalt with a relatively uniform composition, (2) local materials (e.g., silica, sulfate, hematite, and potassic rock), and (3) P-, S-, Cl-, and Zn-rich global dust (Berger et al., 2016; Bishop et al., 2002; McGlynn et al., 2011; McSween & Keil, 2000; O'Connell-Cooper et al., 2017). The dust is an important component because the similarity among the three landing sites is consistent with global mixing and a uniform dust unit, likely due to the recurring (averaging 3 martian years) global dust storms (Berger et al., 2016; Yen et al., 2005).

Based on the evidence summarized above, the basaltic soil, which has minimal local contributions, has been hypothesized to represent the major and minor elemental composition of the average Mars crust by Taylor and McLennan (2010). This average crustal composition was compiled largely from MER APXS analyses of basaltic soils at Meridiani Planum and Gusev Crater renormalized after subtracting SO_3 and Cl (e.g., Gellert et al., 2006; Ming et al., 2008; Yen et al., 2005). Gale soils have a composition similar to basaltic soils analyzed by MER APXS (O'Connell-Cooper et al., 2017), as well as the airfall dust that settled on *Curiosity* (Berger et al., 2016). The overlapping basaltic soil and dust compositions and the constant S/Cl (3.7 ± 0.7) measured by APXS instruments at three rover landing sites (e.g., Franz et al., 2019; O'Connell-Cooper et al., 2017) supports this conclusion. For this reason, here we define enrichment and depletion in Gale materials relative to Gale soil, which is reasonable as a representative composition of average martian surface materials. Here, we use the Sourdough soil measurement from sol 673 to represent average soils because it was the highest quality soil measurement (i.e., smallest standoff distance for an overnight measurement of a disturbed soil).

4.3. Sedimentary Rock Units

Below we present APXS results for the sedimentary rock units in Gale crater, following the stratigraphic column starting with the lowermost units and then the subsequent overlying units (Figure 1). Subunits with distinct compositions and characteristics are discussed separately; not all subunits are discussed individually because they can be grouped generally by composition.

4.3.1. Bradbury Group

The Bradbury group contains the distinct Sheepbed member mudstone in the YKB formation. The Bradbury group from YKB to lower Mt. Sharp are grouped together and discussed separately from the Sheepbed member because they are sandstone and conglomerate units with variable compositions.

4.3.1.1. Sheepbed Member

The Sheepbed member is the stratigraphically lowermost unit investigated by *Curiosity* in the YKB formation of the Bradbury group during sols ~130–290 (Figure 1). The area explored (~800 m²) is a small fraction of the ~4 km² extent of the Sheepbed member exposed at the surface (Grotzinger et al., 2014). The very fine (<50 μm) grain size and saponitic smectite (~20%) content is consistent with a mudstone, which

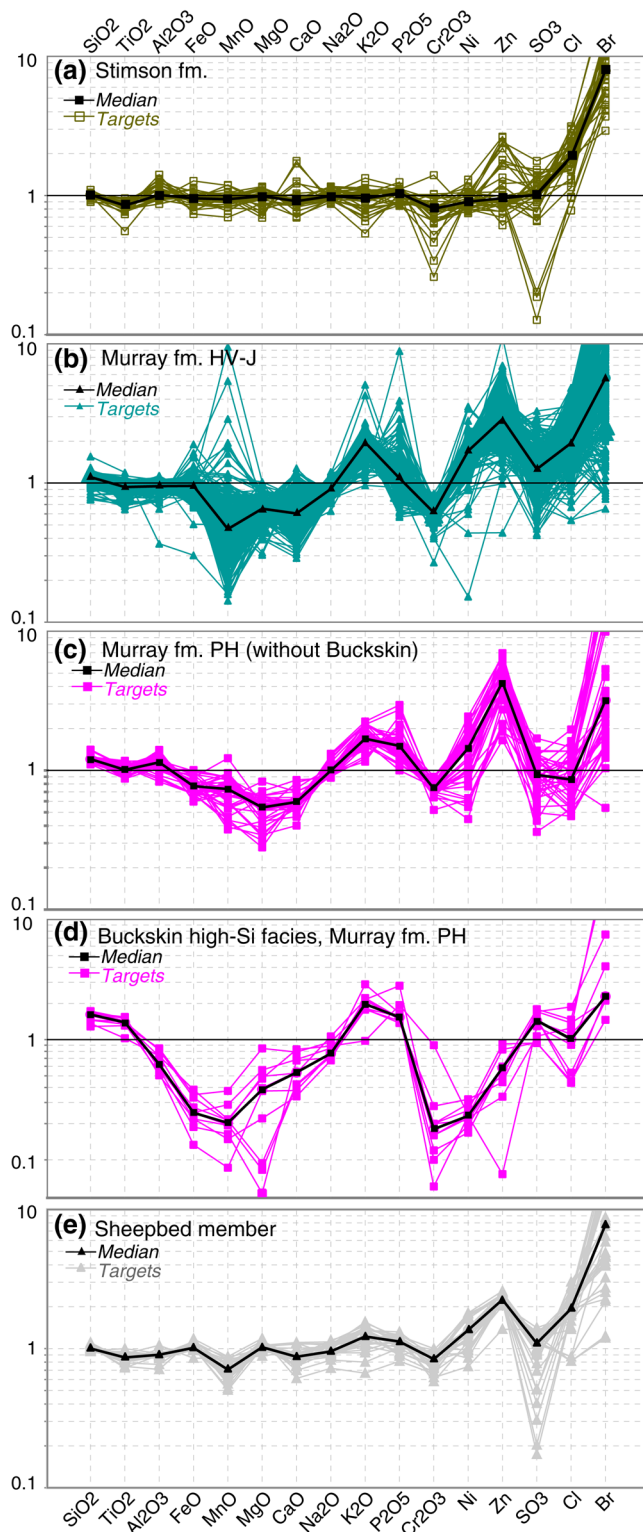


Figure 7. Element ratios in selected sedimentary units, normalized by soil (Sourdough sol 673). The units are shown in stratigraphic order (Figure 1): (a) Stimson formation, (b) Hartmann’s Valley to Jura members (HV-J), (c) Pahrump Hills member (PH) excluding the Buckskin high-Si facies, (d) the SiO₂-enriched Buckskin targets are shown separately for clarity, and (e) the Sheepbed member. Targets with prominent Ca-sulfate veins (SO₃ > 15 wt%) are omitted.

contains Ca-sulfate filled fractures and voids, raised ridges, and nodules (Grotzinger et al., 2014; Vaniman et al., 2014).

Major and minor element concentrations in the Sheepbed member (Data Sets S1 and S2) are similar to soil (Figure 7e) and consistent with a basaltic composition (Figure 4). Plots of total alkali versus silica (Figure 4) and Mg/Si versus Al/Si (Figure 8a) demonstrate the overlapping major element compositions of the Sheepbed member with those of soil, sand, and dust. Minor and trace elements differ from soil, having 40% higher Ni (700 ± 130 ppm), 160% higher Zn (800 ± 50 ppm), and 30% lower MnO (0.29 ± 0.04 wt%). The low MnO is reflected in a high FeO/MnO ratio (70 ± 10), which is distinctive from the basaltic soils analyzed by the APXS on the MER and MSL missions (~50 ± 5; O’Connell-Cooper et al., 2017). The Sheepbed member bedrock is also enriched in Ge (~85 ppm), whereas it is below the limit of detection (LOD) of ~30 ppm in the basaltic soils (Berger et al., 2017). Relative to concentrations predicted for the average basaltic crust (see Section 4.2), the Sheepbed member is enriched in volatile elements S, Cl, and Zn (Figure 5). The Sheepbed bedrock, however, does not have the same S/Cl correlation as soil owing to the wider range of Cl contents (Figure 5b; see Section 4.4.3.).

4.3.1.2. Yellowknife Bay to Lower Mt. Sharp

The Bradbury group units overlying the Sheepbed member of the YKB formation are characterized by common alkali-rich (i.e., high Na₂O and/or K₂O) sedimentary materials that are mixed with basaltic sedimentary materials. These rocks occur in a mix of sandstone and conglomerate strata and as unconsolidated regolith, or float (Figures 1 and 9; Grotzinger et al., 2014, 2015). During much of the traverse over this section of the Bradbury group, outcrop was sparse and most of the APXS targets were on float rocks. Differentiating float from outcrop was ambiguous in some cases. Here, we group float and possible float as part of the Bradbury group. The Windjana drill target (sols 612–704) in the Dillinger member of the Kimberley formation is the only drilled sample in the alkali-rich units of the Bradbury group (Treiman et al., 2016). Assessments of the distribution and APXS compositions of the alkali-rich Bradbury group targets were presented previously (Schmidt et al., 2014; Siebach et al., 2017; Thompson et al., 2016). Herein, we denote results for the Sheepbed member of the Bradbury group with different symbols (gray triangles) than the rest of the Bradbury group (white diamonds) to distinguish the finer-grained, basaltic mudstone from the coarser-grained, alkali-rich units overlying it (Figure 1).

The alkali-rich rocks display two major element trends relative to the basaltic sedimentary units (Data Set S1). One trend is toward high total alkali typified by the target JakeM (sol 46–47). The JakeM rocks have high Na₂O + K₂O (4–10 wt%; Figure 4) and Al₂O₃ (14–17 wt%) and low MgO (<5 wt%) and FeO (<13 wt%). JakeM and similar rocks were classified as mugearitic based on the bulk APXS composition (Schmidt et al., 2014; Stolper et al., 2013). Note that chemical composition alone is not conventional for classifying terrestrial igneous rocks, but the chemical consistency of JakeM with mugearites on Earth supports the use of this term to classify similar rocks on Mars (Stolper et al., 2013). Nevertheless, some of the mugearitic rocks have possible igneous characteristics: vesicles, resistance to erosion, scalloped ventifacts, and porphyritic textures (Mangold et al., 2017). The second trend is potassic and is typified by the drill

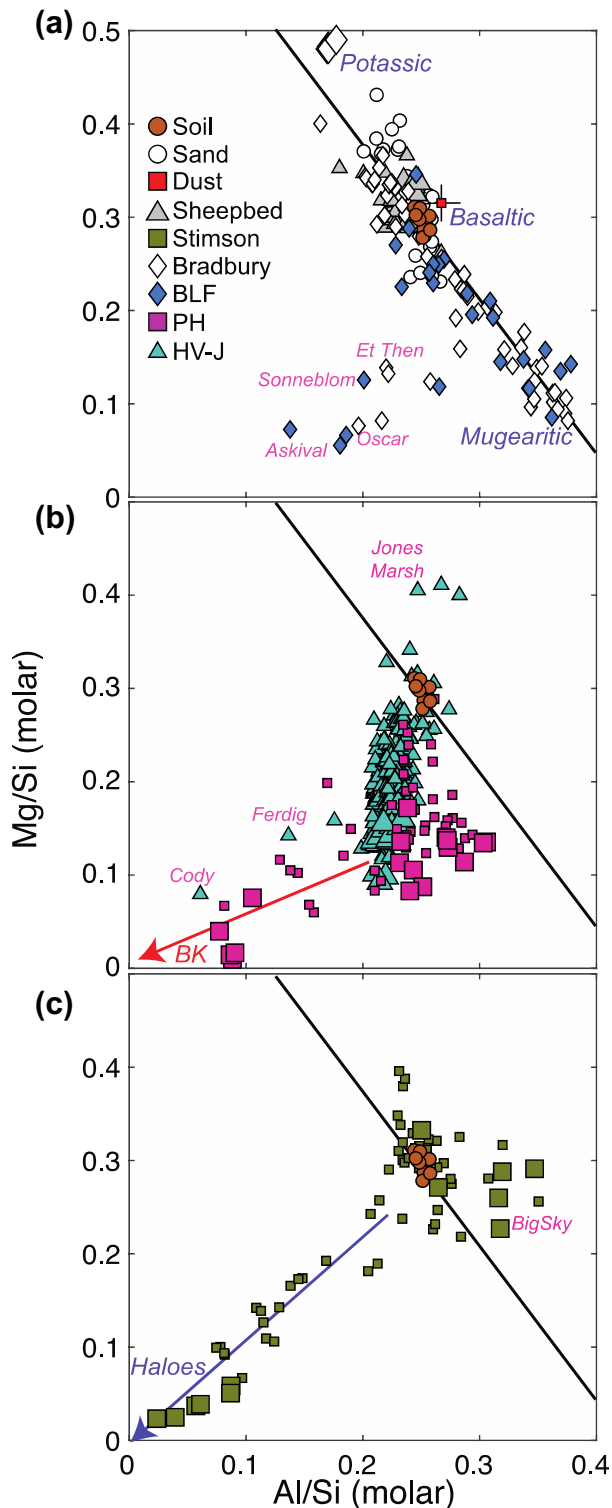


Figure 8. Major element ratios Mg/Si versus Al/Si for (a) the Bradbury group, (b) the Murray formation, and (c) the Stimson formation. The black line delineates a trend consistent with fractionation of mafic/felsic materials, and deviation from this trend indicates open-system alteration (Ming et al., 2006). Larger symbols denote drill fines. Targets discussed in the text and the high silica trends associated with Buckskin (BK; red arrow) and the Stimson fracture haloes (blue arrow) are indicated.

target Windjana in the Dillinger member of the Kimberley formation. The potassic rocks have high K_2O (1.0–3.7 wt%), FeO (20–27 wt%), and MgO (9–13 wt%), but relatively low Na_2O (<2.5 wt%). Windjana, the only alkali-rich sample drilled and analyzed with CheMin XRD, is classified as a potassic basaltic sandstone (Treiman et al., 2016). CheMin results indicate that all of the K_2O is in sanidine, which is ~20 wt% of the sample (Treiman et al., 2016). The two major element trends are apparent in a total alkali versus silica diagram (Figure 4), where the JakeM trend plots in the high-alkali basalt and alkali-rich fields with higher $Na_2O + K_2O$ and SiO_2 , and the Windjana trend has lower SiO_2 and intermediate $Na_2O + K_2O$, plotting in the alkali-basalt, tephrite/basanite, and foidite fields. The differences in Si, Al, and Mg are apparent in Figure 8a, where the mugearitic trend has lower Mg/Si and higher Al/Si. Using a classification scheme adapted from Mangold et al. (2017), we refer to the two alkali-rich chemical trends as mugearitic and potassic. For brevity, we use the term “mugearitic” to represent compositions that fall within or above the hawaiite-mugearite-benmoreite fields in the total alkali versus silica diagram (Figure 4). The mugearitic trend has higher $Na_2O + K_2O$ than the basaltic material (>4.5 wt%) and the potassic trend has lower Na_2O (<3.5 wt%) and high K_2O (>1 wt%). In this text, APXS targets that fall into the mugearitic and potassic ranges are respectively referred to as mugearitic and potassic rocks. As we discuss below (Section 5), the alkali-rich compositions are a continuum and the basaltic-mugearitic-potassic distinctions delineated here are for classification and discussion purposes.

Minor and trace elements also delineate trends within the alkali-rich units that are not apparent in other units. The mugearitic rocks, distinguished from the other Bradbury group targets by higher Na_2O content, tend to have lower MnO, Cr_2O_3 , and Ni than soil and other basaltic to potassic basaltic materials (Figure 10). Zinc in most of the mugearitic rocks (320 ± 270 ppm) is the same or lower than soil (310 ± 105 ppm). However, other rocks in the alkali-rich units have Zn enrichments that are commonly ~800 ppm and range up to 1,900 ppm. The drilled Windjana target has a remarkable Zn enrichment of ~4,500 ppm. The Zn-bearing phase was not identified by CheMin (Treiman et al., 2016) or SAM (Sutter et al., 2018). A possible veinlet, Stephen, located ~10 cm away from Windjana, has very high Zn ($8,160 \pm 250$ ppm), suggesting in situ Zn mobilization by fluids in the Kimberley formation (Berger et al., 2017). Germanium follows the same general trend as Zn, being enriched in the basaltic and potassic basaltic materials but not in the mugearitic rocks (Berger et al., 2017).

Ten targets grouped with the alkali-rich units deviate from the mafic/felsic mixing line defined by Mg/Si and Al/Si (Figure 8a). Et Then and Secure are float in the Bradbury group with high FeO (~27 wt%). Oscar and Ruker are Bradbury group targets with the high $Na_2O + K_2O$ (5–7 wt%) and low Ni (35–70 ppm) characteristic of mugearitic rocks, but relatively lower Al_2O_3 (9–11 wt%) results in lower molar Al/Si that differentiates the targets. Oscar, as well as the Bradbury-like float targets Little Devil, Sonneblom, and Zambezi, has FeO that is 15%–50% higher than similar alkali-rich rocks on the mafic/felsic mixing line (Figure 8a). One target, Wildrose, is float located in the Bradbury group ~125 m from the Pahrump Hills member and is probably from that unit. Two targets found in the Bressay deposit (Askival raster and Sanquhar sols 2015–2022) have unusual SiO_2 enrichments up to 66 wt%.

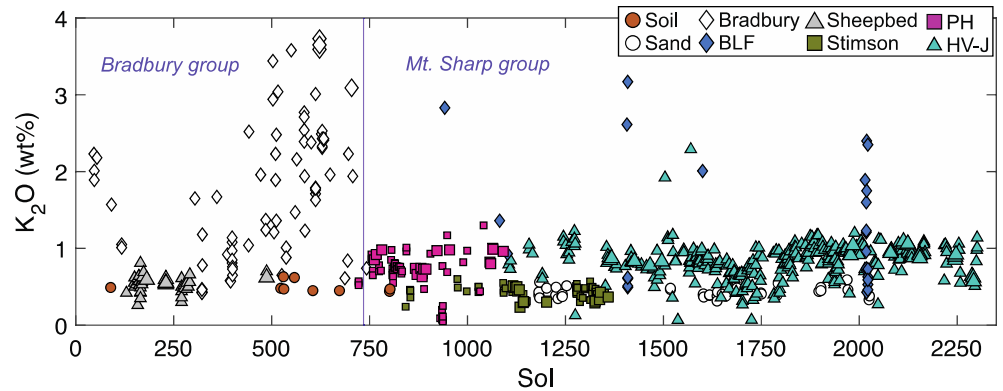


Figure 9. A plot of K_2O versus sol demonstrates the distribution of alkali-rich rocks along the traverse. The alkali-rich rocks in the Bradbury group are a mix of outcrop and float; all of the alkali-rich rocks discovered after sol ~ 750 on Mt. Sharp units are float (Bradbury-like float; BLF). The Bradbury/Mt. Sharp contact is indicated with the vertical line.

4.3.2. Mt. Sharp Group

From the base of lower Mt. Sharp to the end of the Vera Rubin ridge, the Mt. Sharp group targets were in the Murray formation, which contains seven members (Figure 1). The Pahrump Hills member and alkali-rich float have distinctive compositions and are discussed separately.

4.3.2.1. Murray Formation

The greatest thickness of strata explored by *Curiosity* has been the Murray formation bedrock of the Mt. Sharp group (Figure 1), which comprises most of the traverse from sol ~ 750 to sol 2,301 while climbing 320 m in elevation. The bedrock is primarily laminated mudstone. Some strata contain very fine sandstone mixed with siltstone and mudstone, and intermittent coarser sandstone lenses (e.g., Fedo

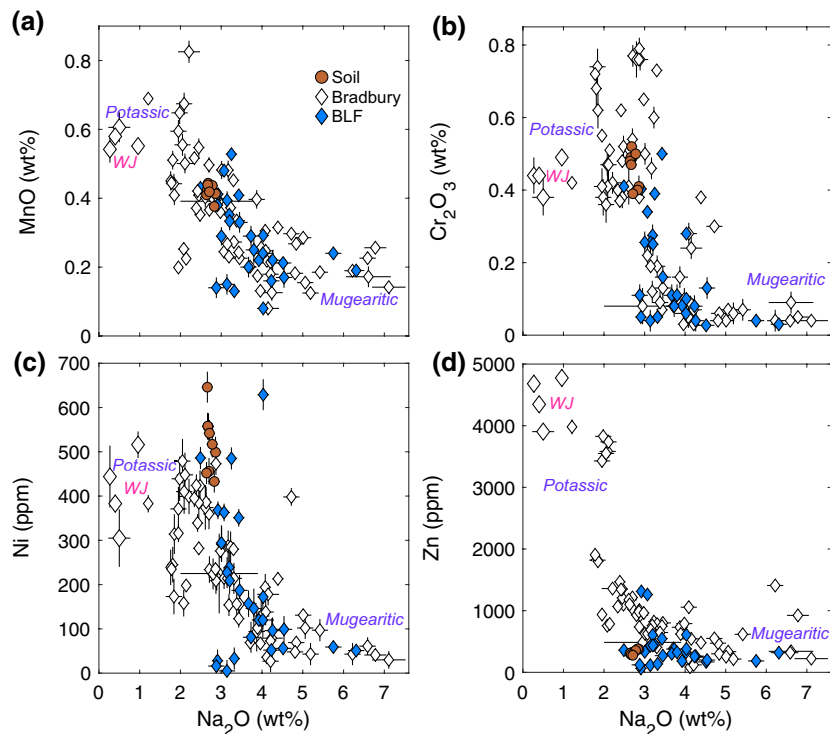


Figure 10. Selected minor and trace elements (a) MnO , (b) Cr_2O_3 , (c) Ni , and (d) Zn versus Na_2O in alkali-rich units. The four measurements of Windjana drill fines (WJ; larger symbols) are denoted.

et al., 2018; Stack et al., 2019). The Vera Rubin ridge (Pettegrove Point and Jura members) is an approximately linear, ~200–500-m-wide topographic feature explored over sols 1,800 to 2,301 (Edgar et al., 2020; Thompson et al., 2020). The raised Vera Rubin ridge is a step in topography, but the bedrock has thin planar laminae similar to much of the underlying Murray formation (Edgar et al., 2020). Diagenetic features are common and include white veins that cross-cut bedding planes (see Section 4.4.2) and concretions enriched in Mg, S, Fe, Mn, P, K, and Ni (e.g., Kronyak et al., 2019; Minitti et al., 2019; Sun et al., 2019; VanBommel et al., 2017, 2016).

The volatile-free composition of the Murray formation is basaltic and basaltic andesitic (Figure 4). However, Murray formation bedrock has notable differences from the other basaltic units. The Murray units are broadly distinguished chemically from average Mars by elevated SiO_2 (vein-free median is 48.0 ± 5.2 wt%) relative to soil (42.1 ± 0.5 wt%; Figure 4). The Si enrichment corresponds with a depletion in Mg, as evident in a plot of Mg/Si versus Al/Si (Figure 8b). For comparison, the basaltic and alkali-rich units define a mafic/felsic mixing line on this plot (Figure 8a), and the Murray formation deviates from this line. Note that there is a trend from low molar Mg/Si of the dust-free drill targets toward soil (0.30 ± 0.03), which is effectively the same as the dust (0.32 ± 0.06 ; Berger et al., 2016), that is likely caused by mixing with Mg-rich airfall dust on unbrushed rock surfaces (Figure S3). Most of the Murray bedrock, when prominent Ca-sulfate veins ($\text{SO}_3 > 15$ wt%) are omitted, is consistently low in Mn, Mg, and Ca, and high in K, P, Ni, and Zn relative to soil (Figures 7b and 7c). The units are also uniformly enriched in Ge (110 ± 25) by a factor of ~50 relative to martian meteorites and terrestrial basalts (Berger et al., 2017).

The Murray formation above the Pahrump Hills member has a relatively uniform composition, but there are small variations in elemental concentrations along *Curiosity's* traverse up the strata. Thompson et al. (2020) discuss the APXS results for the Murray formation in greater detail, including elemental variation with elevation and within the Vera Rubin ridge. These results can be used to refine interpretations of the geologic history of Gale crater, but they are beyond the scope of this study and are presented by Thompson et al. (2020). In summary, the relatively small elemental changes with elevation include as follows: (1) In the Karasburg, Sutton Island, and Blunt's Point members, the mean Si, Al, and Na concentrations are statistically the same, but mean Fe, Mn, and Zn concentrations increase with elevation. (2) Near the base of the Vera Rubin ridge, Si and Al correlate positively, whereas Al and Fe correlate negatively. (3) The Vera Rubin ridge has small differences in Si, Al, Ti, Fe, and Mn that differentiate red-toned bedrock from patches of gray bedrock.

Pahrump Hills Member

The stratigraphically lowest Pahrump Hills member has similar element enrichments and depletions compared to the overlying Murray formation members (Figure 7c). However, it is distinctive from other Murray formation members (Figure 1) for its higher Al_2O_3 (10.4 ± 2.3 wt%) relative to the overlying members (8.9 ± 0.76 wt%), resulting in a higher Al/Si for a given Mg/Si (Figure 8b). Due to the chemical distinctions between Pahrump Hills and the overlying members of the Murray formation, Pahrump Hills targets are plotted with different symbols in plots and denoted "PH". All of the Murray formation members above Pahrump Hills from Hartman's Valley to Jura have the same symbols in plots and are denoted "HV-J."

The Pahrump Hills member also contains unusual high-Si targets typified by the drill target Buckskin (sols 1,057–1,091; Figure 7d). The Buckskin target, which represents a high-Si facies within the Pahrump Hills member, ranges to significantly higher SiO_2 (74 wt%) than the typical Murray bedrock. This and ~8 other similar high-Si targets were limited to a <5 m thick part of the member. Considering major and minor elements, the soil-normalized element pattern of the Buckskin high-Si facies is broadly similar to the other Murray formation units, except that some of the relative enrichments and depletions are greater: Si and Ti are enriched, and Al, Fe, Mn, Mg, and Cr are depleted (Figure 7d). Key differences are Ni and Zn, which are enriched in the Murray formation, are both depleted in Buckskin. The SiO_2 enrichment and the associated depletion in MgO in Buckskin-like rocks leads to lower Mg/Si, deviating from mafic/felsic mineral trends in Mg/Si and Al/Si associated with igneous fractionation. Compared to the other Murray formation units, the high SiO_2 (73 ± 7 wt%) Buckskin high-Si facies of Murray has even greater depletions in MnO and MgO, as well as lower FeO, Al_2O_3 , and Na_2O . The CheMin XRD results for Buckskin reveal that the total bulk Si is associated primarily with tridymite (14 wt%) and the X-ray amorphous fraction (60 wt%; Morris et al., 2016). Morris et al. (2016) conclude that the tridymite indicates silicic volcanism (ash or detrital), arguing that low temperature formation (i.e., diagenetic) of this silica polymorph is kinetically inhibited.

Alkali-Rich Float

A limited number of alkali-rich rocks were found in the Mt. Sharp group as deposits of float (each roughly 0.01–0.03 km² in lateral extent) on top of the Murray formation. These deposits have Bradbury-like, alkali-rich compositions that are distinct from the Murray bedrock (denoted BLF for “Bradbury-like float;” Figure 9). An unusual, small float deposit was found on top of the Vera Rubin ridge at a waypoint named Bressay (Wiens et al., 2020) where 17 APXS measurements on nine different targets scattered over an area of ~70 m² were acquired (sols 2015–2022). The deposit includes mugearitic and potassic rocks nearly identical in composition to those found in the Bradbury group.

4.3.3. Siccar Point Group

The Siccar Point group targets measured by the APXS occur in the Stimson formation (Figure 1).

4.3.3.1. Stimson Formation

Outcrop of the Stimson formation was encountered intermittently over sols 975–1,350. The Stimson formation bedrock of the Siccar Point group unconformably overlies the Murray formation, and is comprised of coarse-grained, cross-bedded sandstone (Banham et al., 2018). The sandstone forms isolated, erosion-resistant outcrops and mesas with up to 4-m-thick strata (Banham et al., 2018). Crosscutting Ca-sulfate veins occur in the bedrock; however, they are less common in APXS analyses than in the Sheepbed member and Murray formation. Fracture-associated haloes also crosscut both the Murray and the Stimson formations (Yen et al., 2017b). The textures and stratigraphy are consistent with formation via lithification of an aeolian sand, and the relatively sharp contact with the underlying mudstone-dominated Murray formation indicates a period of erosion of the lithified Murray bedrock and a change in paleoclimate before deposition of the Stimson formation (Banham et al., 2018).

Excluding fracture-associated haloes (Section 4.4.1) the Stimson formation shares similar major element characteristics with soil, sand, and the Sheepbed member (Figure 7a; Data Sets S1 and S2). The Stimson formation has a basaltic composition (Figure 4), and the plot of Mg/Si versus Al/Si (Figure 8c) overlaps with soil on the inferred igneous mixing line. Several targets, including the Big Sky drill tailings, have higher Al/Si in Figure 8c, which is attributed to higher Al₂O₃ at approximately the same SiO₂. Volatile elements SO₃ and Cl have similar concentrations and molar ratios as the Sheepbed member (Figure 5), which are enriched relative to the average basaltic crust but not as narrowly constrained as soil and sand.

In the Stimson formation, trace elements and MnO are soil-like, which is unlike the Sheepbed member and Murray formation. The Stimson formation has Ni (460 ± 70 ppm), Zn (315 ± 150 ppm), MnO (0.39 ± 0.05 wt%), and FeO/MnO (50 ± 5) that are within the same range as soil. Exceptions are five targets with Zn > 600 ppm, and these are located laterally on the traverse <10 m away from contacts with the Murray formation, thus they may represent incorporation of Murray detritus into the Stimson bedrock and/or mobilization of Zn across the contact in diagenetic fluids (Berger et al., 2017). Germanium is below the LOD of ~30 ppm in the Stimson formation, as it is in soil and sand (Berger et al., 2017).

4.4. Selected Mobile Element Trends

A number of features and trends highlight element mobility in the units investigated by *Curiosity* and are key to interpreting the history of Gale crater. In this section we present results and give an overview of the characteristics, occurrence, and distribution of the most prominent features and trends: (1) fracture-associated haloes, (2) sulfur, (3) chlorine and bromine, (4) and phosphorus.

4.4.1. Fracture-Associated Haloes

Fracture-associated haloes enriched in Si were discovered in Gale crater, and two that occur in the Stimson formation were investigated in detail with a drill campaign (Yen et al., 2017b). The ~50-cm-wide haloes have a lighter tone than the host bedrock and occur surrounding a central fracture that cross-cuts strata. The halo targets trend toward the origin in a Mg/Si versus Al/Si plot in a similar manner to what is ob-

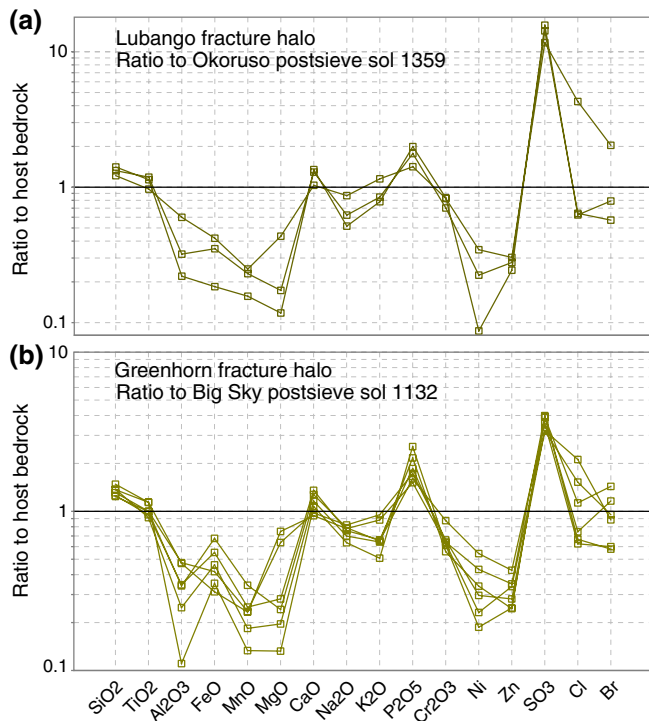


Figure 11. Element ratios of the (a) Lubango and (b) Greenhorn silica-rich haloes normalized by the adjacent, less altered host Stimson formation bedrock.

served in the Murray formation bedrock because Mg and Al are lower, relative to Si (Figure 8c). Element gains and losses, relative to the less altered adjacent host bedrock, are well-characterized because two fractures were investigated by analyzing the halo and adjacent, less altered bedrock within ~ 1 m. Compared to the host Stimson bedrock, the haloes are enriched in Si, Ti, P, and S, and depleted in Al, Fe, Mn, Mg, Ni, Zn, and Cr (Figure 11). The element ratio pattern is notably similar to that of the Buckskin targets (Figure 7d). However, unlike Buckskin, the crystalline material in the two drilled halo samples, Greenhorn and Lubango, does not contain detectable tridymite (< 1 wt%) and contains 20–25 wt% $\text{CaSO}_4 \cdot n\text{H}_2\text{O}$ minerals (Yen et al., 2017b). Note that crystalline material comprises only ~ 25 –35 wt% of the halo samples and 50 ± 15 wt% of the Buckskin sample (Morris et al., 2016; Yen et al., 2017b). The silica-rich haloes crosscut the Stimson formation as well as the Murray formation. Two targets at one halo in the Hartmann's Valley member were investigated: Ferdig and Cody, which are < 1 m apart and the latter is in lighter-toned rock. Ferdig and Cody have similar relative element trends as the Stimson haloes, with Cody being enriched in silica. Light-toned fracture haloes were also observed in Mastcam images of the Bradbury group (Gabriel et al., 2019); however, these were not investigated further with the APXS.

4.4.2. Sulfur

Sulfur is a major element (> 1 wt%) in nearly all Gale crater materials (Data Set S1). Most targets (72%) thus far have SO_3 concentrations that fall into the same range found in sand, soil, and dust (2.3–8.3 wt%). Twenty-five percent of APXS targets have higher SO_3 concentrations (up to 44 wt%). Concentrations below 2 wt% were discovered in only four targets, including

the basaltic Stimson formation drill target Okoruso ($\text{SO}_3 = 0.65 \pm 0.03$ wt%). Sulfur has clearly been mobile in Gale, as evidenced by geochemical associations discovered in the Gale bedrock, including associated diagenetic features (e.g., Kronyak et al., 2019; Sun et al., 2019).

The highest concentrations of S occur in white fracture- and void-filling material, which is common, to varying degrees, in all of the Gale crater units (e.g., Kronyak et al., 2019; Nachon et al., 2014; Sun et al., 2019). Not all rock types have white veins; for example, the mugearitic JakeM class rocks (Schmidt et al., 2014; Thompson et al., 2016) do not have sulfate veins or nodules. Nearly all of the 44 targets with SO_3 contents > 15 wt% have positive correlation between SO_3 and CaO at a ratio that approaches the CaO: SO_3 weight ratio of Ca-sulfate ($\sim 3:2$; Figure 12). An exception is the Garden City vein complex (GC; sols 930–948), which is a mixture of white (Ca + S)-rich material and dark Ca-rich material (VanBommel et al., 2017; Kronyak et al., 2019). White, cross-cutting and/or concordant veins (i.e., parallel with bedding planes; Figure S4) were visually confirmed in MAHLI and Mastcam images of 39 of the 44 high-S targets ($\text{SO}_3 > 15$ wt%). Five were ambiguous in the imagery, but we interpret the high (Ca + S) to be due to the same white material (Data Set S1). Therefore, the white vein material in the APXS FOV is the source of the high S concentrations for 90%–100% of targets with $\text{SO}_3 > 15$ wt%. Targets with intermediate SO_3 content (~ 5 –15 wt%) also typically have elevated CaO and thin (~ 1 –2 mm) white veins in the APXS FOV. The consistent CaO: SO_3 weight ratio ($\sim 3:2$) in vein-bearing targets, and the confirmation of crystalline Ca-sulfate phases (anhydrite, bassanite, and gypsum) in CheMin XRD analyses (e.g., Bristow et al., 2018; Vaniman et al., 2014), provide strong evidence that the white, cross-cutting and concordant veins observed by the APXS are Ca-sulfate. The predominant hydration state of the veins on the surface is likely bassanite (Rapin et al., 2016). The mudstone-dominated units (Sheepbed member and Murray formation) have the greatest density of veins, which is evident in the distribution of CaO and SO_3 in the Gale stratigraphy (Figure S5). As stated above, the tactical APXS operations group typically and intentionally avoids veins, and thus the actual distribution of Ca-sulfate veins is not necessarily reflected accurately in the APXS dataset (e.g., Mi-

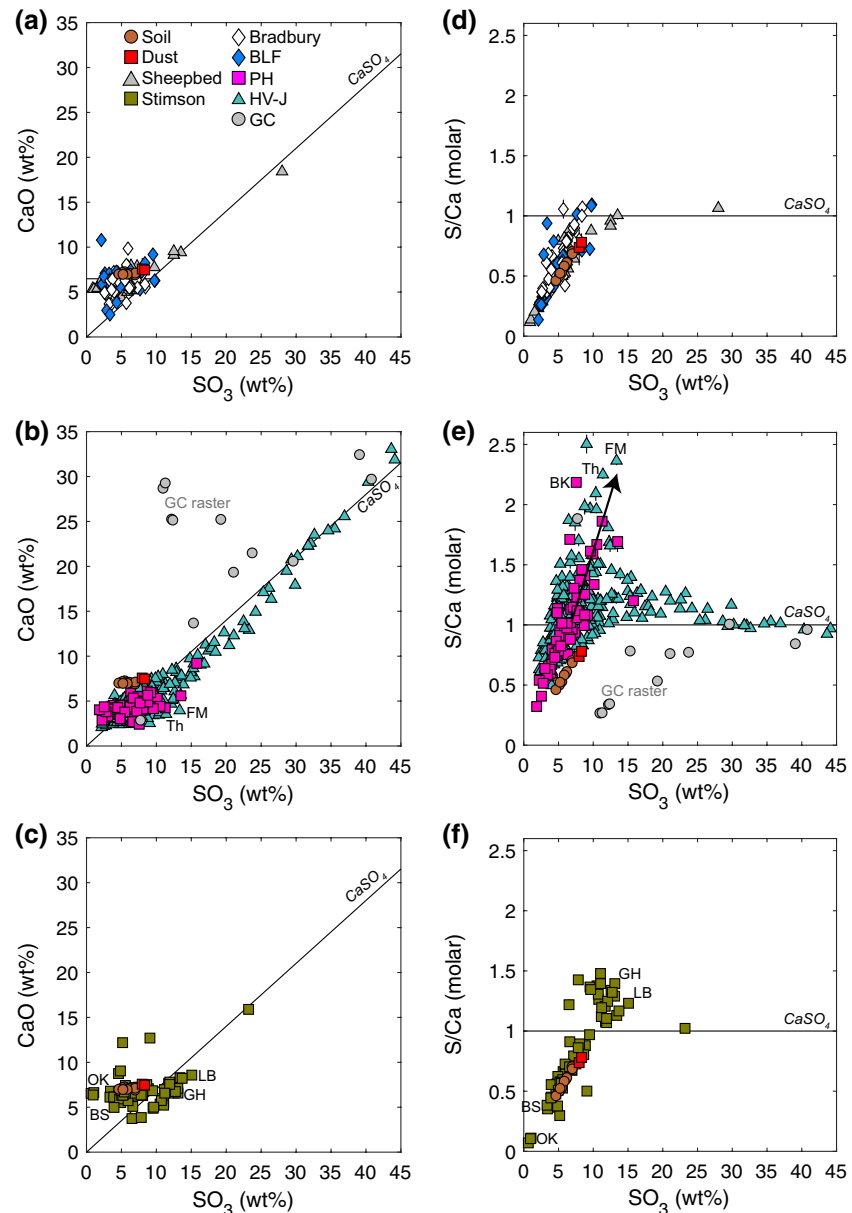


Figure 12. Calcium and S/Ca versus sulfur in alkali-rich units (a and d), the Murray formation (b and e), and the Stimson formation (c and f). The black line indicates stoichiometric CaSO_4 and the arrow in (e) denotes a possible mixed-cation sulfate addition trend. Rasters of Mg-sulfate features are omitted; see Figure S6. The high K_2O and FeO targets Thrumcap (Th) and Fresh Meadow (FM), the Garden City raster points (GC; sols 930–948), and selected drill targets are denoted.

nitti et al., 2019). Notably, bedding-concordant veins are common in the Blunt's Point member and these were analyzed frequently by the APXS because they were difficult to resolve and identify in Navcam and Mastcam targeting images.

Note that Figures 12b and 12e show an apparent systematic enrichment of SO_3 relative to CaO because most of the SO_3 -rich targets plot on the higher- SO_3 side of the CaO: SO_3 (1:1) line. Some of the SO_3 enrichment in targets with $< \sim 30$ wt% SO_3 is attributed to matrix effects arising from the necessary but incorrect assumption used in APXS analysis that the matrix is homogeneous on the submicrometer scale (Berger et al., 2020). The heterogeneous matrix effect is estimated to cause SO_3 concentrations to be $\sim 5\%$ – 30% high when the

APXS FOV includes sulfate and silicate (Berger et al., 2020). However, the effect does not account for all of the excess sulfur with respect to Ca-sulfate, as evident in targets with S/Ca >1.3 (Figure 12e).

Sulfur is also associated with elements other than Ca in localized features. Dendritic and subspherical concretions (~1 cm) in the Pahrump Hills and Hartmann's Valley members were analyzed with APXS rasters and show a positive correlation between MgO and SO₃ (Figures S4d, S4e, and S6a; VanBommel et al., 2016, 2017). Deconvolution of the rasters using MAHLI image analysis indicates that the concretions are a mixture of the adjacent bedrock with ~10%–15% pure MgSO₄ (VanBommel et al., 2017). Nickel is also highly enriched (up to 4,000 ppm) in most, but not all of the concretions (Figure S6b). The concretions are interpreted to be Mg-sulfates that precipitated from diagenetic fluids in situ (Sun et al., 2019; VanBommel et al., 2017). The Mg-sulfate concretions are not as widespread as the Ca-sulfates; they are limited to the Pahrump Hills and Hartmann's Valley members. Mg-sulfate concretions occur in the Stimson formation (Sperrgebiet; sol 1,277), but they are limited to within a few lateral meters from the Stimson/Hartmann's Valley contact. Distinct from the Mg-sulfates, two S-rich fracture-associated features found in the Murray formation occur with elevated K₂O and FeO (Fresh Meadow and Thrumcap; sols 1,504 and 1,520). We reiterate that the APXS dataset does not represent the true distribution of these features. For example, there were locations in the vicinity of Pomona when there were extensive concretions, but they were outside the workspace reachable by the rover's arm.

Sulfur is a component of the matrix of Gale bedrock (Figure 13). Correlation of CaO and SO₃ indicate that Ca-sulfate is present (Figure 13a). Evidence in CheMin XRD analyses suggests that the matrix of 9 of 12 Murray formation samples and the Stimson formation fracture haloes contain >1 wt% crystalline Ca-sulfates, although very thin Ca-sulfate veins possibly intersected by the drill cannot be ruled out (Bristow et al., 2018; Rampe et al., 2017; Vaniman et al., 2014; Yen et al., 2017b). However, the coupling of S with Ca in sulfates does not account for all of the sulfur in Gale bedrock. This is apparent in Figure 12e (arrow), where targets with elevated SO₃ do not necessarily trend toward the corresponding 1:1 molar S:Ca ratio expected from simple addition of Ca-sulfate (Figure S7). Evidence of Mg-sulfates in Murray formation nodules suggests that they could be present in the bedrock matrix; however, there is no direct evidence of widespread Mg-sulfate in the bedrock matrix (Figure 13b). Deconvolving Ca-sulfate from other possible S-bearing phase(s) is challenging with APXS alone, but the APXS analysis of CheMin XRD samples enables the allocation of sulfur between crystalline and amorphous phases (e.g., Morrison et al., 2018). Combined results from the APXS and CheMin show that ~50%–90% of the bulk S in bedrock samples is associated with the X-ray amorphous fraction in the bulk sample (Table S1).

Some of the S X-ray signal in APXS analyses is attributed to airfall dust (Schmidt et al., 2018), which contains 8.3 ± 0.4 wt% SO₃ (Berger et al., 2016). The effects of dust on APXS analyses are discussed in detail by Schmidt et al. (2018), but the APXS analyses of drill fines extracted from drill holes of 2–6 cm depth, in concert with CheMin and SAM results, confirm that sulfur is a major component of most Gale bedrock units, and S results are *not* simply a measurement of dust. For example, the vein-free bedrock of the Hartmann's Valley and Karasburg members, which have relatively small variations in elemental compositions, do not have any apparent overall differences in SO₃ concentrations between unbrushed, brushed, and drill fines targets (Figure S8).

4.4.3. Chlorine and Bromine

Chlorine concentrations in Gale vary by an order of magnitude, ranging from 0.28 ± 0.01 wt% in the Buckskin drill fines up to 3.44 ± 0.09 wt% in an unusual, relatively erosion-resistant veinlet named Stephen (Figure 14a). Bromine also varies widely, with 44 targets below ~30 ppm and more than 15 targets with Br concentrations of 1,000–2,000 ppm (Figure 14b). The two elements are not well-correlated with each other, consistent with findings elsewhere on Mars (Haskin et al., 2005). For example, the diagenetic target Jones Marsh has the second-highest Cl in Gale (3.10 ± 0.09 wt%) but relatively low Br concentrations (155 ± 15 ppm). Despite lacking a clear correlation in absolute concentrations, Cl and Br are both consistently enriched in unbrushed and brushed surface targets compared to material exposed from depths of >1 mm by the drill (Figure 15). The Cl concentration in drilled material (0.56 ± 0.28 wt%) is about half of the Cl concentration in unbrushed surfaces (1.23 ± 0.51 wt%) and brushed surfaces (1.06 ± 0.54 wt%). The same difference in median Br concentrations is found between the surface (160 ppm) and the drilled material (70 ppm).

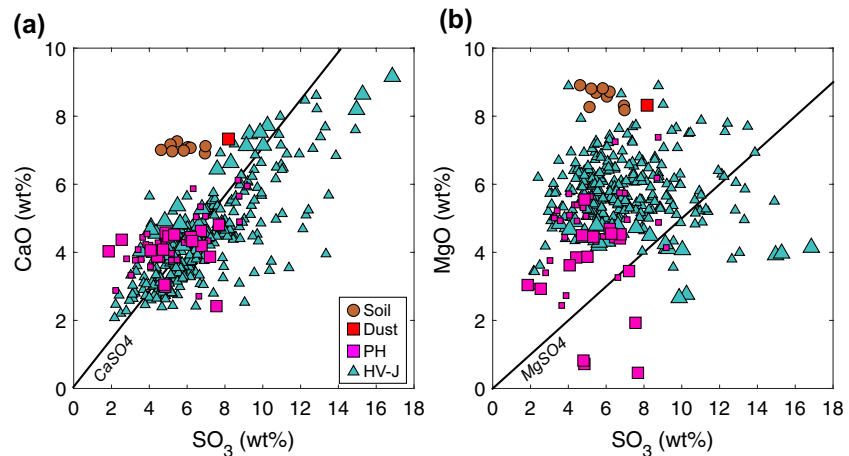


Figure 13. Variation of (a) CaO and (b) MgO with SO_3 in Murray formation bedrock. Drill fines are denoted by larger symbols. The pure mixing lines of MgSO_4 and CaSO_4 are shown. Targets with Ca-sulfate veins and rasters of Mg-sulfate concretions are omitted; see Figure S6. The CaO and SO_3 correlation is evidence of Ca-sulfate in the bedrock matrix, although the influence of small veins (<1 mm) or unseen veins are difficult to assess with Mars Hand Lens Imager (MAHLI) imagery.

Elevated Cl at the surface (<1 mm depth) leads to the question: is the Cl analysis dominated by Cl-rich dust? Dust has a Cl concentration of 1.08 ± 0.12 wt% (Berger et al., 2016), which is within the range of the *median* unbrushed and brushed surface concentrations. However, the distinctive S/Cl ratio of 3.4 ± 0.2 in dust (and soil) discussed above (Section 5.1) is not consistent with the surface targets. Excluding targets with S-rich veins and concretions, the median S/Cl of surface targets is 2.2 ± 1.1 (Figure 15) because Cl is commonly higher at a given SO_3 concentration than that found in dust and soil. We interpret this difference in S/Cl to be an indication that the APXS analysis of Cl on the surface is not simply dust; Cl is enriched at the surface of most bedrock relative to drilled material. Similar observations of elevated Cl

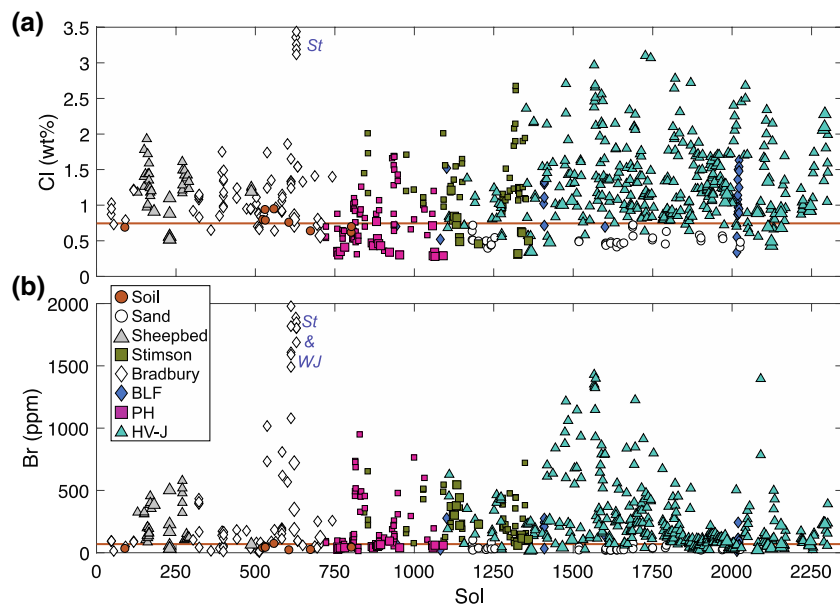


Figure 14. (a) Chlorine and (b) bromine concentrations versus sol for all Gale crater targets. Highly enriched targets Windjana (WJ; sols 612–704) and Stephen (St; sols 627–629) are indicated, and the brown line denotes the median soil concentration.

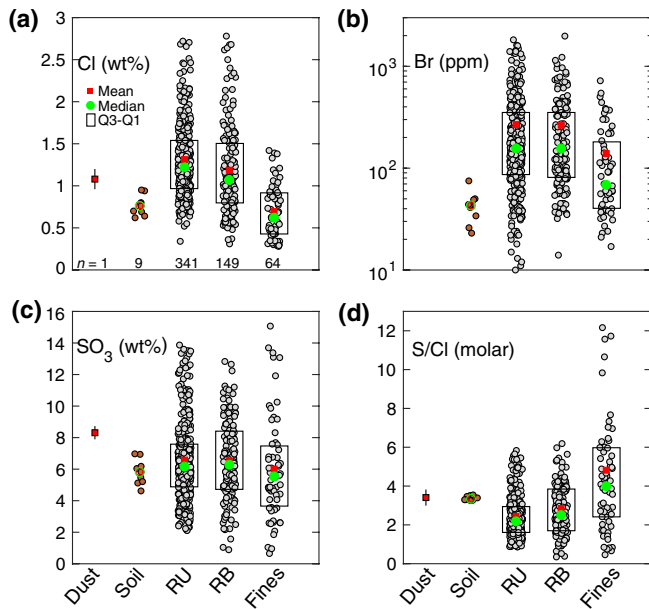


Figure 15. Evaluation of target preparation methods (i.e., brushing and drilling) with respect to the (a) Cl, (b) Br, (c) SO₃, and (d) molar S/Cl in dust, soil, unbrushed (RU), brushed (RB), and drilled (fines) APXS targets. Sulfur- and chlorine-rich veins, concretions, and other diagenetic features are omitted. The number of targets (*n*) for each category is shown in (a). The red square is the mean, the green square is the median, and the box contains the middle 50% of the data.

on rock surfaces were made by the MER APXS analyses of unbrushed, brushed, and abraded surfaces (Haskin et al., 2005).

Chlorine and bromine analyses do not show any systematic geochemical association with any other single element in the Gale bedrock. For instance, considering only the 67 measurements of bedrock drill fines, neither Cl nor Br have clear correlations ($-0.55 < r < 0.47$) with any of the other 14 elements reported here. The same results hold for the unbrushed and brushed rock surfaces ($-0.50 < r < 0.50$) when evaluated by the separate groupings discussed herein (Sheepbed, Bradbury, PH, HV-J, Stimson). The HV-J units of the Murray formation have a very weak positive correlation between molar Cl and Na ($r = 0.43$) that may indicate halite; Cl and K are not correlated ($r = 0.01$) thus KCl does not control Cl concentrations if present (Figure 16). The lack of Cl and Br correlation with a single cation in the bedrock indicates that chloride and oxychlorine species are associated with multiple cations (e.g., Na, Mg, K, and Ca). Mixed chloride and oxychlorine species are consistent with the findings of the Phoenix and MSL missions. Analysis of the Phoenix Wet Chemistry Laboratory experiments revealed evidence of perchlorate mixtures of $\sim 60\%$ Ca(ClO₄)₂ and $\sim 40\%$ Mg(ClO₄)₂ (Kounaves et al., 2014). Evolved gas analysis of Murray formation bedrock by SAM resulted in O₂ peaks from oxychlorine phases that could be consistent with a mixture of Ca(ClO₄)₂, Mg(ClO₄)₂, and Mg(ClO₃)₂ (Sutter et al., 2018). However, the HV-J Murray drilled samples do not show chlorate/perchlorate detections in SAM analyses (Sutter et al., 2018). Akaganeite, a possible Cl-bearing mineral [FeO(OH,Cl)], was also detected by CheMin in the Sheepbed mudstone (1–2 wt%; Vaniman et al., 2014) and in the VRR sample Rock Hall (~ 7 wt%; Rampe et al., 2020b).

Targets with the highest halide concentrations are localized features (i.e., veins and patchy coatings/rinds) and have geochemical associations with multiple elements. In the Bradbury group, the target Stephen, an approximately 10-cm-wide, linear ridge (likely a veinlet) adjacent to the Windjana drill site, has the highest Cl concentration discovered by the APXS on Mars (3.36 ± 0.04 wt%). Stephen also has remarkable enrichments in MnO (4.05 ± 0.03) and Zn ($8,160 \pm 250$ ppm; Berger et al., 2017; Thompson et al., 2016; VanBommel et al., 2016). Similarly, an APXS raster of the Garden City vein cluster has evidence of an association between Cl, MnO, and Zn, all of which are enriched (1.88 wt%, 1.01 wt%, and 2,438 ppm, respectively) in an uncommon, dark vein-filling material by 3–4 times relative to the adjacent bedrock (Berger et al., 2017; VanBommel et al., 2017). Jones Marsh (sol 1727), a patchy cm-scale darker-toned crust, is another example, having very high Cl (3.1 wt%), P₂O₅ (7.6 wt%), and MnO (4.0 wt%). These diagenetic features indicate the mobility of Cl in postdepositional fluids, which is key to understanding the aqueous history of Gale because chloride is a conservative element in aqueous solutions (e.g., Garrels & Christ, 1965; Garrels & MacKenzie, 1967). Additionally, halide species (e.g., perchlorate, chlorate, and chloride) may act as an oxidant and/or complexing ligand (e.g., Marion et al., 2010), and their presence at high concentrations likely impacted geochemical processes on the martian surface.

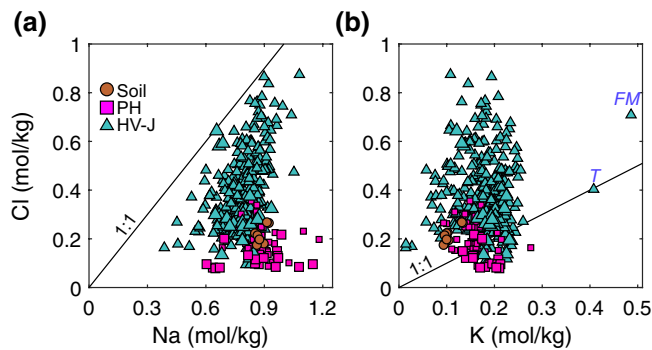


Figure 16. Molar Cl versus (a) Na and (b) K in Murray formation targets. The HV-J members have a weak positive correlation between Cl and Na ($r = 0.43$) and no correlation between Cl and K ($r = 0.01$). The 1:1 line shows the pure NaCl and KCl mixing lines. The K-rich targets Thrumcap (T; sol 1,504) and Fresh Meadow (FM; sol 1,570) are indicated and larger symbols denote drill fines.

4.4.4. Phosphorus

Systematic differences in P concentrations and evidence of P mobility have emerged along *Curiosity's* traverse. The Sheepbed member, Stimson formation (excluding the altered haloes), and alkali-rich sedimentary units all have a relatively limited range of P₂O₅ concentrations

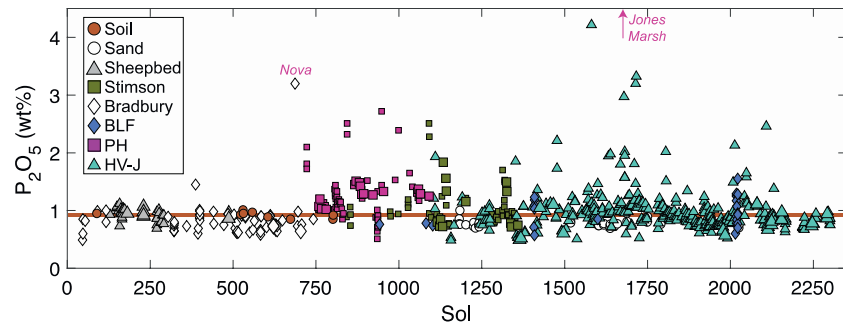


Figure 17. P_2O_5 versus sol. The unique, high P_2O_5 target named Nova is denoted (sol 687) and the target named Jones Marsh (sol 1727; indicated by arrow) with very high P_2O_5 (7.56 ± 0.40 wt%) is not shown. The brown line denotes the median soil concentration.

(0.88 ± 0.22 wt%; Figure 17), and there is no overall correlation of P_2O_5 in these units with any of the other 15 elements reported here. As such, small amounts of apatite are not detectable with P correlations with Ca and Cl. The alkali-rich units of the Bradbury group have lower P_2O_5 (0.80 ± 0.16 wt%) than the Sheepbed member and Stimson formation (0.92 ± 0.09 wt%). Limited and/or localized apatite enrichment in the alkali-rich units is suggested by the P_2O_5 enriched float targets Nova (sol 687), Rucker (sol 387), and Waternish (sol 2022). Nova has high CaO and P_2O_5 (9.8 and 3.2 wt%, respectively), and Rucker and the Waternish raster have elevated P_2O_5 (~ 1.5 wt%).

The CaO: P_2O_5 slope of these targets is consistent with the addition of apatite to a Ca-bearing rock, and they are interpreted to be igneous rocks with elevated apatite content (Figure S9). In contrast with the Bradbury group, the Murray formation has greater P_2O_5 variance (Figure 17). The Pahrump Hills member has slightly higher median P_2O_5 (1.25 ± 0.33 wt%) than the overlying Murray members (0.93 ± 0.52 wt%). Some of the Pahrump Hills rock targets with elevated SiO_2 (>53 wt%) have higher P_2O_5 (1.5–2.5 wt%; Figure 18a).

Phosphorus enrichments occur in localized features in the Murray formation and in the Stimson fracture haloes (Figure 18b). Dark gray nodules and patches on bedrock (e.g., Timber Point, Maple Spring, Berry Cove, and Jones Marsh) have correlated enrichments in MnO (0.8–4.0 wt%) and P_2O_5 (3.0–7.5 wt%; Figure S10a). Another occurrence of P enrichment is in the Garden City vein complex, where the target Kern Peak, interpreted to be altered vein-hosting bedrock (Berger et al., 2017), has elevated P_2O_5 (2.72 ± 0.14 wt%). The silica-rich fracture haloes in the Stimson formation have elevated P_2O_5 (up to 2.51 wt%), which represents a 185% enrichment relative to the less-altered adjacent bedrock (Figures 18b and S10b). Assuming TiO_2 has low mobility in diagenetic fluids under most Eh-pH conditions (e.g., Young & Nesbitt, 1998), the increase of molar P/Ti from 1.1 ± 0.1 in the Stimson bedrock to ~ 1.6 –1.9 in the altered haloes indicates an addition of P during formation of the haloes (Yen et al., 2017, p. 04).

5. Discussion

The APXS results demonstrate compositional diversity in Gale crater sedimentary bedrock and unconsolidated float, including elemental compositions that were not predicted to occur on Mars. Below, we discuss how the results are relevant to the primary objectives of the APXS investigation, which seeks to deduce the provenance of sedimentary materials in the crater, infer the paleoclimate, establish if liquid water was stable for extended periods, and constrain the geochemical conditions of ancient liquids. First, we compare compositions with igneous models to constrain the provenance of the materials in Gale crater. Then, we discuss the chemical evolution of the sedimentary units.

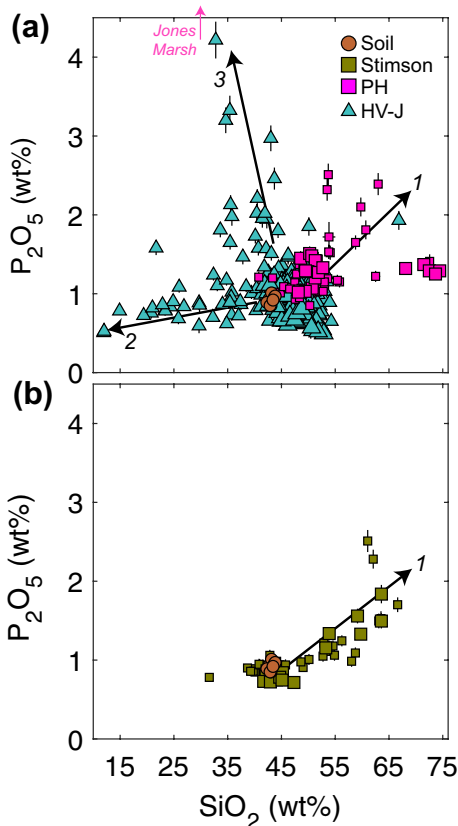


Figure 18. P_2O_5 versus SiO_2 in (a) Murray formation and (b) Stimson formation rocks. The black arrows indicate three trends: (1) bedrock with elevated SiO_2 and P_2O_5 primarily in the Pahrump Hills member and Stimson formation Si-rich haloes, (2) bedrock with prominent Ca-sulfate veins in the FOV, and (3) localized, P-rich diagenetic features in the HV-J Murray members. The red arrow denotes the SiO_2 content of the Jones Marsh with very high P_2O_5 (7.56 ± 0.40 wt%).

5.1. Comparison With Igneous Models to Constrain Provenance

Comparison of the APXS results with igneous geochemical models is useful for constraining the provenance of the sedimentary units in Gale crater, and for discerning secondary alteration and salt-forming processes. Below, we consider igneous models for the units with basaltic chemical characteristics, and then discuss igneous models for the alkali-rich rocks.

5.1.1. Igneous Signatures of the Basaltic Units

The units with basaltic chemical characteristics include soil and sand, the Sheepbed member at Yellowknife Bay, the Murray formation, and the Stimson formation. First, we consider the molar element ratio:

$$(0.25 * \text{Al} + 0.5 * \text{Fe} + 0.5 * \text{Mg} + 1.5 * \text{Ca} + 2.75 * \text{Na}) / \text{Ti} \quad (1)$$

which models the fractionation and/or crystal sorting via magmatic evolution of rocks with a mineral assemblage containing olivine (OL), plagioclase (PL), and clinopyroxene (CPX; Stanley & Madeisky, 1996). A positive correlation of Equation 1, denoted $(\text{OL} + \text{CPX} + \text{PL})/\text{Ti}$, with molar Si/Ti and a slope of ~ 1 indicates igneous fractionation of basalt (basalt control line; Figures 19a–19c). Most cases of open system alteration cause points to deviate from the 1:1 basalt control line. The geochemical indicator is thus sensitive to the addition of major elements (e.g., silica, Fe-oxides, and sulfates) and removal of major elements via dissolution and leaching. A second element ratio model is molar $(\text{Fe} + \text{Mg})/\text{Al}$ versus Si/Al (Figures 19d–19f), which can indicate an olivine control on element concentrations when targets plot with a 2:1 slope (Barnes et al., 2004). That is, more or less olivine has a control on the major elements in the model. Deviation from the 2:1 olivine control line indicates open-system alteration.

Using chemical models intended for igneous systems to evaluate sedimentary materials has several caveats. These geochemical indicators are not sensitive to closed system (isochemical) alteration, and crystalline and amorphous alteration products can preserve the bulk chemical composition of the parent material. Sedimentary *sorting* or *mixing* can simulate igneous fractionation in the basalt and olivine control models: (1) if sediment from a basalt protolith is *sorted* such that mafic and felsic components are separated into different deposits, then we would observe an increased range of compositions on the basalt and olivine control lines; (2) if sediment from a low alkali basalt is *mixed* with sediment from a high alkali basalt, then we would observe a range of intermediate compositions on the basalt and olivine control lines. Because of the ambiguity introduced by overlapping igneous and sedimentary processes, the range of values observed on the control lines should be interpreted conservatively. Nevertheless, in the absence of open-system alteration that adds or removes detectable elements, the igneous signature of basalt is likely to be preserved because the chemical compositions will follow the control lines.

Compared to the basalt and olivine models, soil, sand, and the Sheepbed mudstone have a relatively narrow range of elemental concentrations that are consistent with materials derived from basalt (Figures 19a and 19d). The Stimson formation bedrock has the same range of compositions, with two exceptions (Figures 19c and 19f). First, the fracture-associated haloes deviate from the basalt and olivine models, reflecting the depletion of Al, Fe, Mn, and Mg relative to the less-altered bedrock (Figure 11; Section 4.4.1). Second, several targets (Big Sky, Kwakwas, and Nomeib) have 20%–40% higher Al_2O_3 than soil and other Stimson formation bedrock, resulting in a lower Si/Al , which may indicate minor alteration. Overall, the Sheepbed member and Stimson formation share the geochemical signatures of basalt. Therefore, the provenance of the two sedimentary units was very likely basalt with a composition similar to the soil and sand.

The Murray formation deviates from the basalt and olivine chemical control models in three ways (Figures 19b and 19e). First, the apparent depletion of Mg and Ca, and the enrichment in Si in the large number of vein-free bedrock targets ($n \sim 325$; Figures 7b and 7c) results in lower molar $(\text{OL} + \text{CPX} + \text{PL})/\text{Ti}$ and $(\text{Fe} + \text{Mg})/\text{Al}$. Second, the Buckskin high-Si facies has very low $(\text{OL} + \text{CPX} + \text{PL})/\text{Ti}$ and very high Si/Al . Third, localized diagenetic features with high Fe (e.g., Morancy Stream, Newport Ledge, and Sagadahoc Bay) have corresponding high $(\text{OL} + \text{CPX} + \text{PL})/\text{Ti}$, and the Ti-depleted Haroldswick raster has high Si/Ti . The Murray formation observations support the interpretation that the bedrock has a basaltic provenance, but the deviations from basaltic compositions (e.g., lower Ca and Mg, higher K, P, and Zn; Figures 7b and

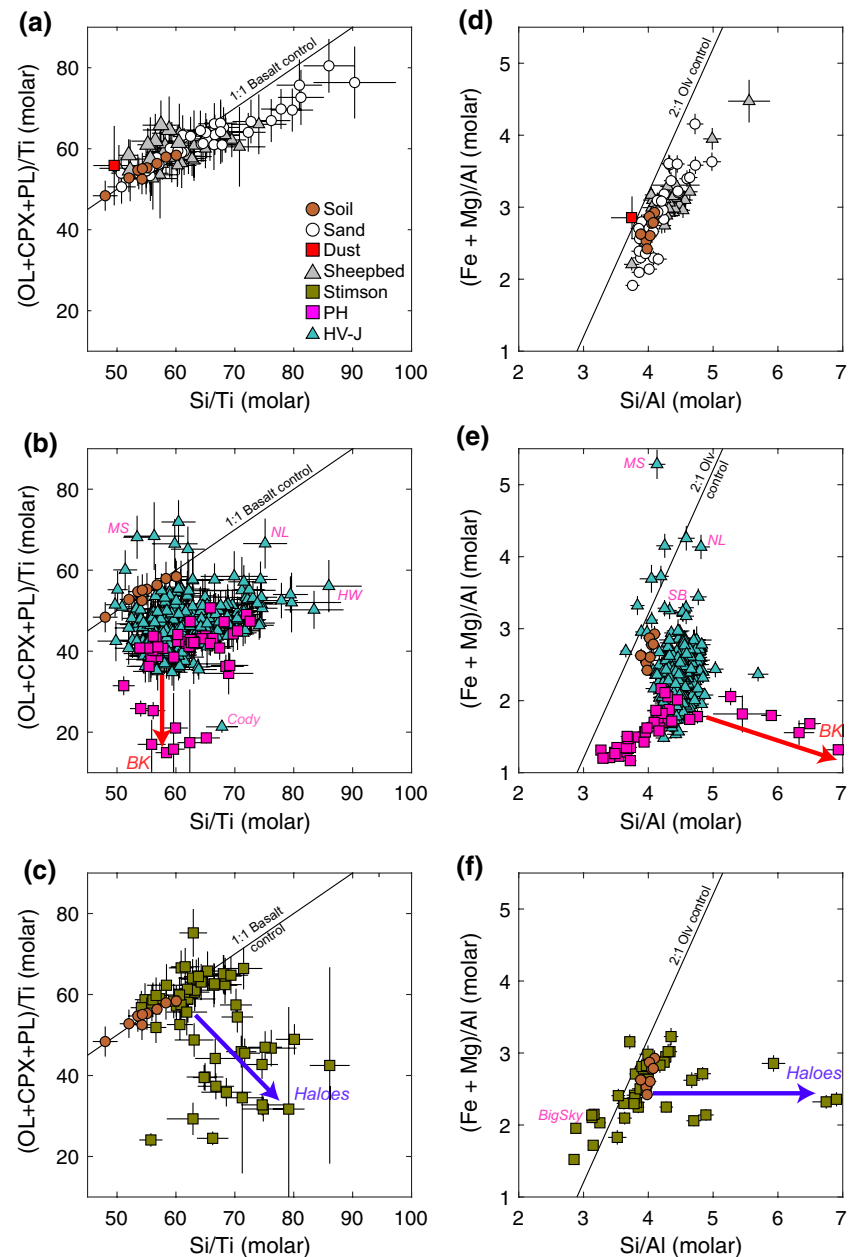


Figure 19. Element ratio indicator plots for fractionation and/or sorting trends in (a–c) a basaltic mineral assemblage containing olivine, clinopyroxene, and plagioclase (OL + CPX + PL) and (d–f) olivine, showing the APXS results for the basaltic units. Ca-sulfate veins are omitted, and the units are shown separately for clarity: (a and d) soil, sand, dust, and the Sheepbed member, (b and e) the Murray formation, and (c and f) the Stimson formation. The Buckskin (BK) and fracture halo trends are indicated by the red and blue vectors, respectively. For clarity, the full range of Si/Al values for BK (up to 13) and the Stimson haloes (up to 18) is not shown in [f], see Figure S11 for full range). Selected diagenetic features are denoted: Fe-rich Morancy Stream (MS), Newport Ledge (NL), and Sagadahoc Bay (SB); Ti-depleted Haroldswick raster (HW).

7c) point to widespread open-system alteration (Hurowitz et al., 2017; Rampe et al., 2017). The geochemical evidence and implications of this are addressed further in Section 5.2.

5.1.2. Igneous Signatures of the Alkali-Rich Units

The variable compositions of the alkali-rich Bradbury group (Section 4.3.1.2) and Bradbury-like float on the Murray formation (Section 4.3.2.1) suggest a diverse provenance for the sedimentary materials in Gale

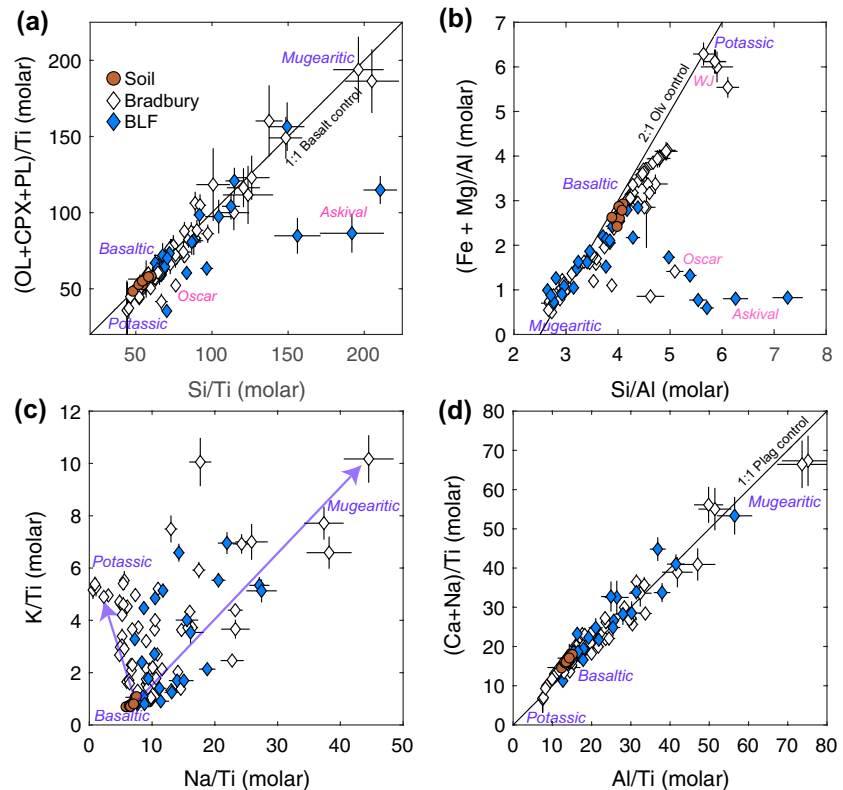


Figure 20. Element ratio indicator plots for fractionation and/or sorting trends in (a) basaltic minerals (OL + CPX + PL), (b) olivine, (c) alkali feldspar, and (d) plagioclase, showing the APXS results for the alkali-rich units. Three endmembers that delineate trends discussed in the text are denoted: basaltic, mugearitic, and potassic. Geochemical control lines are shown (Stanley & Madeisky, 1996). Targets with Ca-sulfate veins are omitted.

crater. The Bradbury group compositions are similar to igneous compositions found on Earth (Schmidt et al., 2014; Stolper et al., 2013; Thompson et al., 2016; Treiman et al., 2016) and drilled samples at Windjana and at John Klein/Cumberland contain abundant igneous minerals (Treiman et al., 2016; Vaniman et al., 2014), including pyroxenes and feldspars, suggesting the sediments are sourced from igneous terrains. The basaltic and alkali-rich targets have a range of alkali contents consistent with a mixing model with variable proportions of three endmembers: mugearitic, potassic, and basaltic (soil-like). The three compositional endmembers correlate qualitatively with the basalt control line (Figure 20a) and olivine control line (Figure 20b) discussed for the basaltic units above. To reiterate, here we use the term “mugearitic” to refer to compositions that fall slightly above or within the hawaiite-mugearite-benmoreite fields in the total alkali versus silica diagram (Figure 4). The three endmembers are further illustrated in a plot of K/Ti versus Na/Ti, which can be sensitive to alkali feldspar fractionation and/or physical sorting (Figure 20c; e.g., Stanley & Madeisky, 1996). In this plot, the higher total alkalis of the mugearitic rocks results in a positive correlation, whereas the potassic rocks trend to high K/Ti at low Na/Ti. Many of the alkali-rich targets fall between the three identified endmembers and are interpreted to be mixtures of the three endmembers via physical sedimentary processes.

The basaltic and mugearitic endmembers have elemental compositional trends that are similar to ocean island volcanics, such as Tenerife (Canary Islands) and Mauna Kea (Hawai’i), where compositions follow the alkaline differentiation series basalt-hawaiite-mugearite-benmoreite (Figure 4; Schmidt et al., 2014; Stolper et al., 2013). The positive correlation of K/Ti with Na/Ti (Figure 20c) and the ~1:1 correlation of (Ca + Na)/Ti with Al/Ti (Figure 20d) is consistent with plagioclase enrichment in the mugearitic endmember (Stanley & Madeisky, 1996). Postshield volcanics on Mauna Kea exhibit very similar trends in the element ratio indicator plots discussed herein (Figure S12). The elemental characteristics of the basaltic and mugearitic endmembers may be evidence of a common petrogenetic evolution involving high pressure fractional crystallization, as seen in terrestrial postshield volcanics (e.g., Wolfe et al., 1997).

Constraints on the potassic endmember are provided by the drill target Windjana, which has evidence of a magma source separate from the basaltic and mugearitic endmembers. Windjana is not a singular igneous composition; the presence of pigeonite and sanidine together indicates at least two sources because a sanidine-rich protolith would contain augite and not pigeonite (Treiman et al., 2016). Windjana has mineralogical evidence of three sediment sources, which correspond with the three igneous endmembers evident in the APXS results: basalt, a plagioclase-rich source, and potassic trachyte (Treiman et al., 2016). Based primarily on CheMin XRD results, Treiman et al. (2016) concluded that the potassic component of Windjana (sanidine) was sediment derived from a potassic trachyte lava, although potassic metasomatism could not be ruled out.

We suggest that igneous processes and simple physical mixing of sediment with the chemical characteristics of the basaltic, mugearitic, and potassic endmembers can convincingly create most of the compositions found in the Bradbury group. The mineralogy of Windjana, therefore, probably reflects the provenance of these three possible sources. It is thus not necessary to call upon generation of these compositions using physical sorting of sediment derived from a basalt protolith alone (cf. Siebach et al., 2017). On Earth, physical sorting of basaltic sediment does not necessarily result in significant chemical fractionation. For example, the Dyngjúsundur basaltic glacial outwash sand sheet in Iceland has only a small increase in olivine content (apparent in the 8% relative increase in MgO) with fluvial and aeolian transport over a distance of 30 km (Sara, 2017). Similarly, an enrichment in olivine was found at the Lambahraun sandy-lava plain in Iceland over a distance of ~12 km of aeolian transport, but the major elements vary by less than 9% (Mangold et al., 2011). Basaltic fluvial sediment in Iceland exhibits more extensive chemical and mineralogical changes over a longer transport distance (~100 km) due to sorting and chemical alteration (Thorpe et al., 2019). The effects of the fluvial transport in this Icelandic analogue, however, resulted in up to ~20%–40% decreases in Ca and Na (thus a higher CIA value) and a decrease in bulk plagioclase content from ~50 wt% in the parent rock to ~30 wt% in downstream samples (Thorpe et al., 2019). Based on this evidence, it would be unlikely to generate a bulk mugearitic or sanidine-rich potassic composition through sorting processes. For comparison, the Sheepbed member is ~30–60 km from the Peace Valles catchment that may have been a source region. Indeed, the active sands in Gale have been transported more than ~10 km with relatively limited sorting and minimal changes to the original basaltic bulk composition (O'Connell-Cooper et al., 2017 and 2018). Given the terrestrial evidence and the likely conditions in Gale crater, the chemical characteristics of the mugearitic sediment, in particular, indicate that an igneous origin is more parsimonious, and thus more likely, than an origin via mineral sorting of a basalt precursor. Subsequent mixing with the basaltic and potassic endmembers resulted in the range of compositions observed by *Curiosity*.

An important consideration for an igneous endmember model is the elevated concentrations of volatile elements SO₃ (1–8 wt%) and Cl (0.5–1.9 wt%), which are confirmed by drill fines results to be a component of the bedrock to a depth of ~5 cm and are not simply a thin dust coating. The source of S and Cl is uncertain: were they added by aqueous processes after deposition or incorporated as a detrital or airfall dust component? We can say with certainty that they were both mobile in fluids after deposition because Ca-sulfate veins crosscut nearly every unit. Furthermore, the Stephen target, which is an apparent veinlet adjacent to the Windjana potassic basaltic drilled sandstone, is highly enriched in Cl (3.5 wt%). Therefore, the igneous chemical signatures were likely modified, at a minimum, by addition of S and Cl.

5.2. Chemical Evolution of the Sedimentary Units

Considering the evidence presented above, we can reasonably conclude that the sedimentary units of Gale crater contain the geochemical signatures of a basaltic provenance, with mugearitic and potassic sources contributing to most of the Bradbury group and to the Bradbury-like float on lower Mt. Sharp. Chemical evidence of alteration was found throughout the strata, and localized enrichments in veins, concretions, and other features demonstrate in situ mobilization and concentration of elements. Results from CheMin XRD confirm profoundly that, while the bedrock has a petrogenesis that is related to igneous processes based on the presence of the detrital basaltic mineral assemblage of plagioclase and pyroxene with some olivine, oxides, and apatite, other processes are also recorded by the occurrence of typical alteration products: X-ray amorphous materials, phyllosilicates, Ca-sulfates, jarosite, akaganeite, and iron oxides (Rampe

et al., 2020a). Most authors have thus explained the chemistry of Gale crater in terms of volcanic genesis followed by sedimentary processes that include mineral sorting, weathering, and diagenesis (e.g., Bedford et al., 2019; Frydenvang et al., 2017; Hurowitz et al., 2017; Siebach et al., 2017). Below we discuss the chemical evolution of the sedimentary units in Gale crater and the implications for its geologic history.

5.2.1. Sedimentological and Stratigraphic Background

Sedimentological and stratigraphic observations have led to the interpretation that Gale crater contained fluvial, deltaic, and lacustrine environments (Grotzinger et al., 2014, 2015). *Curiosity's* traverse through the sequence of eroded sedimentary rocks (Figure 1) has revealed evidence that the lowermost unit, the Sheepbed mudstone of Yellowknife Bay, was a subaqueous lacustrine deposit (Grotzinger et al., 2014, 2015). The Sheepbed mudstone underlies the conglomerate and massive, cross-stratified, and clinoforn sandstones of the Bradbury group, which was likely deposited in a fluvial environment (Grotzinger et al., 2014, 2015). The Murray formation of the Mount Sharp group is the next sedimentary unit and is proposed to be linked to the Sheepbed mudstone by a similar lacustrine depositional setting (Grotzinger et al., 2015). The Murray formation is primarily laminated mudstone, but thin sandstone units occur (Fedó et al., 2018; Stack et al., 2019). Much of the lithologic variability is found in the Sutton Island member, which is a mix of mudstone, siltstone, and sandstone. Depositional transitions and changes in lacustrine environments (i.e., perennial to episodic) are suggested by the mixed rock types. This is supported by possible desiccation features in the Sutton Island member (N. Stein et al., 2018). The Blunt's Point member, which is recessive relative to the overlying VRR, is a fine-grained, laminated mudstone with common concordant Ca-sulfate veins (Edgar et al., 2020). The Pettegrove Point and Jura members comprise a resistant topographic ridge (VRR) with laminae thicknesses and grain sizes similar to the underlying Murray formation units, also consistent with a lacustrine environment (Edgar et al., 2020). The Stimson formation of the Siccar Point group unconformably overlies the Murray formation, and is interpreted to be lithified sand dune deposits that imply a change in climate from wet to arid (Banham et al., 2018).

5.2.2. Mudstones of the Mt. Sharp and Bradbury Groups

The mudstones of the Sheepbed member and Murray formation are comprised primarily of fine-grained rock that may be genetically linked by a lacustrine depositional environment and share a similar basaltic provenance (although the provenance of the Murray formation is less certain). The chemical evolution of the two units, however, was distinct, as reflected in compositional differences.

5.2.2.1. Sheepbed Member

The similarity of the Sheepbed member to basaltic soil (Figure 7e) suggests that (1) the sediment source was basaltic and (2) the alteration evident in CheMin analyses was largely isochemical (McLennan et al., 2013; Vaniman et al., 2014). McLennan et al. (2013) interpreted the conditions under which the Sheepbed member formed to be cold, arid, and rock dominated, which indicates rapid erosion and deposition. CheMin XRD results led Vaniman et al. (2014) to hypothesize that ~75% less olivine, three times more magnetite, and the ~20 wt% smectite in two Sheepbed member samples, relative to the nearby Rocknest soil sample (Blake et al., 2013), was evidence that basaltic detrital material with a soil-like composition was altered such that most of the olivine was converted to magnetite and smectite. The isochemical nature of this alteration process suggests it was authigenic (McLennan et al., 2013; Vaniman et al., 2014). A minor amount of open system processes may be evident in Mg-rich raised ridges (McGrath; Léveillé et al., 2014) and depleted Mn, which may have been dissolved in fluid and removed from the rock.

The model outlined above for the formation of the Sheepbed mudstone does not account for Zn, which is more than two times higher than soil, and the remarkable Ge enrichment (80 ± 25 ppm; Berger et al., 2017). High concentrations of moderately volatile trace elements invoke enrichment processes (e.g., hydrothermal; see Section 5.2.6) that are at odds with the hypothesis that basaltic sediment was isochemically altered at low temperatures. The trace element signature therefore suggests a more complex history.

5.2.2.2. Murray Formation

Evidence of aqueous processes are apparent in the Murray formation bedrock composition as well as the common diagenetic features. The Murray formation and Sheepbed member mudstones likely have similar basaltic provenance and are hypothesized to represent a common lacustrine depositional setting, with the overlying Murray formation representing younger deposits (e.g., Hurowitz et al., 2017). The two mudstones, however, have distinct compositions. In this section, we explore two models of the aqueous geochemical conditions under which the Murray formation could have been altered. Temperatures attained were likely below $\sim 75^{\circ}\text{C}$, which is the maximum temperature modeled for buried Gale sediment, assuming no external heat source (Borlina et al., 2015) at the likely maximum burial depth of $\sim 2,600$ m (Lewis et al., 2019). The absolute ages of fluid interactions in the Murray formation are partially constrained by K-Ar dating of the drilled sample Mojave 2 (sols 867–888) by the SAM instrument, which determined a bulk age of 2.57 ± 0.39 Ga (Martin et al., 2017). Detrital feldspar formed at 4.07 ± 0.63 Ga, and the observed low temperature K-Ar release indicates that jarosite in the sample crystallized 2.12 ± 0.36 Ga, providing evidence that low pH aqueous processes occurred ~ 1 Ga after deposition (Martin et al., 2017), which likely occurred before 3.3–3.1 Ga (Grant et al., 2014; Grotzinger et al., 2015). Below, we discuss the APXS results in the context of two contrasting models for the chemical evolution of the Murray formation: acid-sulfate alteration and circumneutral chemical weathering.

Acid-Sulfate Alteration

In the Murray formation, element enrichments and depletions relative to soil (Figures 7b and 7c) have several possible chemical fingerprints of low pH alteration: (1) elevated SiO_2 , (2) depleted MnO, MgO, CaO, and (3) enriched K_2O . The elevated SiO_2 and high K_2O , in particular, may be low pH indicators because both elements are typically depleted in basalt by circumneutral, open-system alteration and enriched by acid-sulfate alteration (Figure S13; Nesbitt & Wilson, 1992). This leads us to consider if the acid sulfate alteration interpretation for the fracture haloes (Yen et al., 2017b) can also account for variations observed in the Murray formation bedrock. The presence of jarosite (~ 1 –8 wt%) in 8 of 12 Murray samples (Achilles et al., 2020; Morrison et al., 2018; Rampe et al., 2020b) is also an indicator of low pH fluids because it precipitates at $\text{pH} < 5$ (King & McSween, 2005), and commonly coprecipitates with phyllosilicates and hematite in acidic sedimentary systems (e.g., Baldridge et al., 2009). The geochemical and mineralogical evidence led Rampe et al. (2017) to propose a model for the Pahrump Hills member in which acidic groundwater interacted with the sediment and mobilized Al, Fe, Mn, Ni, and Zn. In this model, the Buckskin high-Si facies was leached of these elements (Figure 7d), and they were translocated downsection and precipitated due to buffering by weathering reactions to higher pH, causing Al, Zn, and Ni enrichment in the underlying Pahrump Hills bedrock. A similar interpretation was proposed for the Vera Rubin ridge based on the mineralogy observed by CheMin: variably warm, acidic, saline fluids interacted with the Murray formation bedrock at a contact with an overlying unit, likely the Siccar Point group before it was eroded (Rampe et al., 2020b). The presence of smectite, red hematite, gray hematite, akaganeite, jarosite, and Ca-sulfate indicate, along with other evidence, that conditions were variable (Rampe et al., 2020b).

The bulk elemental indicators of acidic alteration are also evident in the ~ 320 m of overlying Murray formation strata. The element ratio pattern (Figure 7b) shows that, relative to the basaltic soil, Murray formation bedrock has elevated SiO_2 , the same or greater TiO_2 , FeO, K_2O , and P_2O_5 , and depleted MnO, MgO, and CaO. These chemical trends are similar to terrestrial rocks altered by acid-sulfate processes. For example, Morris et al. (2000) showed that acid-sulfate altered tephra from Mauna Kea, Hawai'i retains SiO_2 and TiO_2 in the altered rock residue. Iron is oxidized and forms secondary Fe-oxides that can be retained in the altered tephra. Sodium and potassium are leached from the rock and precipitate with alunite group sulfates (e.g., jarosite), and phosphate derived from apatite dissolution is retained in the secondary alteration assemblage. Elements removed from the rock are Mn, Mg, and Ca. The result is a bulk composition with same or greater TiO_2 , FeO, K_2O , and P_2O_5 , and depleted MnO, MgO, and CaO, which is similar to the trend observed in the Murray formation bedrock. Elements that were mobilized and removed from the bulk rock are accounted for in the closed Gale crater basin by the Mg- and Ca-sulfates in veins and concretions, and in highly localized Mn-rich features (Berger et al., 2019).

Several characteristics are problematic for the acid sulfate alteration model. Minor amounts of fluorapatite (1–2 wt%) co-exist with jarosite (0–3 wt%; Rampe et al., 2017), but fluorapatite is soluble at low pH (Chairat et al., 2007) and so would be expected to dissolve. This may be evidence that only minor, localized jarosite formed by oxidation of sulfides (Hurowitz et al., 2017). Furthermore, it is difficult to maintain extensive amounts of strongly acidic solutions in the presence of the other observed minerals because acid-base reactions will neutralize the solution (King & McSween, 2005).

Chemical Weathering and SiO₂ Enrichment in Neutral to Alkaline Fluids

Chemical weathering and silica addition via precipitation from neutral to alkaline fluids has been proposed to explain the Murray characteristics, particularly the elevated SiO₂ (Figure 7; Frydenvang et al., 2017; Hurowitz et al., 2017). If circumneutral (i.e., pH between ~6 and 8) chemical weathering occurred at Gale crater before, during, and after transport of the lake sediment, it is likely that the fluids which interacted with the sediment contained dissolved silica (Hurowitz et al., 2017). The addition of a silica cement (e.g., Siever, 1957) would result in higher SiO₂ in the bulk rock. This model requires that the silica-depleted, weathered residue was not re-incorporated into the sediment, because that would result in ~zero net change in the bulk composition. According to Hurowitz et al. (2017), the SiO₂ enrichment in the Pahrump Hills member, typified by the drill target Buckskin, can be explained by the simple addition of pure SiO₂ and CaSO₄ to a bedrock composition representative of average bedrock for that unit (Telegraph Peak drill sample).

A simple silica addition model is inconsistent with APXS observations. Hurowitz et al. (2017) predicts that the composition of the high-SiO₂ Buckskin high-Si facies is modeled by a mixture of three endmembers: pure SiO₂, CaSO₄, and Pahrump Hills bedrock (represented by the Telegraph Peak target). We tested this model to determine how accurately it predicts the Buckskin composition. A linear, least-squares deconvolution was used to estimate the fractions of each of the three endmembers proposed for Buckskin (see Text S1). According to the deconvolution, pure SiO₂, CaSO₄, and Telegraph Peak comprise 55%, 8%, and 32% of Buckskin, respectively. This result is comparable to Hurowitz et al. (2017), who estimated Telegraph Peak was ~30% of Buckskin. However, when the three endmember components are combined to model Buckskin, significant differences are apparent (Figure 21a). Most notable are TiO₂, K₂O, and P₂O₅, which are respectively ~3X, ~2X, and ~2X higher in the actual Buckskin than in the model. A fingerprint of acid sulfate alteration, as discussed above in terrestrial materials (Morris et al., 2000), is the retention of these three elements in the altered residue and secondary phases. These characteristics should therefore should not be dismissed in interpretations of the Murray formation chemical evolution. In summary, the silica + CaSO₄ addition model may be oversimplified; the geochemical characteristics of the bedrock are, overall, not consistent with the model.

The circumneutral weathering model may also be inconsistent with K₂O and Na₂O observations. If the protolith was chemically weathered by a circumneutral fluid that released silica into solution, then we would expect concomitant mobilization of the more-soluble ions K⁺ and Na⁺ (Nesbitt & Wilson, 1992). Both K⁺ and Na⁺ are conservative elements and would likely accumulate in a brine and precipitate in evaporitic deposits, not in a cement with silica (Garrels & Christ, 1965). This prediction is not consistent with the K₂O enrichment and soil-like Na₂O concentrations in the Murray formation bedrock (Figures 7b, 7c, and 7d).

Chemical weathering of basalt in a circumneutral, open system can be quantified with the chemical index of alteration (CIA; Nesbitt & Young, 1982). The CIA is calculated using molecular proportions as:

$$CIA = \left[\text{Al}_2\text{O}_3 / (\text{Al}_2\text{O}_3 + \text{CaO} + \text{Na}_2\text{O} + \text{K}_2\text{O}) \right] \times 100 \quad (2)$$

Higher CIA values, relative to the unaltered protolith, indicate chemical weathering because Al usually has low solubility at circumneutral pH and is retained in weathered residue, whereas Ca, Na, and K are more soluble and are more likely to be removed from the system via weathering (Nesbitt & Young, 1982). We find that the CIA is not a useful alteration index for APXS results in Gale crater for the following reasons:

1. The CIA does not consider Mg, which has been demonstrated as a sensitive indicator of chemical weathering on Mars (Figure 8; e.g., Ming et al., 2006) in part because olivine is likely the most susceptible min-

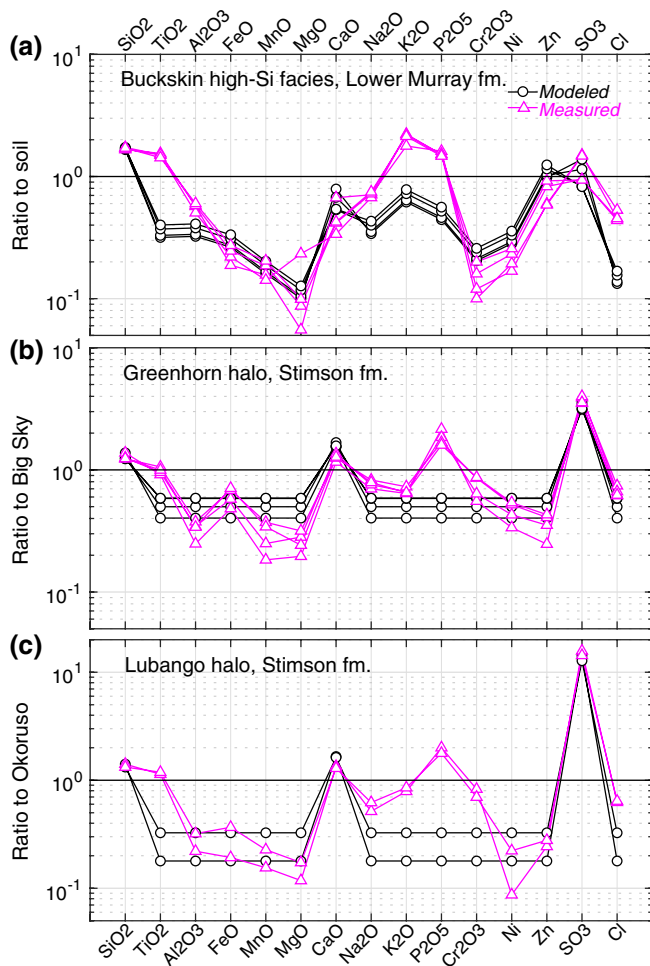


Figure 21. Tests of simple SiO₂ addition models (see Text S1). (a) Measured Buckskin high-silica facies normalized to soil is compared to the modeled composition derived from SiO₂ and Ca-sulfate addition as proposed by Hurowitz et al. (2017). (b) Measured Greenhorn normalized to the less altered parent Big Sky and compared to the modeled composition of simple pure SiO₂ and Ca-sulfate added to a Big Sky composition. (c) Lubango normalized to the less altered parent Okoruso and compared to a modeled Okoruso composition with pure SiO₂ and Ca-sulfate added. Note that the model does not fit well with the observed Ti, K, and P concentrations.

elements, likely after lithification. The timing of the formation of Stephen is not well-constrained because the fin-shaped feature protrudes from the bedrock and does not preserve clear cross-cutting relationships. In addition, aqueous activity was possible >1 Gy after the bulk of the sediments were deposited because localized Aeolis Palus alluvial deposits dated at <2 Ga could have introduced fluids into the system (Grant & Wilson, 2019). Nevertheless, Stephen demonstrates aqueous activity in the Bradbury group sandstone that concentrated fluid-mobile elements.

5.2.4. Stimson Formation Sandstone

The Stimson formation bedrock has a composition consistent with basaltic soil and sand that has experienced limited, largely isochemical alteration of basaltic material (section 4.3.4.3). Olivine is below the 1–2 wt% detection limit of CheMin in the Big Sky and Okoruso drill targets, and the 10–11 wt% magnetite in the samples, which probably comprises the cementing agent, could be a secondary diagenetic product of

eral to incipient low temperature alteration in martian sediments (Vaniman et al., 2014; Yen et al., 2017b), which is consistent with terrestrial materials (e.g., Nesbitt & Wilson, 1992).

2. The CIA is only applicable if the secondary Al-, Ca-, Na-, and K-bearing salts can be subtracted from the chemical analysis, which is a problematic correction for Gale crater targets. In particular, Ca-sulfate is ubiquitous (Section 4.4.2), but the amount of Ca-sulfate is poorly constrained in targets that have not been analyzed by CheMin. Therefore, Ca-sulfate cannot be subtracted from most targets without an unacceptable amount of uncertainty. Furthermore, much of the S in the bulk sample is likely associated with the amorphous component (Table S1; McAdam et al., 2014; Morrison et al., 2018). In this amorphous material, S may be coupled with Mg and/or Fe in amorphous sulfates. Thus, the amount of sulfate salts cannot be unambiguously subtracted from APXS analyses because S is coupled with Ca, Mg, and Fe, all of which are major elements associated with primary igneous phases.
3. Evidence of Al mobility is found in the Pahrump Hills member (Rampe et al., 2017) and in the Stimson formation fracture haloes (Yen et al., 2017b). If Al is mobile, then it is not suitable to use as the immobile element against which to compare Ca, K, and Na mobility in the CIA.

5.2.3. Bradbury Group Sandstone, Conglomerate, and Float

The geochemical characteristics of the Bradbury group (excluding the Sheepbed member mudstone) are generally consistent with a mixture of unaltered and/or isochemically altered igneous endmembers. The physical mixing model proposed in Section 5.1.2 reasonably accounts for most of the sandstone, conglomerate, and float compositions by way of mixtures of the basaltic, mugearitic, and potassic basaltic endmembers. This is consistent with the results from the only drill target in Bradbury units above the Sheepbed member, Windjana, which is a mixture of igneous components that were likely cemented by magnetite and ferrihydrite (Treiman et al., 2016). Iron-rich cement is also apparent in several Bradbury targets with higher FeO that deviates from igneous mixing models (e.g., Oscar, Et Then; Figure 8a; Schmidt et al., 2014). The APXS observations suggest that the Bradbury materials were transported, deposited, and lithified under conditions with limited chemical weathering.

An important consideration is the veinlet Stephen next to the drill target Windjana. Stephen is highly enriched in Zn, Mn, and Cl (Sections 4.3.2 and 4.4.3), which is strong evidence of in situ mobilization of those elements,

olivine alteration (Yen et al., 2017b). The sedimentological interpretation of the Stimson formation is that it formed in an arid aeolian system, and stratigraphic relationships suggest the unconformity between the underlying Murray formation and the Stimson formation represents a period of erosion and time (Banham et al., 2018). The geochemical differences between the two formations also indicate distinct geochemical evolution of the bedrock. However, features indicating similar aqueous activity are common to both formations: (1) cross-cutting sulfate veins, (2) cross-cutting fracture-associated haloes, and (3) Mg-sulfate nodules near the unconformity (e.g., Sperrgebiet). Therefore, the chemical evolution of the two formations is not entirely decoupled.

5.2.5. Fracture Halo Formation

Fracture-associated haloes (Section 4.4.1) cross-cut the Murray formation, Stimson formation (Yen et al., 2017b), and the Bradbury group (Gabriel et al., 2019), postdating the lithification of those units. Two of the models proposed for the fracture haloes have contrasting hypotheses on the pH of the fluids that interacted with the rock. The chemical and mineralogical characteristics of the fracture haloes led Yen et al. (2017b) to conclude that initially acidic fluids leached Al, Fe, Mn, Mg, Ni, Zn, \pm Na, and \pm K, causing the passive enrichment of silica and TiO₂ in the residue. The depletion of Al is notable because it typically has low solubility in circumneutral fluids and remains in altered residue; mobility of Al is an indicator for low pH. Excess Si, relative to Ti, indicates later alkaline fluids deposited additional silica, thus silica enrichment was both passive and active. Frydenvang et al. (2017) proposed a model involving only active enrichment of silica: groundwater interacted with the underlying Si-rich Buckskin facies and carried dissolved silica to the fractures where it was precipitated via decrease in temperature and/or alkalinity. The model suggests that the haloes are parent bedrock diluted with Ca-sulfate and pure silica. This three endmember model is the same as proposed for the Murray formation (Hurowitz et al., 2017), and we tested it with the same linear, least-squares deconvolution discussed in Section 5.2.2.2 (see also Text S1). The model results have a significant mismatch of the modeled versus measured concentrations of Ti, Na, K, P and \pm Cr (Figures 21b and 21c). The silica + CaSO₄ addition model deviates from the observed composition in a similar manner for both the fracture haloes and the Murray formation (Figure 21a). We conclude that silica + CaSO₄ addition is not a compelling model for the formation of the fracture haloes and that the acid-sulfate-dominated alteration model of Yen et al. (2017b) is more plausible.

5.2.6. Hydrothermal Indicators

In the Murray formation, the trace elements Zn and Ge are enriched ($1,060 \pm 460$ ppm and 110 ± 20 ppm, respectively) tens to hundreds of times greater than predicted from martian meteorites and crustal formation models (Berger et al., 2017). The enrichment is relatively uniform, except in the Buckskin high-Si facies where Zn and Ge are lower (respectively 170 ± 100 and 50 ± 20 ppm; Figure 7). Because the two elements are commonly coupled in hydrothermal fluids, their enrichment indicates a hydrothermal signature in the Murray formation. The Murray units do not contain hydrothermal mineral assemblages expected with a basaltic protolith (e.g., serpentine–chlorite–[amphibole–talc–magnetite] \pm garnet \pm quartz) (Schwenzer & Kring, 2009). However, the Murray formation does contain assemblages of minerals that can be associated with hydrothermal processes: hematite, magnetite, Si-rich X-ray amorphous material, phyllosilicates, and, most importantly because it is the only unambiguous high temperature phase, tridymite (e.g., Hynek et al., 2013). These observations led Berger et al. (2017) to conclude that hydrothermal deposits exist (ed) in the Gale source region and were dispersed with siliciclastic material during transport and deposition. Alternatively, the possible localized occurrence of high-temperature silica mineralization ($\sim 870^\circ\text{C}$; e.g., Swamy et al., 1994) has led to speculation that hydrothermal fluids interacted with the Murray formation bedrock after deposition (Yen et al., 2017a). The presence of a possible hydrothermal deposit is a key finding because it expands the number of habitable environments that could have existed in Gale.

Enriched Zn and Ge also occur at concentrations similar to the Murray formation in the Sheepbed member and alkali-rich units (with the exception of the mugearitic endmembers), suggesting that this trace element signature is common in Gale (Berger et al., 2017). In these units, like the Murray formation, hydrothermal alteration mineral assemblages expected for a basaltic protolith were not unambiguously identified.

6. Conclusions

Curiosity's APXS has acquired a dataset of >700 measurements over a >20 km traverse, determining the elemental composition of geologic materials on the martian surface. The APXS has made a number of other contributions, including triage for drill site selection, providing constraints on crystal chemistry for CheMin (e.g., Morrison et al., 2018) and sulfur and chlorine speciation for SAM (e.g., Sutter et al., 2018), and enabling K-Ar dating with SAM results (Farley et al., 2014; Martin et al., 2017). The APXS has also made it possible to directly compare the elemental composition of martian surface materials at the Viking, Pathfinder, MER-A, and MER-B landing sites, building on a global compositional dataset.

How does the geochemical data from the APXS contribute to an integrated model of the provenance and chemical evolution of Gale crater? APXS-based observations from Gale crater have led to a number of conclusions, including:

1. Unconsolidated fine material, or sand, soil, and dust, has a basaltic composition that is effectively the same as basaltic soil found at the MER and Pathfinder sites. This establishes an average basaltic composition for the martian crust.
2. The Bradbury group has a wide range of compositions, indicating the source region is a diverse igneous complex containing basalts, high-alkali rocks with igneous hawaiiite-mugearite-benmoreite characteristics, and potassic basalts.
3. The preserved igneous bulk elemental compositions of the Bradbury group sandstone, conglomerate, and float indicate deposition in an arid climate and rapid erosion, with minimal open-system chemical weathering.
4. The Sheepbed member mudstone and Murray formation mudstone both have evidence of a basaltic provenance; however, their geochemical characteristics are different. The Sheepbed member largely preserves the bulk chemical composition of basalt, indicating limited, closed-system alteration. In contrast, the Murray formation has indications of pervasive open-system alteration in the bedrock. If the Sheepbed member mudstone and Murray formation mudstone are linked by a similar lacustrine depositional paleoenvironment, their chemical evolution pathways were distinct.
5. The Stimson formation is an aeolian sandstone with a basaltic composition similar to sand and soil. The basaltic composition is largely preserved, indicating deposition in an arid environment and limited, closed-system alteration during lithification.
6. Diverse diagenetic features are common on *Curiosity's* traverse, and include nodules, veins, concretions, and patchy crusts with enrichments in Mn, Fe, Zn, Ni, P, Cl, and S. These enrichments indicate widespread element mobility in fluids.
7. Ca-sulfate veins crosscut every sedimentary unit, demonstrating fluid activity after lithification of the sediment.
8. Extensive open-system alteration occurred in localized, fracture-associated haloes, thus fluid activity occurred after lithification of the Murray formation and unconformably overlying Stimson formation.

Data Availability Statement

All APXS spectra and reductions are available at the planetary data system, https://pds-geosciences.wustl.edu/msl/msl-m-apxs-4_5-rdr-v1/mslapx_1xxx/ and the MSL APXS RDR dataset has the DOI:10.17189/1518757. The Supporting Information, including the two .csv files containing Data Sets S1 and S2, are also in Berger (2020) PDS GeosciencesNode https://pds-geosciences.wustl.edu/msl/urn-nasa-pds-msl_apxs_supplement_sols_0_2301/.

Acknowledgements

We are indebted to NASA-JPL, the Canadian Space Agency, and Australian Research Council (DP150104604) for supporting our work and the MSL mission. A portion of this study was conducted at the Jet Propulsion Laboratory, California Institute of Technology under a contract with the National Aeronautics and Space Administration.

References

- Achilles, C. N., Rampe, E. B., Downs, R. T., Bristow, T. F., Ming, D. W., Morris, R. V., et al. (2020). Evidence for multiple diagenetic episodes in ancient fluvial-lacustrine sedimentary rocks in Gale crater, Mars. *Journal of Geophysical Research: Planets*, 125(8), e2019JE006295. <https://doi.org/10.1029/2019JE006295>
- Agee, C. B., Wilson, N. V., McCubbin, F. M., Ziegler, K., Polyak, V. J., Sharp, Z. D., et al. (2013). Unique meteorite from early Amazonian Mars: Water-rich basaltic breccia Northwest Africa 7034. *Science*, 339(6121), 780–785. <https://doi.org/10.1126/science.1228858>
- Anderson, R. C., Jandura, L., Okon, A. B., Sunshine, D., Roumeliotis, C., Beegle, L. W., et al. (2012). Collecting samples in Gale crater, Mars; an overview of the Mars science laboratory sample acquisition, sample processing and handling system. *Space Science Reviews*, 170(1–4), 57–75. <https://doi.org/10.1007/s11214-012-9898-9>

- Anderson, R. B., Morris, R. V., Clegg, S. M., Bell, J. F. III, Wiens, R. C., Humphries, S. D., et al. (2011). The influence of multivariate analysis methods and target grain size on the accuracy of remote quantitative chemical analysis of rocks using laser induced breakdown spectroscopy. *Icarus*, 215(2), 608–627. <https://doi.org/10.1016/j.icarus.2011.07.034>.
- Baldrige, A. M., Hook, S. J., Crowley, J. K., Marion, G. M., Kargel, J. S., Michalski, J. L., et al. (2009). Contemporaneous deposition of phyllosilicates and sulfates: Using Australian acidic saline lake deposits to describe geochemical variability on Mars. *Geophysical Research Letters*, 36(19), L19201. <https://doi.org/10.1029/2009GL040069>
- Banham, S. G., Gupta, S., Rubin, D. M., Watkins, J. A., Sumner, D. Y., Edgett, K. S., et al. (2018). Ancient Martian Aeolian processes and palaeomorphology reconstructed from the Stimson formation on the lower slope of Aeolis Mons, Gale crater, Mars. *Sedimentology*, 65(4), 993–1042. <https://doi.org/10.1111/sed.12469>
- Barnes, S. J., Hill, R. E. T., Perring, C. S., & Dowling, S. E. (2004). Lithochemical exploration for komatiite-associated Ni-sulfide deposits: Strategies and limitations. *Mineralogy and Petrology*, 82(3), 259–293. <https://doi.org/10.1007/s00710-004-0051-7>
- Bedford, C. C., Bridges, J. C., Schwenzer, S. P., Wiens, R. C., Rampe, E. B., Frydenvang, J., & Gasda, P. J. (2019). Alteration trends and geochemical source region characteristics preserved in the fluviolacustrine sedimentary record of Gale crater, Mars. *Geochimica et Cosmochimica Acta*, 246, 234–266. <https://doi.org/10.1016/j.gca.2018.11.031>
- Bell, J. F., Malin, M. C., Caplinger, M. A., Ravine, M. A., Godber, A. S., Jungers, M. C., et al. (2012). *Mastcam multispectral imaging on the Mars science laboratory rover: Wavelength coverage and imaging strategies at the Gale crater field site*. In the 43rd Lunar and Planetary Science Conference, Abstract 2541.
- Berger, J. A. (2020). *Overview of MSL APXS targets from sol 0 to 2301*. NASA Planetary Data System. <https://doi.org/10.17189/1519050>
- Berger, J. A., King, P. L., Gellert, R., Clark, B. C., O'Connell-Cooper, C. D., Thompson, L. M., et al. (2019). *Manganese enrichment pathways relevant to Gale crater, Mars: Evaporative concentration and chlorine-induced precipitation*. In the 50th Lunar and Planetary Science Conference, Abstract 2487.
- Berger, J. A., Schmidt, M. E., Campbell, J. L., Flannigan, E. L., Gellert, R., Ming, W., & Morris, R. V. (2020). Particle Induced X-ray Emission spectrometry (PIXE) of Hawaiian volcanics: An analogue study to evaluate the APXS field analysis of geologic materials on Mars. *Icarus*, 345, 113708. <https://doi.org/10.1016/j.icarus.2020.113708>
- Berger, J. A., Schmidt, M. E., Gellert, R., Boyd, N. I., Desouza, E. D., Flemming, R. L., et al. (2017). Zinc and germanium in the sedimentary rocks of Gale Crater on Mars indicate hydrothermal enrichment followed by diagenetic fractionation. *Journal of Geophysical Research: Planets*, 122(8), 1747–1772. <https://doi.org/10.1002/2017JE005290>
- Berger, J. A., Schmidt, M. E., Gellert, R., Campbell, J. L., King, P. L., Flemming, R. L., et al. (2016). A global Mars dust composition refined by the alpha-particle X-ray spectrometer in Gale crater. *Geophysical Research Letters*, 43(1), 67–75. <https://doi.org/10.1002/2015GL066675>
- Bishop, J. L., Murchie, S. L., Pieters, C. M., & Zent, A. P. (2002). A model for formation of dust, soil, and rock coatings on Mars: Physical and chemical processes on the Martian surface. *Journal of Geophysical Research*, 107(5097), 17. <https://doi.org/10.1029/2001JE001581>
- Blake, D. F., Morris, R. V., Kocurek, G., Morrison, S. M., Downs, R. T., Bish, D., et al. (2013). Curiosity at Gale crater, Mars: Characterization and analysis of the rocknest sand shadow. *Science*, 341(6153), 1239505. <https://doi.org/10.1126/science.1239505>
- Blake, D. F., Vaniman, D., Achilles, C., Anderson, R., Bish, D., Bristow, T., et al. (2012). Characterization and calibration of the CheMin mineralogical instrument on Mars science laboratory. *Space Science Reviews*, 170(1–4), 341–399. <https://doi.org/10.1007/s11214-012-9905-1>
- Borlina, C. S., Ehlmann, B. L., & Kite, E. S. (2015). Modeling the thermal and physical evolution of Mount Sharp's sedimentary rocks, Gale Crater, Mars: Implications for diagenesis on the MSL Curiosity rover traverse. *Journal of Geophysical Research: Planets*, 120(8), 2015JE004799. <https://doi.org/10.1002/2015JE004799>
- Bristow, T. F., Rampe, E. B., Achilles, C. N., Blake, D. F., Chipera, S. J., Craig, P., et al. (2018). Clay mineral diversity and abundance in sedimentary rocks of Gale crater, Mars. *Science Advances*, 4(6), eaar3330. <https://doi.org/10.1126/sciadv.aar3330>
- Brückner, J., Dreibus, G., Gellert, R., Squyres, S. W., Wänke, H., Yen, A., & Zipfel, J. (2008). Mars Exploration Rovers: Chemical composition by the APXS. In J. F. Bell III (Ed.), *The martian surface*. Vol. 1 (pp. 58–101). New York, NY: Cambridge University Press.
- Campbell, J. L., King, P. L., Burkemper, L., Berger, J. A., Gellert, R., Boyd, N. I., et al. (2014). The Mars Science Laboratory APXS calibration target: Comparison of Martian measurements with the terrestrial calibration. *Nuclear Instruments and Methods in Physics Research B*, 323, 49–58. <https://doi.org/10.1016/j.nimb.2014.01.011>
- Campbell, J. L., Perrett, G. M., Gellert, R., Andruschenko, S. M., Boyd, N. I., Maxwell, J. A., et al. (2012). Calibration of the Mars science laboratory Alpha Particle X-ray Spectrometer. *Space Science Reviews*, 170(1–4), 319–340. <https://doi.org/10.1007/s11214-012-9873-5>
- Chairat, C., Schott, J., Oelkers, E. H., Lartigue, J.-E., & Harouiya, N. (2007). Kinetics and mechanism of natural fluorapatite dissolution at 25°C and pH from 3 to 12. *Geochimica et Cosmochimica Acta*, 71(24), 5901–5912. <https://doi.org/10.1016/j.gca.2007.08.031>
- Dreibus, G., & Wanke, H. (1985). Mars, a volatile-rich planet. *Meteoritics*, 20, 367–381.
- Edgar, L. A., Fedo Christopher, M., Gupta, S., Banham Steven, Fraeman Abigail, A., Grotzinger John, P., et al. (2020). A lacustrine paleoenvironment recorded at Vera Rubin ridge, Gale crater: Overview of the sedimentology and stratigraphy observed by the Mars Science Laboratory Curiosity rover. *Earth and Space Science Open Archive*, 125(3). <https://doi.org/10.1002/essoar.10501350.1>
- Edgett, K. S., Yingst, R. A., & McBride, M. J. (2015). *Curiosity's Mars Hand Lens Imager (MAHLI) Mars science laboratory principal investigator's Notebook: Sols 90–179*. MSL MAHLI Technical Report 0003, Version. Retrieved from [http://www.researchgate.net/profile/Ken_Edgett/publication/279179730_Curiositys_Mars_Hand_Lens_Imager_\(MAHLI\)_Mars_Science_Laboratory_\(MSL\)_Principal_Investigators_Notebook_Sols_90179/links/558c524508aee43bf6ae2b0e.pdf](http://www.researchgate.net/profile/Ken_Edgett/publication/279179730_Curiositys_Mars_Hand_Lens_Imager_(MAHLI)_Mars_Science_Laboratory_(MSL)_Principal_Investigators_Notebook_Sols_90179/links/558c524508aee43bf6ae2b0e.pdf)
- Edgett, K. S., Yingst, R. A., Ravine, M. A., Caplinger, M. A., Maki, J. N., Ghaemi, F. T., et al. (2012). Curiosity's Mars Hand Lens Imager (MAHLI) investigation. *Space Science Reviews*, 170(1–4), 259–317. <https://doi.org/10.1007/s11214-012-9910-4>
- Farley, K. A., Malespin, C., Mahaffy, P., Grotzinger, J. P., Vasconcelos, P. M., Milliken, R. E., et al. (2014). In situ radiometric and exposure age dating of the martian surface. *Science*, 343(6169), 1247166. <https://doi.org/10.1126/science.1247166>
- Fedo, C. M., Grotzinger, J. P., Gupta, S., Fraeman, A., Edgar, L., Edgett, K., et al. (2018). *Sedimentology and stratigraphy of the Murray formation, Gale crater, Mars*. In the 49th Lunar and Planetary Science Conference, Abstract 2078.
- Filiberto, J., McCubbin, F. M., & Taylor, G. J. (2019). Chapter 2 - volatiles in martian magmas and the interior: Inputs of volatiles into the crust and atmosphere. In J. Filiberto, & S. P. Schwenzer (Eds.), *Volatiles in the martian crust* (pp. 13–33). New York, NY: Elsevier <https://doi.org/10.1016/B978-0-12-804191-8.00002-7>
- Fox, V. K., Bennett, K. A., Bristow, T., Ehlmann, B. L., House, C., Fairén, A. G., et al. (2019). *Exploring the Clay-Bearing Unit with the Curiosity Rover*. In the 50th Lunar and Planetary Science Conference, Abstract 2826.
- Franz, H. B., King, P. L., & Gaillard, F. (2019). Chapter 6 - Sulfur on Mars from the atmosphere to the core. In J. Filiberto, & S. P. Schwenzer (Eds.), *Volatiles in the martian crust* (pp. 119–183). New York, NY: Elsevier. <https://doi.org/10.1016/B978-0-12-804191-8.00006-4>

- Frydenvang, J., Gasda, P. J., Hurowitz, J. A., Grotzinger, J. P., Wiens, R. C., Newsom, H. E., et al. (2017). Diagenetic silica enrichment and late-stage groundwater activity in Gale crater, Mars. *Geophysical Research Letters*, *44*(10). 2017GL073323. <https://doi.org/10.1002/2017GL073323>
- Gabriel, T. S. J., Hardgrove, C., Achilles, C., Rampe, E. B., Czarnecki, S., Rapin, W., et al. (2019). *Pervasive water-rich, fracture-associated alteration halos in Gale crater, Mars*. AGU Fall Meeting Abstracts. Retrieved from <http://adsabs.harvard.edu/abs/2019AGUFM.P43B.08G>
- Garrels, R. M., & Christ, C. L. (1965). *Minerals, Solutions, and Equilibria*, New York: Harper & Row.
- Garrels, R. M., & MacKenzie, F. T. (1967). Origin of the chemical compositions of some springs and lakes. In *Equilibrium concepts in natural water systems*, Vol. 67. (pp. 222–242). American Chemical Society. <https://doi.org/10.1021/ba-1967-0067.ch010>
- Gellert, R. (2012). *Mars science laboratory alpha particle X-ray spectrometer EDR data V1.0 MSL-M-APXS-2-EDR-V1.0*. NASA Planetary Data System.
- Gellert, R., Campbell, J. L., King, P. L., Leshin, L. A., Lugmair, G. W., Spray, J. G., et al. (2009). The alpha-particle-X-ray-spectrometer (APXS) for the Mars science laboratory (MSL) rover mission. *Lunar Planet Science XL* (p. Abstract 2364).
- Gellert, R., & Clark, B. C. (2015). Compositional measurements of rocks and soils on NASA's Mars rovers with the alpha-particle X-ray spectrometer (APXS). *Elements*, *11*(1), 39–44. <https://doi.org/10.2113/gselements.11.1.39>
- Gellert R., Rieder R., Brückner J., Clark B. C., Dreibus G., Klingelhöfer G., et al. (2006). Alpha Particle X-ray Spectrometer (APXS): Results from Gusev Crater and calibration report. *Journal of Geophysical Research*, *111*, E02S05. <https://doi.org/10.1029/2005JE002555>
- Goetz, W., Bertelsen, P., Binau, C. S., Gunnlaugsson, H. P., Hviid, S. F., Kinch, K. M., et al. (2005). Indication of drier periods on Mars from the chemistry and mineralogy of atmospheric dust. *Nature*, *436*(7047), 62–65. <https://doi.org/10.1038/nature03807>
- Grant, J. A., & Wilson, S. A. (2019). Evidence for late alluvial activity in Gale crater, Mars. *Geophysical Research Letters*, *46*(13), 7287–7294. <https://doi.org/10.1029/2019GL083444>
- Grant, J. A., Wilson, S. A., Mangold, N., Calef, F., & Grotzinger, J. P. (2014). The timing of alluvial activity in Gale crater, Mars. *Geophysical Research Letters*, *41*(4), 1142–1149. <https://doi.org/10.1002/2013GL058909>
- Grotzinger, J. P., Gupta, S., Malin, M. C., Rubin, D. M., Schieber, J., Siebach, K., et al. (2015). Deposition, exhumation, and paleoclimate of an ancient lake deposit, Gale crater, Mars. *Science*, *350*(6257), aac7575. <https://doi.org/10.1126/science.aac7575>
- Grotzinger, J. P., Sumner, D. Y., Kah, L. C., Stack, K., Gupta, S., Edgar, L., et al. (2014). A habitable fluvio-lacustrine environment at Yellowknife Bay, Gale crater, Mars. *Science*, *343*(6169), 1242777. <https://doi.org/10.1126/science.1242777>
- Haskin, L. A., Wang, A., Jolliff, B. L., McSween, H. Y., Clark, B. C., Des Marais, D. J., et al. (2005). Water alteration of rocks and soils on Mars at the Spirit rover site in Gusev crater. *Nature*, *436*(7047), 66–69. <https://doi.org/10.1038/nature03640>
- Hurowitz, J. A., Grotzinger, J. P., Fischer, W. W., McLennan, S. M., Milliken, R. E., Stein, N., et al. (2017). Redox stratification of an ancient lake in Gale crater, Mars. *Science*, *356*(6341), eaah6849. <https://doi.org/10.1126/science.aah6849>
- Hynek, B. M., McCollom, T. M., Marcucci, E. C., Brugman, K., & Rogers, K. L. (2013). Assessment of environmental controls on acid-sulfate alteration at active volcanoes in Nicaragua: Applications to relic hydrothermal systems on Mars. *Journal of Geophysical Research: Planets*, *118*(10), 2083–2104. <https://doi.org/10.1002/jgre.20140>
- King, P. L., & McSween, H. Y. (2005). Effects of H₂O, pH, and oxidation state on the stability of Fe minerals on Mars. *Journal of Geophysical Research*, *110*, 15. <https://doi.org/10.1029/2005JE002482>
- Kounaves, S. P., Chaniotakis, N. A., Chevri er, V. F., Carrier, B. L., Folds, K. E., Hansen, V. M., et al. (2014). Identification of the perchlorate parent salts at the Phoenix Mars landing site and possible implications. *Icarus*, *232*, 226–231. <https://doi.org/10.1016/j.icarus.2014.01.016>
- Kronyak, R. E., Kah, L. C., Edgett, K. S., VanBommel, S. J., Thompson, L. M., Wiens, R. C., et al. (2019). Mineral-filled fractures as indicators of multigenerational fluid flow in the Pahrump Hills member of the Murray formation, Gale crater, Mars. *Earth and Space Science*, *6*(2), 238–265. <https://doi.org/10.1029/2018EA000482>
- Lanza, N. L., Wiens, R. C., Arvidson, R. E., Clark, B. C., Fischer, W. W., Gellert, R., et al. (2016). Oxidation of manganese in an ancient aquifer, Kimberley formation, Gale crater, Mars. *Geophysical Research Letters*, *43*(14), 2016GL069109. <https://doi.org/10.1002/2016GL069109>
- Lasue, J., Clegg, S. M., Forni, O., Cousin, A., Wiens, R. C., Lanza, N., et al. (2016). Observation of >5 wt% zinc at the Kimberley outcrop, Gale crater, Mars. *Journal of Geophysical Research: Planets*, *121*(3), 338–352. <https://doi.org/10.1002/2015JE004946>
- Lasue, J., Cousin, A., Meslin, P.-Y., Mangold, N., Wiens, R. C., Berger, G., et al. (2018). Martian eolian dust probed by ChemCam. *Geophysical Research Letters*, *45*(20), 10968–10977. <https://doi.org/10.1029/2018GL079210>
- Le Deit, L. L., Hauber, E., Fueten, F., Pondrelli, M., Rossi, A. P., & Jaumann, R. (2013). Sequence of infilling events in Gale Crater, Mars: Results from morphology, stratigraphy, and mineralogy. *Journal of Geophysical Research: Planets*, *118*(12), 2012JE004322. <https://doi.org/10.1002/2012JE004322>
- Le Maitre, R. W., Streckeisen, A., Zanettin, B., Le Bas, M. J., Bonin, B., & Bateman, P. (2002). *Igneous rocks: A classification and glossary of terms: Recommendations of the international union of geological sciences subcommission on the systematics of igneous rocks*, Cambridge, UK: Cambridge University Press.
- L evell e, R. J., Bridges, J., Wiens, R. C., Mangold, N., Cousin, A., Lanza, N., et al. (2014). Chemistry of fracture-filling raised ridges in Yellowknife Bay, Gale Crater: Window into past aqueous activity and habitability on Mars. *Journal of Geophysical Research: Planets*, *119*(11), 2398–2415. <https://doi.org/10.1002/2014JE004620>
- Lewis, K. W., Peters, S., Gonter, K., Morrison, S., Schmerr, N., Vasavada, A. R., & Gabriel, T. (2019). A surface gravity traverse on Mars indicates low bedrock density at Gale crater. *Science*, *363*(6426), 535–537. <https://doi.org/10.1126/science.aat0738>
- Lodders, K., & Fegley, B. (1997). An oxygen isotope model for the composition of Mars. *Icarus*, *126*(2), 373–394. <https://doi.org/10.1006/icar.1996.5653>
- Mahaffy, P., Webster, C., Cabane, M., Conrad, P., Coll, P., Atreya, S., et al. (2012). The sample analysis at Mars investigation and instrument suite. *Space Science Reviews*, *170*(1–4), 401–478. <https://doi.org/10.1007/s11214-012-9879-z>
- Maki, J., Thiessen, D., Pourangi, A., Kobzeff, P., Litwin, T., Scherr, L., et al. (2012). The Mars science laboratory engineering cameras. *Space Science Reviews*, *170*(1–4), 77–93. <https://doi.org/10.1007/s11214-012-9882-4>
- Mangold, N., Baratoux, D., Arnalds, O., Bardintzeff, J.-M., Platevoet, B., Gr egoire, M., & Pinet, P. (2011). Segregation of olivine grains in volcanic sands in Iceland and implications for Mars. *Earth and Planetary Science Letters*, *310*(3), 233–243. <https://doi.org/10.1016/j.epsl.2011.07.025>
- Mangold, N., Forni, O., Dromart, G., Stack, K., Wiens, R. C., Gasnault, O., et al. (2015). Chemical variations in Yellowknife Bay formation sedimentary rocks analyzed by ChemCam on board the Curiosity rover on Mars. *Journal of Geophysical Research: Planets*, *120*(3), 2014JE004681. <https://doi.org/10.1002/2014JE004681>
- Mangold, N., Schmidt, M. E., Fisk, M. R., Forni, O., McLennan, S. M., Ming, D. W., et al. (2017). Classification scheme for sedimentary and igneous rocks in Gale crater, Mars. *Icarus*, *284*, 1–17. <https://doi.org/10.1016/j.icarus.2016.11.005>

- Marion, G. M., Catling, D. C., Zahnle, K. J., & Claire, M. W. (2010). Modeling aqueous perchlorate chemistries with applications to Mars. *Icarus*, *207*(2), 675–685. <https://doi.org/10.1016/j.icarus.2009.12.003>
- Martin, P. E., Farley, K. A., Baker, M. B., Malespin, C. A., Schwenzer, S. P., Cohen, B. A., et al. (2017). A two-step K-Ar experiment on Mars: Dating the diagenetic formation of jarosite from amazonian groundwaters. *Journal of Geophysical Research: Planets*, *122*(12), 2803–2818. <https://doi.org/10.1002/2017JE005445>
- McAdam, A. C., Franz, H. B., Sutter, B., Archer, P. D., Freissinet, C., Eigenbrode, J. L., et al. (2014). Sulfur-bearing phases detected by evolved gas analysis of the Rocknest aeolian deposit, Gale Crater, Mars. *Journal of Geophysical Research: Planets*, *119*(2), 373–393. <https://doi.org/10.1002/2013JE004518>
- McGlynn, I. O., Fedo, C. M., & McSween, H. Y. (2011). Origin of basaltic soils at Gusev crater, Mars, by aeolian modification of impact-generated sediment. *Journal of Geophysical Research*, *116*(E7), E00F22. <https://doi.org/10.1029/2010JE003712>
- McLennan, S. M., Anderson, R. B., Bell, J. F., Bridges, J. C., Calef, F., Campbell, J. L., et al. (2013). Elemental geochemistry of sedimentary rocks at Yellowknife Bay, Gale crater, Mars. *Science*, *343*(6169), 1244734. <https://doi.org/10.1126/science.1244734>
- McSween, H. Y., & Keil, K. (2000). Mixing relationships in the Martian regolith and the composition of globally homogeneous dust. *Geochimica et Cosmochimica Acta*, *64*(12), 2155–2166. [https://doi.org/10.1016/S0016-7037\(99\)00401-9](https://doi.org/10.1016/S0016-7037(99)00401-9)
- McSween, H. Y., Taylor, G. J., & Wyatt, M. B. (2009). Elemental composition of the Martian crust. *Science*, *324*(5928), 736–739. <https://doi.org/10.1126/science.1165871>
- Ming, D. W., Archer, P. D., Glavin, D. P., Eigenbrode, J. L., Franz, H. B., Sutter, B., et al. (2014). Volatile and organic compositions of sedimentary rocks in Yellowknife Bay, Gale crater, Mars. *Science*, *343*(6169), 1245267. <https://doi.org/10.1126/science.1245267>
- Ming, D. W., Gellert, R., Morris, R. V., Arvidson, R. E., Brückner, J., Clark, B. C., et al. (2008). Geochemical properties of rocks and soils in Gusev Crater, Mars: Results of the Alpha Particle X-ray Spectrometer from Cumberland ridge to home plate. *Journal of Geophysical Research*, *113*(E12S39), 28. <https://doi.org/10.1029/2008JE003195>
- Ming, D. W., Mittlefehldt, D. W., Morris, R. V., Golden, D. C., Gellert, R., Yen, A., et al. (2006). Geochemical and mineralogical indicators for aqueous processes in the Columbia Hills of Gusev crater, Mars. *Journal of Geophysical Research*, *111*(E2), E02S12. <https://doi.org/10.1029/2005JE002560>
- Mintitti, M. E., Malin, M. C., Van Beek, J. K., Caplinger, M., Maki, J. N., Ravine, M., et al. (2019). Distribution of primary and secondary features in the Pahrump Hills outcrop (Gale crater, Mars) as seen in a Mars Descent Imager (MARDI) “sidewalk” mosaic. *Icarus*, *328*, 194–209. <https://doi.org/10.1016/j.icarus.2019.03.005>
- Morris, R. V., Golden, D. C., Bell, J. F., Shelfer, T. D., Scheinost, A. C., Hinman, N. W., et al. (2000). Mineralogy, composition, and alteration of Mars Pathfinder rocks and soils: Evidence from multispectral, elemental, and magnetic data on terrestrial analogue, SNC meteorite, and Pathfinder samples. *Journal of Geophysical Research*, *105*(E1), 1757–1817. <https://doi.org/10.1029/1999JE001059>
- Morrison, S. M., Downs, R. T., Blake, D. F., Vaniman, D. T., Ming, D. W., Hazen, R. M., et al. (2018). Crystal chemistry of martian minerals from Bradbury landing through Nauyfluff Plateau, Gale crater, Mars. *American Mineralogist*, *103*(6), 857–871. <https://doi.org/10.2138/am-2018-6124>
- Morris, R. V., Vaniman, D. T., Blake, D. F., Gellert, R., Chipera, S. J., Rampe, E. B., et al. (2016). Silicic volcanism on Mars evidenced by tridymite in high-SiO₂ sedimentary rock at Gale crater. *Proceedings of the National Academy of Sciences*, *113*(26), 7071–7076. <https://doi.org/10.1073/pnas.1607098113>
- Nachon, M., Clegg, S. M., Mangold, N., Schröder, S., Kah, L. C., Dromart, G., et al. (2014). Calcium sulfate veins characterized by Chem-Cam/Curiosity at Gale crater, Mars. *Journal of Geophysical Research: Planets*, *119*(9), 1991–2016. <https://doi.org/10.1002/2013JE004588>
- Nachon, M., Mangold, N., Furni, O., Kah, L. C., Cousin, A., Wiens, R. C., et al. (2017). Chemistry of diagenetic features analyzed by Chem-Cam at Pahrump Hills, Gale crater, Mars. *Icarus*, *281*, 121–136. <https://doi.org/10.1016/j.icarus.2016.08.026>
- Nesbitt, H. W., & Wilson, R. E. (1992). Recent chemical weathering of basalts. *American Journal of Science*, *292*(10), 740–777. <https://doi.org/10.2475/ajs.292.10.740>
- Nesbitt, H. W., & Young, G. M. (1982). Early Proterozoic climates and plate motions inferred from major element chemistry of lutites. *Nature*, *299*(5885), 715–717.
- O’Connell-Cooper, C. D., Spray, J. G., Thompson, L. M., Gellert, R., Berger, J. A., Boyd, N. I., et al. (2017). APXS-derived chemistry of the Bagnold dune sands: Comparisons with Gale crater soils and the global martian average. *Journal of Geophysical Research: Planets*, *122*(12), 2623–2643. <https://doi.org/10.1002/2017JE005268>
- O’Connell-Cooper, C. D., Thompson, L. M., Spray, J. G., Berger, J. A., VanBommel, S. J., Gellert, R., et al. (2018). Chemical diversity of sands within the linear and barchan dunes of the bagnold dunes, Gale crater, as revealed by APXS onboard curiosity. *Geophysical Research Letters*, *45*(18), 9460–9470. <https://doi.org/10.1029/2018GL079026>
- Palucis, M. C., Dietrich, W. E., Hayes, A. G., Williams, R. M. E., Gupta, S., Mangold, N., et al. (2014). The origin and evolution of the Peace Vallis fan system that drains to the Curiosity landing area, Gale Crater, Mars. *Journal of Geophysical Research: Planets*, *119*(4), 2013JE004583. <https://doi.org/10.1002/2013JE004583>
- Rampe, E. B., Blake, D. F., Bristow, T. F., Ming, D. W., Vaniman, D. T., Morris, R. V., et al. (2020a). Mineralogy and geochemistry of sedimentary rocks and eolian sediments in Gale crater, Mars: A review after six Earth years of exploration with curiosity. *Geochemistry*, *80*(2), 125605. <https://doi.org/10.1016/j.chemer.2020.125605>
- Rampe, E. B., Bristow, T. F., Morris, R. V., Morrison, S. M., Achilles, C. N., Ming, D. W., et al. (2020b). Mineralogy of Vera Rubin ridge from the Mars Science Laboratory CheMin instrument. *Journal of Geophysical Research: Planets*, *125*(9), e2019JE006306. <https://doi.org/10.1029/2019JE006306>
- Rampe, E. B., Ming, D. W., Blake, D. F., Bristow, T. F., Chipera, S. J., Grotzinger, J. P., et al. (2017). Mineralogy of an ancient lacustrine mudstone succession from the Murray formation, Gale crater, Mars. *Earth and Planetary Science Letters*, *471*, 172–185. <https://doi.org/10.1016/j.epsl.2017.04.021>
- Rapin, W., Meslin, P.-Y., Maurice, S., Vaniman, D., Nachon, M., Mangold, N., et al. (2016). Hydration state of calcium sulfates in Gale crater, Mars: Identification of bassanite veins. *Earth and Planetary Science Letters*, *452*, 197–205. <https://doi.org/10.1016/j.epsl.2016.07.045>
- Rieder, R., Gellert, R., Brückner, J., Klingelhöfer, G., Dreibus, G., Yen, A., & Squyres, S. W. (2003). The new Athena Alpha Particle X-ray Spectrometer for the Mars Exploration Rovers. *Journal of Geophysical Research*, *108*(E12), 8066. <https://doi.org/10.1029/2003JE002150>
- Sara, M. (2017). Dyngjúsandur sand sheet, Iceland, as a depositional analog to the Stimson Fm in Gale crater, Mars. *Theses and Dissertations*. <https://doi.org/10.17077/etd.25rc5gg2>
- Schmidt, M. E., Campbell, J. L., Gellert, R., Perrett, G. M., Treiman, A. H., Blaney, D. L., et al. (2014). Geochemical diversity in first rocks examined by the Curiosity Rover in Gale Crater: Evidence for and significance of an alkali and volatile-rich igneous source. *Journal of Geophysical Research: Planets*, *119*(1), 64–81. <https://doi.org/10.1002/2013JE004481>

- Schmidt, M. E., Perrett, G. M., Bray, S. L., Bradley, N. J., Lee, R. E., Berger, J. A., et al. (2018). Dusty rocks in Gale crater: Assessing areal coverage and separating dust and rock contributions in APXS analyses. *Journal of Geophysical Research: Planets*, *123*(7), 1649–1673. <https://doi.org/10.1029/2018JE005553>
- Schwenzer, S. P., & Kring, D. A. (2009). Impact-generated hydrothermal systems capable of forming phyllosilicates on Noachian Mars. *Geology*, *37*(12), 1091–1094. <https://doi.org/10.1130/G30340A.1>
- Siebach, K. L., Baker, M. B., Grotzinger, J. P., McLennan, S. M., Gellert, R., Thompson, L. M., & Hurowitz, J. A. (2017). Sorting out compositional trends in sedimentary rocks of the Bradbury group (Aeolus Palus), Gale crater, Mars. *Journal of Geophysical Research: Planets*, *122*(2), 295–328. Retrieved from <http://onlinelibrary.wiley.com/doi/10.1002/2016JE005195/full>
- Siever, R. (1957). The silica budget in the sedimentary cycle. *American Mineralogist*, *42*(11–12), 821–841.
- Stack, K. M., Grotzinger, J. P., Lamb, M. P., Gupta, S., Rubin, D. M., Kah, L. C., et al. (2019). Evidence for plunging river plume deposits in the Pahrump Hills member of the Murray formation, Gale crater, Mars. *Sedimentology*, *66*(5), 1768–1802. <https://doi.org/10.1111/sed.12558>
- Stanley, C. R., & Madeisky, H. E. (1996). *Lithochemical exploration for metasomatic zones associated with hydrothermal mineral deposits using Pearce element ratio analysis*, Vancouver, Canada: University of British Columbia.
- Stein, T. C., Arvidson, R. E., Van Bommel, S. J., Wagstaff, K. L., & Zhou, F. (2019). *MSL analyst's Notebook: Curiosity APXS concentration data integration and Mars target encyclopedia and interface updates*. In the 50th Lunar and Planetary Science Conference, Abstract 1820.
- Stein, N., Grotzinger, J. P., Schieber, J., Mangold, N., Hallet, B., Newsom, H., et al. (2018). Desiccation cracks provide evidence of lake drying on Mars, Sutton Island member, Murray formation, Gale Crater. *Geology*, *46*(6), 515–518. <https://doi.org/10.1130/G40005.1>
- Stolper, E. M., Baker, M. B., Newcombe, M. E., Schmidt, M. E., Treiman, A. H., Cousin, A., et al. (2013). The petrochemistry of Jake_M: A martian mugearite. *Science*, *341*(6153), 1239463. <https://doi.org/10.1126/science.1239463>
- Sullivan, R., Arvidson, R., Bell, J. F., Gellert, R., Golombek, M., Greeley, R., et al. (2008). Wind-driven particle mobility on Mars: Insights from Mars exploration rover observations at “el dorado” and surroundings at Gusev Crater. *Journal of Geophysical Research*, *113*(E6), E06S07. <https://doi.org/10.1029/2008JE003101>
- Sun, V. Z., Stack, K. M., Kah, L. C., Thompson, L., Fischer, W., Williams, A. J., et al. (2019). Late-stage diagenetic concretions in the Murray formation, Gale crater, Mars. *Icarus*, *321*, 866–890. <https://doi.org/10.1016/j.icarus.2018.12.030>
- Sutter, B., McAdam, A. C., Mahaffy, P. R., Ming, D. W., Edgett, K. S., Rampe, E. B., et al. (2017). Evolved gas analyses of sedimentary rocks and eolian sediment in Gale Crater, Mars: Results of the Curiosity rover's sample analysis at Mars instrument from Yellowknife Bay to the Namib Dune. *Journal of Geophysical Research: Planets*, *122*(12), 2574–2609. <https://doi.org/10.1002/2016JE005225>
- Sutter, B., McAdam, A. C., Mahaffy, P. R., Ming, D. W., Edgett, K. S., Rampe, E. B., et al. (2018). Evolved gas analyses of sedimentary rocks and eolian sediment in Gale Crater, Mars: Results of the Curiosity rover's sample analysis at Mars instrument from Yellowknife Bay to the Namib Dune. *Journal of Geophysical Research: Planets*, *122*(12), 2574–2609. <https://doi.org/10.1002/2016JE005225>
- Swamy, V., Saxena, S. K., Sundman, B., & Zhang, J. (1994). A thermodynamic assessment of silica phase diagram. *Journal of Geophysical Research*, *99*(B6), 11787–11794. <https://doi.org/10.1029/93JB02968>
- Taylor, G. J., Boynton, W. V., McLennan, S. M., & Martel, L. M. V. (2010). K and Cl concentrations on the martian surface determined by the Mars odyssey gamma ray spectrometer: Implications for bulk halogen abundances in Mars. *Geophysical Research Letters*, *37*(12), L12204. <https://doi.org/10.1029/2010GL043528>
- Taylor, S. R., & McLennan, S. (2010). *Planetary crusts: Their composition, origin and evolution* (1st ed.). Cambridge, UK: Cambridge University Press.
- Thompson, L. M., Berger, J. A., Spray, J. G., Fraeman, A. A., McCraig, M. A., O'Connell-Cooper, C. D., et al. (2020). APXS-derived compositional characteristics of Vera Rubin Ridge and Murray formation, Gale crater, Mars: Geochemical implications for the origin of the ridge. *Journal of Geophysical Research: Planets*, *125*(10), e2019JE006319. <https://doi.org/10.1029/2019JE006319>
- Thompson, L. M., Schmidt, M. E., Spray, J. G., Berger, J. A., Fairén, A. G., Campbell, J. L., et al. (2016). Potassium-rich sandstones within the Gale impact crater, Mars: The APXS perspective. *Journal of Geophysical Research: Planets*, *121*(10), 1981–2003. <https://doi.org/10.1002/2016JE005055>
- Thomson, B. J., Bridges, N. T., Milliken, R., Baldrige, A., Hook, S. J., Crowley, J. K., et al. (2011). Constraints on the origin and evolution of the layered mound in Gale crater, Mars using Mars reconnaissance orbiter data. *Icarus*, *214*(2), 413–432. <https://doi.org/10.1016/j.icarus.2011.05.002>
- Thorpe, M. T., Hurowitz, J. A., & Dehouck, E. (2019). Sediment geochemistry and mineralogy from a glacial terrain river system in Southwest Iceland. *Geochimica et Cosmochimica Acta*, *263*, 140–166. <https://doi.org/10.1016/j.gca.2019.08.003>
- Treiman, A. H., Bish, D. L., Vaniman, D. T., Chipera, S. J., Blake, D. F., Ming, D. W., et al. (2016). Mineralogy, provenance, and diagenesis of a potassic basaltic sandstone on Mars: CheMin X-ray diffraction of the Windjana sample (Kimberley area, Gale crater). *Journal of Geophysical Research: Planets*, *121*(1), 2015JE004932. <https://doi.org/10.1002/2015JE004932>
- Van Es, H. (2017). A new definition of soil. *CSA News*, *62*(10), 20–21. <https://doi.org/10.2134/csa2017.62.1016>
- VanBommel, S. J., Gellert, R., Berger, J. A., Campbell, J. L., Thompson, L. M., Edgett, K. S., et al. (2016). Deconvolution of distinct lithology chemistry through oversampling with the Mars science laboratory Alpha Particle X-ray Spectrometer. *X-Ray Spectrometry*, *45*(3), 155–161. <https://doi.org/10.1002/xrs.2681>
- VanBommel, S. J., Gellert, R., Berger, J. A., Thompson, L. M., Edgett, K. S., McBride, M. J., et al. (2017). 4. *X-Ray Spectrometry*. *46*(4), 229–236. <https://doi.org/10.1002/xrs.2755>
- VanBommel, S. J., Gellert, R., Berger, J. A., Yen, A. S., & Boyd, N. I. (2019b). Mars science laboratory Alpha Particle X-ray Spectrometer trace elements: Situational sensitivity to Co, Ni, Cu, Zn, Ga, Ge, and Br. *Acta Astronautica*, *165*, 32–42. <https://doi.org/10.1016/j.actaastro.2019.08.026>
- VanBommel, S. J., Gellert, R., Boyd, N. I., & Hanaia, J. U. (2019a). Empirical simulations for further characterization of the Mars science laboratory Alpha Particle X-ray Spectrometer: An introduction to the ACES program. *Nuclear Instruments and Methods in Physics Research Section B: Beam Interactions with Materials and Atoms*, *441*, 79–87. <https://doi.org/10.1016/j.nimb.2018.12.040>
- Vaniman, D. T., Bish, D. L., Ming, D. W., Bristow, T. F., Morris, R. V., Blake, D. F., et al. (2014). Mineralogy of a mudstone at Yellowknife Bay, Gale crater, Mars. *Science*, *343*(6169), 1243480. <https://doi.org/10.1126/science.1243480>
- Weitz, C. M., Sullivan, R. J., Lapotre, M. G. A., Rowland, S. K., Grant, J. A., Baker, M., & Yingst, R. A. (2018). Sand grain sizes and shapes in eolian bedforms at Gale crater, Mars. *Geophysical Research Letters*, *45*(18), 9471–9479. <https://doi.org/10.1029/2018GL078972>
- Wiens, R. C., Edgett, K. S., Stack, K. M., Dietrich, W. E., Bryk, A. B., Mangold, N., et al. (2020). Origin and composition of three heterolithic boulder- and cobble-bearing deposits overlying the Murray and Stimson formations, Gale Crater, Mars. *Icarus*, *350*, 113897. <https://doi.org/10.1016/j.icarus.2020.113897>

- Wiens, R. C., Maurice, S., Barraclough, B., Saccoccio, M., Barkley, W. C., Bell, J. F., et al. (2012). The ChemCam instrument suite on the Mars Science Laboratory (MSL) rover: Body unit and combined system tests. *Space Science Reviews*, *170*(1), 167–227. <https://doi.org/10.1007/s11214-012-9902-4>
- Wiens, R. C., Maurice, S., Lasue, J., Forni, O., Anderson, R. B., Clegg, S., et al. (2013). Pre-flight calibration and initial data processing for the ChemCam laser-induced breakdown spectroscopy instrument on the Mars Science Laboratory rover. *Spectrochimica Acta Part B: Atomic Spectroscopy*, *82*, 1–27. <https://doi.org/10.1016/j.sab.2013.02.003>
- Wolfe, E. W., Wise, W. S., & Dalrymple, G. B. (1997). The geology and petrology of Mauna Kea Volcano, Hawaii: A study of postshield volcanism. *US Geological Survey Professional Paper*, (1557), 1–129.
- Yen, A. S., Gellert, R., Schröder, C., Morris, R. V., Bell, J. F., Knudson, A. T., et al. (2005). An integrated view of the chemistry and mineralogy of martian soils. *Nature*, *436*(7047), 49–54. <https://doi.org/10.1038/nature03637>
- Yen, A. S., Ming, D. W., Vaniman, D. T., Gellert, R., Blake, D. F., Morris, R. V., et al. (2017b). Multiple stages of aqueous alteration along fractures in mudstone and sandstone strata in Gale Crater, Mars. *Earth and Planetary Science Letters*, *471*, 186–198. <https://doi.org/10.1016/j.epsl.2017.04.033>
- Yen, A. S., Morris, R. V., Gellert, R., Berger, J. A., Sutter, B., Downs, R. T., et al. (2017a). *Hydrothermal signatures at Gale crater, Mars, and possible in-situ formation of tridymite*. In the 2017 AGU Fall Meeting Abstracts, Abstract P24B-04.
- Yingst, R. A., Edgett, K. S., Kennedy, M. R., Krezoski, G. M., McBride, M. J., Minitti, M. E., et al. (2016). MAHLI on Mars: Lessons learned operating a geoscience camera on a landed payload robotic arm. *Geoscientific Instrumentation, Methods and Data Systems*, *5*(1), 205–217. <https://doi.org/10.5194/gi-5-205-2016>
- Young, G. M., & Nesbitt, H. W. (1998). Processes controlling the distribution of Ti and Al in weathering profiles, siliciclastic sediments and sedimentary rocks. *Journal of Sedimentary Research*, *68*(3), 448–455. <https://doi.org/10.2110/jsr.68.448>

References From the Supporting Information

- Bell, J. F., Godber, A., McNair, S., Caplinger, M. A., Maki, J. N., Lemmon, M. T., et al. (2017). The Mars Science Laboratory Curiosity rover Mastcam instruments: Preflight and in-flight calibration, validation, and data archiving. *Earth and Space Science*, *4*(7), 396–452. <https://doi.org/10.1002/2016EA000219>
- Hamilton, V. E., Morris, R. V., Gruener, J. E., & Mertzman, S. A. (2008). Visible, near-infrared, and middle infrared spectroscopy of altered basaltic tephra: Spectral signatures of phyllosilicates, sulfates, and other aqueous alteration products with application to the mineralogy of the Columbia Hills of Gusev Crater, Mars. *Journal of Geophysical Research*, *113*, 30. <https://doi.org/10.1029/2007JE003049>
- Malin, M. C., & Edgett, K. S. (2000). Sedimentary rocks of early Mars. *Science*, *290*(5498), 1927–1937. <https://doi.org/10.1126/science.290.5498.1927>
- Vasavada, A. R., Grotzinger, J. P., Arvidson, R. E., Calef, F. J., Crisp, J. A., Gupta, S., et al. (2014). Overview of the Mars science laboratory mission: Bradbury landing to Yellowknife Bay and beyond. *Journal of Geophysical Research: Planets*, *119*(6), 2014JE004622. <https://doi.org/10.1002/2014JE004622>